

OneOcc: Semantic Occupancy Prediction for Legged Robots with a Single Panoramic Camera

Hao Shi^{1,2,*} Ze Wang^{1,3,*} Shangwei Guo^{1,*} Mengfei Duan⁴ Song Wang¹ Teng Chen⁵
 Kailun Yang^{4,†} Lin Wang^{2,†} Kaiwei Wang^{1,†}
¹ZJU ²NTU ³MirrorMe Technology ⁴HNU ⁵Xiaomi Corporation

Abstract

Robust 3D semantic occupancy is crucial for legged/humanoid robots, yet most semantic scene completion (SSC) systems target wheeled platforms with forward-facing sensors. We present **OneOcc**, a vision-only panoramic SSC framework designed for gait-introduced body jitter and 360° continuity. **OneOcc** combines: (i) Dual-Projection fusion (DP-ER) to exploit the annular panorama and its equirectangular unfolding, preserving 360° continuity and grid alignment; (ii) Bi-Grid Voxelizeation (BGV) to reason in Cartesian and cylindrical-polar spaces, reducing discretization bias and sharpening free/occupied boundaries; (iii) a lightweight decoder with Hierarchical AMoE-3D for dynamic multi-scale fusion and better long-range/occlusion reasoning; and (iv) plug-and-play Gait Displacement Compensation (GDC) learning feature-level motion correction without extra sensors. We also release two panoramic occupancy benchmarks: **QuadOcc** (real quadruped, first-person 360°) and **Human360Occ** (H3O) (CARLA human-ego 360° with RGB, Depth, semantic occupancy; standardized within-/cross-city splits). **OneOcc** sets a new state of the art on **QuadOcc**, outperforming strong vision baselines and remaining competitive with classical LiDAR baselines; on **H3O** it gains +3.83 mIoU (within-city) and +8.08 (cross-city). Modules are lightweight, enabling deployable full-surround perception for legged/humanoid robots. Datasets and code will be publicly available at [OneOcc](#).

1. Introduction

A holistic 3D understanding of nearby surroundings is fundamental for robotic autonomy in navigation [1–6], locomotion [7–10], manipulation [11–14], and human-robot interaction [15–17]. Among 3D perception tasks, *Semantic Scene Completion* (SSC)—predicting complete volumetric geometry and semantics from partial observations—has be-

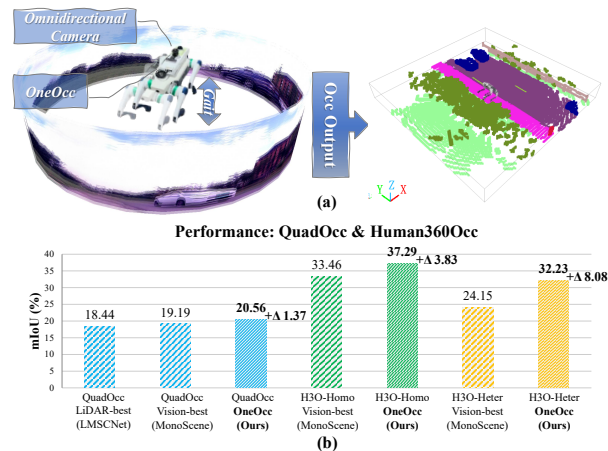


Figure 1. **Teaser.** (a) Single-sensor panoramic semantic scene completion (SSC) on a quadruped: an omnidirectional camera observes full 360° with gait-induced motion; **OneOcc** outputs voxelized semantic occupancy. (b) Summary on **QuadOcc** and **Human360Occ** (H3O): bars show mIoU(%). On **QuadOcc**, **OneOcc** reaches 20.56 mIoU, surpassing the best LiDAR baseline (LMSCNet, 18.44) and vision baseline (MonoScene, 19.19). On **H3O**, **OneOcc** attains 37.29/32.23 mIoU under within-/cross-city, outperforming the best vision baselines (33.46/24.15).

come central [18–21], with most progress driven by autonomous driving where forward-facing sensors on stable wheeled platforms yield benign motion and sensing.

Why legged and humanoid platforms are different. Directly transferring SSC is non-trivial: agile gaits cause *body jitter* that corrupts evidence and breaks temporal coherence; these platforms require full 360° situational awareness in cluttered, uneven terrain; and tight payload/power budgets favor lightweight, single-sensor, low-latency solutions. Hence, we need a panoramic SSC pipeline explicitly robust to gait-induced motion.

Panoramic SSC with a single sensor. A single panoramic camera provides compact, true 360° coverage but introduces annular distortions and seam artifacts after unwrapping [36]—issues poorly handled by perspective-camera SSC pipelines. This motivates a design that preserves raw panoramic cues while exploiting grid-friendly projections.

Method: OneOcc. We propose **OneOcc**, a vision-only

*Equal contribution.

†Corresponding authors (e-mail: kailun.yang@hnu.edu.cn, linwang@ntu.edu.sg, wangkaiwei@zju.edu.cn).

Datasets	Data			Domain				Modality	Volume Size	Scenes	Frames	Anno.
	Camera	Sur.	Plat.	Move.	Env.	Weath.	Lighting					
NYUv2 [22]	Pinhole	✗			Indoor	✗	✗	C&D	(144×240×240)	1.4K	1.4K	
ScanNet [23]	Pinhole	✗			Indoor	✗	✗	C&D	(31×62×62)	1.5K	1.5K	
SUNCG [24]	Pinhole	✗			Indoor	✗	✗	C&D	(144×240×240)	46K	140K	
SemanticPOSS [25]	<i>n.a.</i>	✗			Outdoor	✗		L	(32×256×256)	6	3K	
SemanticKITTI [26]	Pinhole	✗			Outdoor	✗		C&L	(32×256×256)	22	9K	
nuScenes [27]	Pinhole+Fish-eye	✓			Outdoor	✓		C&L	(40×512×512)	850	200K	
Occ3D-Waymo [28]	Pinhole+Fish-eye	✓			Outdoor	✓		C&L	(32×200×200)	1K	200K	
SSCBench-KITTI-360 [29]	Fisheye	✓			Outdoor	✗		C&L	(32×200×200)	11	91K	
ScribbleSC [30]	Pinhole	✗			Outdoor	✗		C&L	(32×256×256)	11	9K	
OmniHD-Scenes [31]	Pinhole	✓			Outdoor	✗		C&L&R	–	200	60K	
WildOcc [32]	Pinhole	✗			Outdoor	✗		C&L	(40×100×100)	5	10K	
DSEC-SSC [33]	Pinhole	✗			Outdoor	✗		C&L&E	(16×128×128)	6	3K	
ORAD-3D [34]	Pinhole	✓			Outdoor	✓		C&L	–	145	58K	
Co3SOP [35]	Pinhole	✗			Outdoor	✗		C&L	(70×1000×1000)	–	–	
Human360Occ (ours)	Panoramic	✓			Outdoor	✓		C&D	(16×128×128)	160	8K	
QuadOcc (ours)	Panoramic	✓			Outdoor	✗		C&L	(8×64×64)	10	24K	

Table 1. Typical datasets for Semantic Scene Completion (SSC). Abbreviations: (Autonomous Car), (Quadruped Robot), (Vision Foundation Model), (Human), (Synthetic), (Internet images/videos), (Wheels), (Gait), (Stationary), (Day), (Dusk), (Night), Sur. (Surround), Plat. (Platform), Move. (Movement), Env. (Environment), Weath. (Weather diversity), Anno. (Annotation), C (Camera), D (Depth), L (LiDAR), R (Radar).

panoramic SSC framework for severe body jitter and 360° continuity, integrating: (i) *Dual-Projection fusion (DP-ER)* to jointly process the raw annular panorama and its equirectangular unfolding; (ii) *Bi-Grid Voxelization (BGV)* that reasons in Cartesian and polar/cylindrical voxel spaces to reduce discretization bias and better match panoramic geometry; (iii) a lightweight decoder with *Hierarchical AMoE-3D* for dynamic multi-scale 3D fusion; and (iv) a plug-and-play *Gait Displacement Compensation (GDC)* that learns feature-level jitter correction without extra sensors.

Benchmarks: QuadOcc and Human360Occ (H3O). To advance panoramic SSC on legged/humanoid robots, we release two complementary benchmarks. *QuadOcc* is a real first-person 360° dataset on a quadruped within a campus domain, with standardized day/dusk/night coverage and semi-automatic ground truth (multi-frame LiDAR aggregation, Grounded-SAM [37] initialization, targeted manual fixes). It contains 10 scenes and 24K frames, uses 6 semantic categories for training. The occupancy uses 0.4 m voxels on a 64 × 64 × 8 grid—reflecting embodied compute and lower speed than cars. *Human360Occ (H3O)* is CARLA-based human-ego 360° with simulated gait, 160 sequences / 8K frames over 16 maps and multiple weathers/times; each frame provides RGB, metric depth, semantic occupancy at 64×64×8 and 128×128×16, and pose. It supports *within-city* (per-map 8:2 train/val) and *cross-city* (default 12/4 maps) splits. See details on the construction pipeline and dataset statistics in the supplementary material.

Results in brief. On *QuadOcc*, OneOcc reaches 20.56 mIoU, surpassing the best LiDAR baseline (LMSCNet, 18.44; +2.12 mIoU, +11.5%) and the best vision baseline (MonoScene, 19.19; +1.37 mIoU). On *H3O*, it at-

tains 37.29/32.23 mIoU under within-/cross-city, improving over the best vision baselines (33.46/24.15) by +3.83 and +8.08 mIoU (up to +33.5% relative); see Fig. 1(b).

Contributions.

- **Method.** *OneOcc* integrates *DP-ER*, *BGV*, *Hierarchical AMoE-3D*, and *GDC* to deliver jitter-robust, full-surround SSC with lightweight computation.
- **Datasets.** Two panoramic occupancy benchmarks for legged robots: *QuadOcc* (real quadruped, 360°, 10 scenes/24K frames, 6 categories, 0.4m voxels on 64 × 64 × 8) and *H3O* (CARLA human-ego 360°, 160 seq/8K frames on 16 maps, per-frame RGB/Depth/voxels/pose, two voxel resolutions).
- **Evaluation.** Extensive benchmarking shows vision-only *OneOcc* rivals or surpasses classic LiDAR-based methods under realistic legged/humanoid settings.

2. Related Work

Semantic scene completion. Semantic Scene Completion (SSC) predicts a complete 3D voxel scene with semantics from partial observations. *LiDAR-based SSC.* From SSC-Net [24] to LMSCNet [38], LiDAR pipelines evolved from dense 3D CNNs to efficient BEV-like decoders; later works (e.g., JS3C-Net [39], SCPNet [40]) enhance long-range context and 3D aggregation. Non-Cartesian discretizations mitigate quantization bias (PointOcc [41], inspired by Cylinder3D [42]); recent efforts also improve supervision efficiency and robustness [43, 44]. Yet LiDAR stacks are often heavy and power-hungry for constrained platforms [45–49]. *Vision-based SSC.* The ill-posed 2D→3D lifting has progressed rapidly: MonoScene [50] set a strong baseline; transformer models (VoxFormer [51], OccFormer [52])

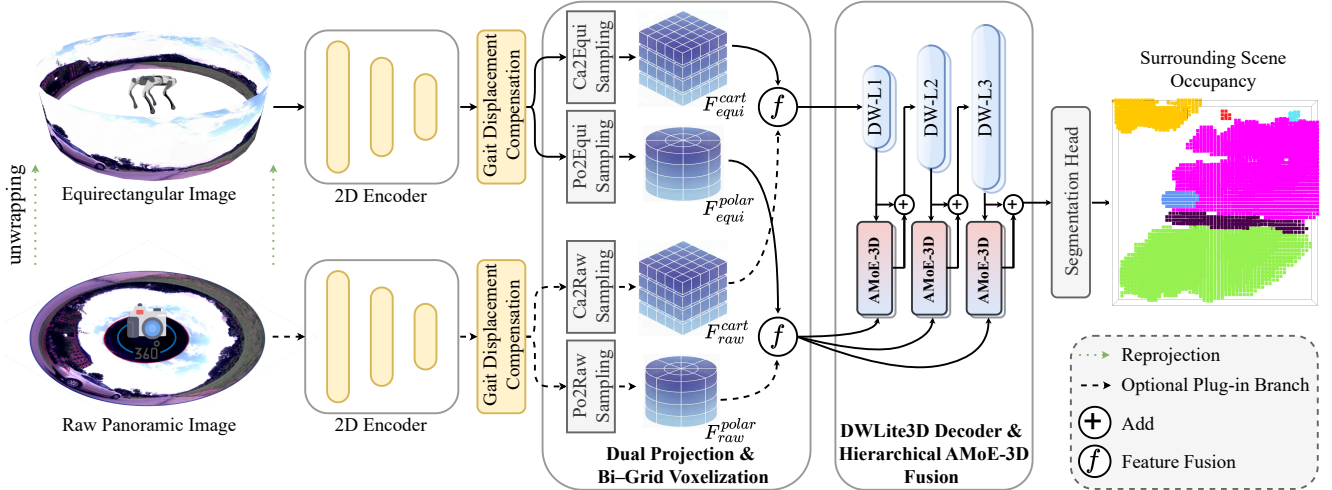


Figure 2. **OneOcc pipeline.** Calibrated *unwrapping* maps the raw panorama to equirectangular. Two 2D encoders (*DP-ER*) feed *GDC* for feature-level gait compensation (optional on H3O). At three scales, *BGV* builds Cartesian and polar/cylindrical voxel grids; voxel-centroid features are sampled to each view (Ca/Po \rightarrow Equi/Raw) and fused. A lightweight 3D decoder with *Hierarchical AMoE-3D* aggregates multi-scale context, followed by a head predicting full-surround occupancy. *Abbrev.*: Ca/Po = Cartesian/Polar; Equi = equirectangular.

improve global aggregation. Follow-ups refine supervision/projection (RenderOcc [53], InverseMatrixVT3D [54], SfMOcc [55]) and pursue efficiency via sparsity or streamlined designs [56–58]. Other lines study context disentangling/causality [59, 60] and scene-adaptive decoders or occlusion-aware projections [61, 62]; for deployment, OccFiner [63] and TALOS [64] target offboard refinement and test-time adaptation. *Gaussian/weak-supervision SSC.* GaussianOcc-style methods [65, 66] reduce dense 3D labeling via Gaussian/flow priors, and GaussianFormer variants [67, 68] model scenes as Gaussian fields for efficient camera-based occupancy. *Panoramic SSC and multi-modality.* While most camera-based SSC methods assume forward pinhole views, emerging works leverage omnidirectional sensing: panoramic depth for occupancy [69], real-time fisheye occupancy without semantics [70], cylindrical fusion [71], event cameras for HDR/blur [33], and radar-camera fusion for joint tasks [72]. Multimodal pipelines [45, 73–75] highlight complementary cues but increase system complexity. In contrast, we target a *single panoramic camera with full-360° continuity under gait-induced jitter*, a setting under-explored by prior literature.

Semantic scene understanding for legged robots. Legged autonomy motivates perception tailored to agile motion and strict payload budgets. Prior efforts include vision-based terrain reconstruction [76], large-scale datasets [77], and traversability learning [78–80]; complementary modules cover robust tracking [81, 82] and instruction grounding [83, 84]. With increasing evidence that limited FoV hinders agility [85–87], panoramic sensors are adopted for omnidirectional tracking [88], multimodal odometry [89], and even satellite communication on the move [90]. Some works study probabilistic semantic mapping [91], and

humanoid systems explore panoramic/occupancy perception [21, 92–94]. However, *dense 3D semantic occupancy* from a *single panoramic camera* on dynamic legged platforms is still largely open. We address this by releasing *QuadOcc* and *Human360Occ* and proposing *OneOcc*, a lightweight panoramic occupancy framework built around dual-projection fusion, bi-grid voxelization, hierarchical 3D MoE fusion, and gait displacement compensation.

3. Method

3.1. Problem Formulation

Given a panoramic RGB image $\mathbf{I} \in \mathbb{R}^{H \times W \times 3}$ and calibrated intrinsics/extrinsics, we aim to predict a dense 3D semantic occupancy $\mathbf{S} \in \{0, \dots, C\}^{X \times Y \times Z}$. We produce per-voxel logits $\mathbf{Z} \in \mathbb{R}^{X \times Y \times Z \times C}$, and the final label is $\hat{s}_{x,y,z} = \arg \max_c \mathbf{Z}_{x,y,z,c}$.

3.2. Overview

Motivation. (1) A 360° panorama exhibits *ring continuity* and strong projection distortion: a single projection cannot balance resolution and receptive fields near the poles vs. the equator; (2) Legged locomotion induces *gait jitters* (impulsive foot strikes, small roll/pitch) that hurt the feature \rightarrow voxel lifting step more than the image \rightarrow feature step; (3) Surrounding SSC must reconcile *near-field contact geometry* and *far-field ring context*. **Principles.** We therefore combine *dual-projection encoders (DP-ER)*, *bi-grid voxelization (BGV)*, a lightweight *Gait Displacement Compensation (GDC)* before lifting, and a *Hierarchical AMoE-3D* decoder for scale-aware, anisotropic fusion.

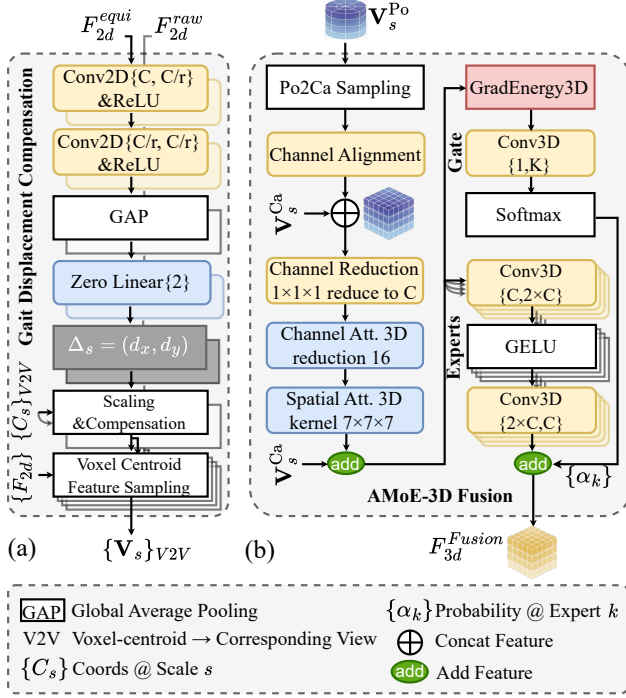


Figure 3. **GDC and AMoE-3D Fusion Module.** (a) GDC regresses $\Delta = (dx, dy)$ from 2D features via GAP+Linear (zero-init), applies scale/shift to multi-scale view coordinates $\{C_s\}$ for voxel-centroid sampling, and yields $\{F_{3d}\}_{V2V}$. (b) AMoE-3D fuses Po2Ca-sampled polar features with Cartesian ones via channel alignment, concatenation, and reduction, applies 3D channel- and spatial attention, and performs MoE-Fuse3D with K experts and GradEnergy3D-Softmax gating: $y = \sum_k P_k \odot E_k(x)$. The fused F_{3d}^{Fusion} feeds the 3D decoder.

3.3. Unwrapping and Dual-Projection Encoders

Motivation. Equirectangular views preserve *azimuthal continuity* that is convolution-friendly; the raw panoramic annulus retains *native geometry and fine textures*. Running both in parallel compensates the equator-pole trade-off.

Method. We calibrate the omnidirectional panoramic annular lens (PAL) camera with the Taylor polynomial model [95]. The unwrapping samples the raw annulus at coordinates given by the calibrated inverse mapping:

$$\mathbf{I}^{equi}(u, v) = \mathbf{I}^{raw}(U^{-1}(u, v; \boldsymbol{\kappa})), \quad (1)$$

where $\boldsymbol{\kappa} = \{a_i, u_0, v_0, \mathbf{A}\}$ are the Taylor coefficients and principal point plus a 2×2 affine matrix (scale/skew), and $(u, v) \in [0, W] \times [0, H]$. For the equirectangular ray with spherical angles (ϕ, θ) :

$$\begin{aligned} \phi &= \frac{2\pi}{W} u - \pi, & \theta &= \frac{\pi}{2} - \frac{\pi}{H} v, \\ r(\theta) &= \sum_{i=0}^N a_i \theta^i, & \begin{bmatrix} u_{raw} \\ v_{raw} \end{bmatrix} &= \begin{bmatrix} u_0 \\ v_0 \end{bmatrix} + \mathbf{A} r(\theta) \begin{bmatrix} \cos \phi \\ \sin \phi \end{bmatrix}. \end{aligned} \quad (2)$$

Two encoders then produce multi-scale features:

$$\{\mathbf{F}_{1/s}^{equi}\}_{s \in \{1,4,8,16\}}, \quad \{\mathbf{F}_{1/s}^{raw}\}_{s \in \{1,4,8,16\}}, \quad (4)$$

with GroupNorm and 1×1 bottleneck alignment to standardize channels.

Why it helps. For legged robots, the equatorial ring dominates motion priors while polar areas are highly distorted. Using the Taylor unwrapping respects PAL optics, preserving *ring continuity* in ER space and *local textures* in the raw annulus, providing more stable cues for lifting.

3.4. Bi-Grid Voxelization and View2View Sampling

Motivation. Cartesian voxels are accurate for *near-field contact geometry* (footholds, obstacles), whereas polar/cylindrical voxels preserve *azimuthal continuity* that matches panoramic imaging. In a 360° camera, the equirectangular horizontal axis is linearly related to azimuth ϕ ; cylindrical voxels (r, φ, z) therefore form a *natural, camera-aligned* parameterization where $\varphi \approx \phi$ and r correlates with depth, yielding uniform sampling along the ring and reduced far-field aliasing. Combining Cartesian and cylindrical grids reduces quantization bias and balances near/far evidence under legged motion.

Method. We define voxel centroids

$$\begin{cases} \mathbf{c}_{ijk}^{Ca} = (x_i, y_j, z_k), \\ \mathbf{c}_{pqk}^{Po} = (r_p \cos \varphi_q, r_p \sin \varphi_q, z_k). \end{cases} \quad (5)$$

For view $v \in \{\text{equi}, \text{raw}\}$ and scale s , we lift features by bilinear sampling at the projected pixel $\pi_v(\cdot)$:

$$\begin{cases} \mathbf{V}_s^{Ca}(\mathbf{c}) = \text{bilinear}(\mathbf{F}_{1/s}^v, \pi_v(\mathbf{c}; \boldsymbol{\kappa})), \\ \mathbf{V}_s^{Po}(\mathbf{c}) = \text{bilinear}(\mathbf{F}_{1/s}^v, \pi_v(\mathbf{c}; \boldsymbol{\kappa})). \end{cases} \quad (6)$$

We fuse scales with per-voxel convex weights:

$$\begin{cases} \mathbf{V}^{Ca} = \sum_s \alpha_s^{Ca} \odot \mathbf{V}_s^{Ca}, & \sum_s \alpha_s^{Ca} = 1, \\ \mathbf{V}^{Po} = \sum_s \alpha_s^{Po} \odot \mathbf{V}_s^{Po}, & \sum_s \alpha_s^{Po} = 1. \end{cases} \quad (7)$$

To inject polar context into the Cartesian stream, we precompute cross-grid indices $\{\mathcal{J}_\ell\}_{\ell \in \{1,2,4\}}$ and form

$$\tilde{\mathbf{V}}_\ell^{Ca} = \text{Align}_{1 \times 1 \times 1}(\mathbf{V}_\ell^{Po}[\mathcal{J}_\ell]) \parallel \mathbf{V}_\ell^{Ca}. \quad (8)$$

Why it helps. On legged robots, near-field foothold safety leverages Cartesian precision while far-field loop-context exploits cylindrical efficiency. The camera-aligned polar stream improves *azimuthal coherence* and reduces spherical-distortion artifacts; the fused bi-grid volume balances near/far evidence under gait jitters.

Table 2. **Semantic scene completion results on the QuadOcc validation set.** All models are (re)trained by us on QuadOcc. **Bold** = best, underline = second best (within the LiDAR-based block; Vision-based block marked separately.)

Method	Input	vehicle (0.90%)	pedestrian (2.09%)	road (52.34%)	building (14.00%)	vegetation (22.82%)	terrain (7.85%)	Precision \uparrow	Recall \uparrow	IoU \uparrow	mIoU \uparrow
											
<i>LiDAR-based</i>											
SSCNet [24]	L	0.00	0.04	44.34	<u>16.06</u>	22.41	4.77	63.42	65.82	47.71	14.60
SSCNet-full [24]	L	0.71	0.04	<u>55.14</u>	14.93	19.66	7.76	<u>78.81</u>	60.03	<u>51.69</u>	16.38
LMSCNet [38]	L	<u>0.88</u>	<u>0.20</u>	57.02	16.45	<u>24.39</u>	11.70	79.70	<u>64.49</u>	55.40	18.44
OccRWKV [46]	L	2.05	0.35	54.17	10.29	24.92	<u>8.38</u>	71.98	62.80	50.47	<u>16.69</u>
<i>Vision-based</i>											
VoxFormer-S [51]	P+D	0.31	1.67	36.83	6.48	7.09	3.81	45.96	69.95	38.38	9.36
SGN [96]	P+D	7.39	1.88	53.35	9.06	21.95	9.39	59.23	67.41	46.05	17.17
VoxFormer-S [†] [51]	P+L	0.24	1.66	38.51	10.90	11.88	4.45	51.29	75.84	44.08	11.27
VoxFormer-T [†] [51]	P+L	0.30	1.65	40.21	14.48	15.86	4.64	56.94	77.10	48.70	12.86
SGN [†] [96]	P+L	<u>11.62</u>	<u>2.47</u>	53.06	<u>15.60</u>	<u>25.67</u>	9.91	73.70	59.62	49.16	<u>19.72</u>
OccFormer [52]	P	0.29	0.37	49.46	10.36	15.00	2.64	45.79	<u>76.99</u>	40.28	13.02
MonoScene [50]	P	8.15	1.59	55.66	12.88	26.10	10.78	62.10	69.28	48.69	19.19
OneOcc (Ours)	P	12.16	2.86	<u>54.41</u>	16.03	24.91	13.01	<u>66.69</u>	64.74	<u>48.92</u>	20.56

[†] Uses a different sensor modality from the original paper (here: *adding LiDAR*).

Input legend: L = LiDAR; P = *Panoramic* camera; D = monocular Depth (pred.).

3.5. Gait Displacement Compensation

Motivation. Gait shocks induce phase errors; correcting them *after* lifting acts on already voxel-quantized evidence. Compensating *before* lifting—at sampling coordinates—avoids quantization and is cheaper.

Method. For each scale and projection, we regress a 2D displacement $\Delta_s = (d_x, d_y)$ with a zero-initialized head:

$$\Delta_s = \text{Linear}_0\left(\text{GAP}(\mathbf{F}_{1/s}^v)\right), \quad (9)$$

where Linear_0 has all weights and bias set to zero so the initial warp is identity (cf. zero-conv [97]). Before lifting we correct and resample:

$$\hat{\mathbf{p}} = \pi_v(\mathbf{c}; \boldsymbol{\kappa}) + \Delta_s, \quad (10)$$

$$\mathbf{V}_s^{(\cdot)}(\mathbf{c}) = \text{bilinear}\left(\mathbf{F}_{1/s}^v, \hat{\mathbf{p}}\right). \quad (11)$$

In practice, this also upgrades the lifting operator from integer-index gather [50] to bilinear sampling, which reduces projection aliasing and further stabilizes GDC. Here, $v \in \{\text{unwrapped, spherical}\}$ indexes the projection path; $\pi_v(\mathbf{c}; \boldsymbol{\kappa})$ projects a 3D voxel centroid \mathbf{c} to image pixels using the calibrated Taylor camera with parameters $\boldsymbol{\kappa}$. $\hat{\mathbf{p}}$ is the corrected sampling pixel; $\text{bilinear}(\cdot)$ samples the 2D feature map $\mathbf{F}_{1/s}^v$, and $\mathbf{V}_s^{(\cdot)}$ denotes the lifted 3D feature.

Why it helps. GDC routes the *phase error* back to 2D, preventing mis-attributed voxels. The zero-init head stabilizes early training and leaves features unperturbed when motion is tiny ($\Delta_s \approx 0$). We additionally provide qualitative analysis of GDC in the supplementary material.

3.6. Hierarchical AMoE-3D

Motivation. Panoramic scenes are *anisotropic*: strong azimuthal variation vs. vertical structure, and large near/far scale disparity. We thus (i) inject polar cues hierarchically (coarse-to-fine), and (ii) apply *voxel-wise expert selection* to prevent over-smoothing in flat regions while enhancing edges/contacts critical for locomotion.

Method. The 3D decoder is a depthwise-separable UNet with trilinear upsampling at three levels (L1/L2/L3). At each level we fuse $\tilde{\mathbf{V}}^{\text{Ca}}$ using a *dual-path volumetric saliency* and a *Mixture-of-Experts* (MoE) fuse; we term this module *AMoE-3D*, where *A* denotes attention implemented via the dual-path (channel & spatial) saliency gates.

Dual-path volumetric saliency (channel & spatial gates):

$$\begin{cases} \mathbf{A}_c = \sigma\left(\text{MLP}(\text{GAP}(\mathbf{X})) + \text{MLP}(\text{GMP}(\mathbf{X}))\right), \\ \mathbf{A}_s = \sigma\left(g^{7 \times 7 \times 7}([\text{Avg}(\mathbf{X}); \text{Max}(\mathbf{X})])\right), \\ \mathbf{Y} = \mathbf{X} \odot \mathbf{A}_c \odot \mathbf{A}_s. \end{cases} \quad (12)$$

Table 3. **Semantic scene completion using Panoramas on H3O (Human360Occ)**. Two vertically-stacked panels report results on **HOMO (within-city)** and **HETER (cross-city)** splits. Header frequencies are computed on *non-empty* voxels. **Input legend:** P = Panoramic camera; D_{pred} = predicted monocular depth; D_{gt} = ground-truth depth.

HOMO (within-city)															
Method	Input	road	sidewalk	building	vegetation	car	truck	bus	two-wheeler	person	pole	Precision	Recall	IoU	mIoU
		(34.04%)	(26.24%)	(10.00%)	(24.02%)	(2.92%)	(0.99%)	(0.25%)	(0.07%)	(0.97%)	(0.50%)				
VoxFormer-S [51]	$P+D_{pred}$	22.27	17.44	2.86	5.65	0.87	0.14	0.00	0.00	61.46	0.18	40.21	59.49	31.57	11.09
VoxFormer-S [51]	$P+D_{gt}$	35.84	25.86	12.32	9.90	3.73	0.70	0.19	0.17	64.79	0.93	59.91	71.12	48.19	15.44
SGN-T [96]	$P+D_{pred}$	54.55	44.61	15.51	35.16	23.91	7.68	4.52	15.77	65.24	19.46	61.82	64.36	46.05	28.64
SGN-S [96]	$P+D_{pred}$	54.81	47.44	15.64	33.22	24.23	8.53	2.62	13.51	65.88	19.72	62.28	63.72	45.98	28.56
OccFormer [52]	P	54.11	46.41	15.14	32.84	17.57	4.30	0.00	1.65	65.08	11.72	57.30	69.94	45.98	24.88
MonoScene [50]	P	62.45	57.18	19.97	38.91	29.76	13.77	5.03	16.76	70.15	20.67	68.78	71.66	54.08	33.46
OneOcc (Ours)	P	63.82	62.92	22.86	41.03	33.74	17.79	6.47	26.58	71.13	26.55	69.14	74.18	55.73	37.29

HETER (cross-city)															
Method	Input	road	sidewalk	building	vegetation	car	truck	bus	two-wheeler	person	pole	Precision	Recall	IoU	mIoU
		(34.04%)	(26.24%)	(10.00%)	(24.02%)	(2.92%)	(0.99%)	(0.25%)	(0.07%)	(0.97%)	(0.50%)				
VoxFormer-S [51]	$P+D_{pred}$	19.02	15.82	2.84	5.86	0.95	0.10	0.00	0.01	61.62	0.10	36.68	52.00	27.40	10.63
VoxFormer-S [51]	$P+D_{gt}$	32.55	25.95	8.98	9.93	4.68	0.44	0.00	0.00	65.45	0.26	59.08	61.21	42.99	14.82
SGN-T [96]	$P+D_{pred}$	42.57	23.94	9.42	15.84	18.22	10.21	1.55	3.11	63.44	11.93	45.84	47.11	30.26	20.02
SGN-S [96]	$P+D_{pred}$	43.47	24.70	9.19	20.27	17.21	8.21	1.85	5.08	61.10	14.89	47.82	50.98	32.76	20.60
OccFormer [52]	P	47.00	39.01	10.14	24.85	11.84	1.52	0.05	0.77	66.60	6.93	53.12	63.57	40.73	20.87
MonoScene [50]	P	49.68	41.41	11.04	20.57	20.34	10.36	1.98	2.79	69.68	13.69	67.39	55.00	43.44	24.15
OneOcc (Ours)	P	58.60	48.28	16.34	25.98	30.68	19.35	12.87	14.16	72.89	23.11	67.89	64.77	49.58	32.23

MoE-Fuse3D with gradient-energy gating:

$$\begin{cases} \text{GradEnergy3D}(\mathbf{Y}) = \sum_{a \in \{x, y, z\}} \|\nabla_a \mathbf{Y}\|_2^2, \\ \alpha = \text{softmax}(W_g * \text{GradEnergy3D}(\mathbf{Y})), \\ \tilde{\mathbf{Y}} = \mathbf{Y} + \sum_{k=1}^K \alpha_k E_k(\mathbf{Y}), \end{cases} \quad (13)$$

where E_k are $1 \times 1 \times 1$ Conv-GELU-Conv experts. Here, $\mathbf{X} \in \mathbb{R}^{C \times D \times H \times W}$ is the level- ℓ Cartesian feature and $\tilde{\mathbf{V}}^{\text{Ca}}$ is the polar volume resampled onto the same Cartesian grid; $\mathbf{A}_c \in \mathbb{R}^{C \times 1 \times 1 \times 1}$ and $\mathbf{A}_s \in \mathbb{R}^{1 \times D \times H \times W}$ are the channel and spatial gates. ∇_a denotes the discrete 3D gradient along axis $a \in \{x, y, z\}$, $*$ is 3D convolution, and $[\ ;]$ concatenates along channels.

Why it helps. Hierarchical polar injections aggregate *far-field azimuthal cues* at coarse levels—e.g., ring-consistent *road/building/vegetation* context—and refine *near-field contact geometry* at fine levels. Gradient-energy gating em-

phasizes high-contrast structures at category transitions (vehicles, poles) while suppressing overfitting on large ground flats (road), improving stability of foothold decisions.

3.7. Segmentation Head and Loss

Method. A $1 \times 1 \times 1$ head outputs per-voxel logits \mathbf{Z} . We supervise only *valid* voxels (from lifting visibility) with deep supervision at strides $\{1, 2, 4\}$.

Loss. We follow MonoScene [50] for most losses: (i) standard cross-entropy on valid voxels, (ii) the scene-class affinity (SCAL) terms for semantics and geometry, and (iii) the frustums proportion (FP) loss. We do *not* use the relation loss, as we observed it encourages co-occurrence priors that over-smooth azimuthal boundaries and suppress small near-field classes under panoramic legged setting, yielding no gain and occasional degradation on our data. The final objective is:

$$\mathcal{L}_{\text{total}} = \mathcal{L}_{\text{CE}} + \mathcal{L}_{\text{SCAL}}^{\text{sem}} + \mathcal{L}_{\text{SCAL}}^{\text{geo}} + \mathcal{L}_{\text{FP}}. \quad (14)$$

Class re-weighting for \mathcal{L}_{CE} follows standard SSC practice.

Table 4. Ablations on QuadOcc (Panorama only). Core columns show if a component is enabled (✓) or disabled (✗).

Variant	Core Designs				Per-class IoU (QuadOcc)						Overall			
	GDC Grid Disp. Compensation	DP-ER Dual Projection (Equiv. + Row)	BGV Bi-Grid Voxelization	AMoE-3D Attention-MoE 3D Fusion	vehicle (0.90%)	pedestrian (2.09%)	road (52.34%)	building (14.00%)	vegetation (22.82%)	terrain (7.85%)	SC Precision	SC Recall	SC IoU	SSC mIoU
(Q0) baseline	✗	✗	✗	✗	8.15	1.59	55.66	12.88	26.10	10.78	62.10	69.28	48.69	19.19
(Q1) + GDC	✓	✗	✗	✗	11.76	2.48	53.73	15.07	22.95	11.51	64.05	66.08	48.78	19.58
(Q2) + DP-ER	✓	✓	✗	✗	11.82	2.51	54.16	15.39	23.40	12.08	65.42	65.01	48.38	19.89
(Q3) + BGV	✓	✓	✓	✗	<u>12.07</u>	<u>2.77</u>	54.29	<u>15.76</u>	24.19	<u>12.74</u>	<u>66.56</u>	64.70	48.68	<u>20.30</u>
(Q4) + AMoE-3D	✓	✓	✓	✓	12.16	2.86	<u>54.41</u>	16.03	<u>24.91</u>	13.01	66.69	64.74	48.92	20.56

Table 5. Performance comparison on the QuadOcc validation set across different lighting conditions. Results are shown for day, dusk, and night scenarios. P (Precision), R (Recall), IoU and mIoU are reported. Methods marked with † use a sensor modality different from the original paper. The best performance for each input modality is highlighted in bold.

Method	Day ☀				Dusk 🌄				Night 🌃			
	P	R	IoU	mIoU	P	R	IoU	mIoU	P	R	IoU	mIoU
<i>LiDAR-based</i>												
SSCNet [24]	67.12	62.95	48.12	14.03	52.97	76.34	45.50	14.88	57.81	75.30	48.60	9.51
SSCNet-full [24]	80.56	58.52	51.28	16.04	73.79	64.34	52.37	17.14	73.64	67.31	54.24	11.56
LMSCNet [38]	81.18	62.50	54.59	17.33	75.34	70.92	57.56	18.91	75.68	72.67	58.91	13.40
OccRWKV [46]	72.84	63.83	51.56	16.25	66.43	59.30	45.63	15.42	74.10	58.31	48.44	12.61
<i>Vision-based</i>												
OccFormer [52]	46.23	77.08	40.64	12.82	41.79	79.45	37.72	14.46	49.49	72.18	41.56	10.21
VoxFormer-S† [51]	55.80	73.96	46.64	11.44	37.42	82.81	34.73	8.95	47.10	82.41	42.80	11.84
VoxFormer-T† [51]	61.77	75.02	51.24	12.91	42.25	84.68	39.25	11.06	51.93	84.62	47.45	12.88
SGN [96]	61.54	68.71	48.06	17.94	54.07	69.06	43.53	15.19	46.83	52.29	32.81	10.58
MonoScene [50]	65.47	69.94	51.09	18.58	47.62	77.10	41.72	15.14	51.35	66.47	40.78	14.20
OneOcc (Ours)	69.10	64.66	50.15	21.15	57.46	71.98	46.96	19.86	63.56	53.75	41.09	13.50

4. Experiments

4.1. Setup

Datasets. We evaluate on two panoramic occupancy benchmarks for legged/humanoid platforms. **QuadOcc:** real first-person 360° data on a quadruped within a campus; day/dusk/night, sequence-heterogeneous split; 24K consecutive frames with *stride-5* training; 6 classes on a 64×64×8 grid (0.4 m). **Human360Occ (H3O):** CARLA-based human-ego 360° with simulated gait over 16 maps and diverse weather/lighting; RGB, depth, occupancy (two resolutions), and poses. We report *within-city* (H3O-Homo) and *cross-city* (H3O-Heter). See supplementary for the data collection pipelines and statistics of QuadOcc and H3O.

Metrics. Following semantic scene completion (SSC) practice, we report per-class IoU and mean IoU (mIoU) on non-empty voxels, plus overall precision (P) and recall (R).

Baselines. We re-train popular LiDAR SSC systems (SSCNet [24], LMSCNet [38], OccRWKV [46]) and adapt representative vision SSC methods (OccFormer [52], VoxFormer [51], SGN [96], MonoScene [50]) to panoramas via calibrated unwrapping to equirectangular. For *P+L* entries in Table 2, we add LiDAR to the corresponding vision model per the table footnote. Details in the supplementary.

Implementation. Unless noted, training follows official configs with minimal dataset-specific changes; schedules/image sizes/voxelization match for fairness. On H3O we disable the raw-projection branch (native equirectangu-

lar), keeping components as in ablations. Training uses a single RTX-4090 GPU. Details in the supplementary.

4.2. Quantitatively Comparisons

QuadOcc. Table 2 reports *QuadOcc (val)*. OneOcc attains 20.56 mIoU, surpassing the best LiDAR baseline LMSCNet (18.44) and the strongest vision baseline MonoScene (19.19). SGN† (P+L) achieves the highest geometry IoU (49.16) among vision entries by leveraging LiDAR, yet camera-only OneOcc delivers the best *mIoU* (20.56) among vision methods. Task-aligned panoramic fusion (DP-ER, BGV, AMoE-3D, with GDC on legged data) enables a camera-only pipeline to rival and even surpass popular LiDAR stacks at this range/resolution.

Human360Occ (H3O). Table 3 summarizes generalization: On H3O-Homo OneOcc reaches 37.29 mIoU (+3.83 vs. MonoScene), while on H3O-Heter it attains 32.23 mIoU (+8.08). The larger margin under *heterogeneous* cross-city shifts highlights OneOcc’s strong distribution robustness: DP-ER and AMoE-3D transfer across maps and lighting/weather, and their distortion-aware priors mitigate panoramic aliasing, yielding state-of-the-art camera-only mIoU under distribution shift.

Robustness to Lighting Conditions. Table 5 reports day/dusk/night. OneOcc leads the best vision baseline in day (21.15 vs. 18.58) and dusk (19.86 vs. 15.14); at night its mIoU (13.50) trails MonoScene (14.20) but shows *higher precision*, likely from frustum-artifact suppression (cf. Fig. 4). *LiDAR trend.* Dusk often exceeds day due to weaker solar background in near-IR, while night drops with altered return statistics and sparser echoes on low-albedo/specular surfaces, hurting long-range completion.

4.3. Ablations

We ablate GDC, DP-ER, BGV, AMoE-3D (Table 4). Starting from Q0 (ER-only, no GDC, single-grid, no AMoE-3D; 19.19 mIoU), we add: +GDC → 19.58 (+0.39), +DP-ER → 19.89 (+0.31), +BGV → 20.30 (+0.41), +AMoE-3D (full) → 20.56 (+0.26). Gains are additive: GDC stabilizes sampling; DP-ER provides complementary cues; BGV reduces discretization bias; AMoE-3D sharpens edges/contacts without over-smoothing flats. We further provide more detailed per-module ablations, calibration-robustness analysis, temporal aggregation baselines, and resolution scaling results in the supplementary material.

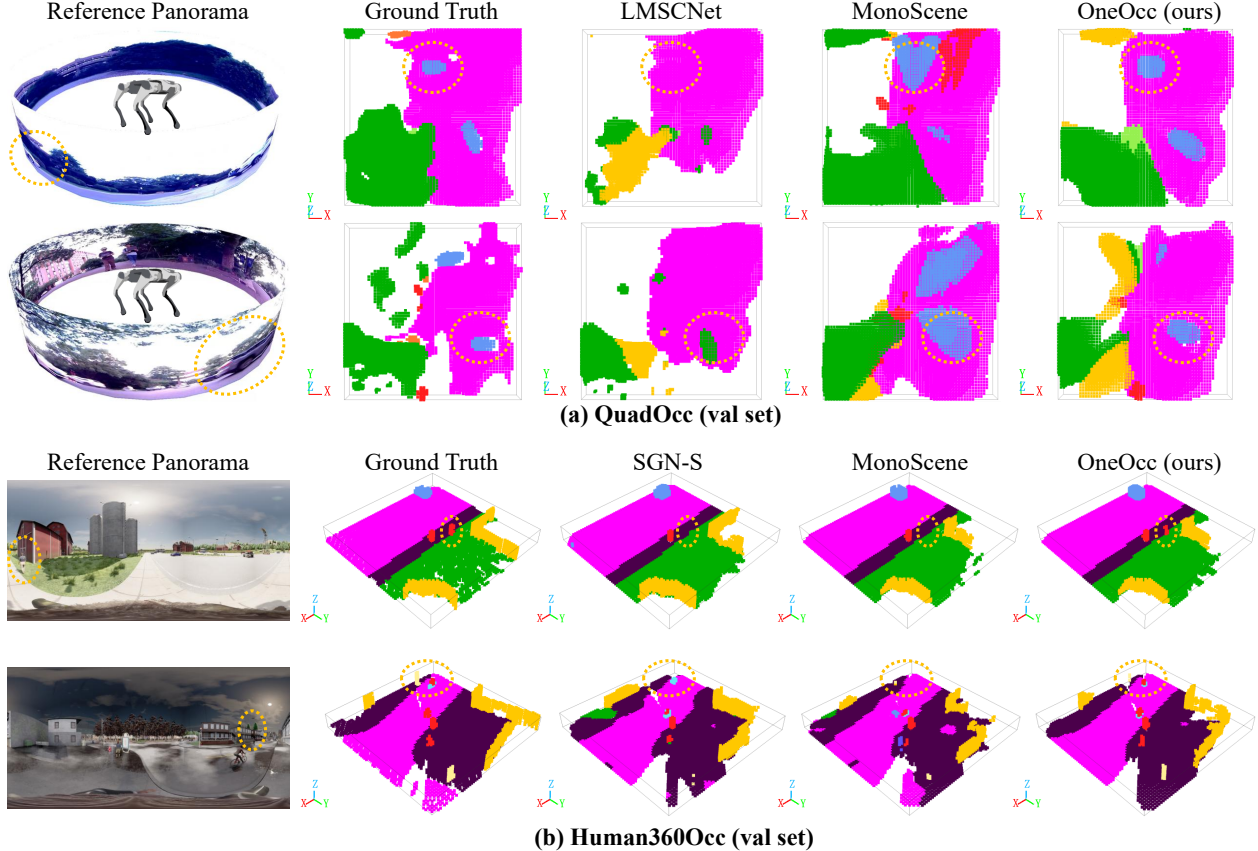


Figure 4. **Qualitative comparisons on (a) *QuadOcc* and (b) *Human360Occ* (val sets).** Left to right: Reference panorama, ground-truth occupancy, baselines, and OneOcc (ours). Across both real (*QuadOcc*) and simulated (*H3O*) panoramic settings, OneOcc better preserves the global layout and 360° continuity, produces cleaner class boundaries, and recovers occluded structures. Yellow dotted circles highlight typical improvements over LMSCNet/SGN-S and MonoScene (e.g., foreground-background disambiguation and far-range layout).

4.4. Qualitative Comparisons

Fig. 4 shows typical cases. On *QuadOcc*, MonoScene exhibits frustum-direction artifacts (ghost elongation), while OneOcc suppresses them via *DP-ER* (cross-view corroboration), *GDC* (phase-stable sampling), and *BGV* (near/far balance). On *Human360Occ*, OneOcc recovers pedestrians close in color to background that competing vision methods miss. Overall, OneOcc preserves global layout and 360° continuity and better handles occlusions.

4.5. Efficiency

Inference on an RTX 4090 at 608×1216 , batch size 1. OneOcc averages 69.93 ms (FPS ≈ 14.30). The model has 101.76M parameters and peaks at 1.82 GB CUDA allocation (2.58 GB reserved) in FP32. With mixed precision (FP32+FP16), latency drops to 52.84 ms (FPS ≈ 18.92), and peak allocation is 1.49 GB. The footprint remains moderate, making OneOcc suitable for onboard legged perception on a single GPU. We additionally report measured on-device runtime and a module-wise latency breakdown on NVIDIA Jetson AGX Orin in the supplementary material.

5. Conclusion

We introduced *OneOcc*, a panoramic *camera-only* framework for semantic occupancy on legged and humanoid platforms. OneOcc stabilizes feature phases under periodic motion via *Gait Displacement Compensation* (GDC), fuses raw annular and equirectangular streams with *Dual-Projection* (DP-ER), balances near-far geometry through *Bi-Grid Voxelization* (BGV), and aggregates multi-scale evidence using a hierarchical *AMoE-3D* decoder. Together, these components turn monocular panoramas into a geometry-aware 3D grid. We also contribute *QuadOcc* (real 360° quadruped) and report cross-domain evaluation on *Human360Occ*, facilitating systematic study across robot morphologies and environments.

Limitations & Outlook. OneOcc assumes accurate calibration with bounded drift. A possible remedy is online extrinsic self-calibration, optionally regularized by lightweight odometry priors. We propose *robotic occupancy* as an intermediate layer for world models and vision-language-action models: tokens for language control, and occupancy-sequence pretraining for cross-robot transfer.

Acknowledgment

This research was funded by the Natural Science Foundation of Zhejiang Province (Grant No. LZ24F050003), the National Natural Science Foundation of China (Grant Nos. 12174341 and 62473139), the Hunan Provincial Research and Development Project (Grant No. 2025QK3019), the MOE AcRF Tier 1 SSHR-TG Incubator Grant FY24 (Grant No. RSTG7/24), and the opening project of the State Key Laboratory of Autonomous Intelligent Unmanned Systems (Grant No. ZZKF2025-2-10). Hao Shi was also supported by the China Scholarship Council (CSC) for joint Ph.D. training at Nanyang Technological University (NTU).

References

- [1] Junming Wang, Xiuxian Guan, Zekai Sun, Tianxiang Shen, Dong Huang, Fangming Liu, and Heming Cui. OMEGA: Efficient occlusion-aware navigation for air-ground robots in dynamic environments via state space model. *IEEE Robotics and Automation Letters*, 2025. 1
- [2] David Hoeller, Nikita Rudin, Christopher Choy, Animesh Anandkumar, and Marco Hutter. Neural scene representation for locomotion on structured terrain. *IEEE Robotics and Automation Letters*, 2022.
- [3] Junming Wang, Zekai Sun, Xiuxian Guan, Tianxiang Shen, Dong Huang, Zongyuan Zhang, Tianyang Duan, Fangming Liu, and Heming Cui. HE-Nav: A high-performance and efficient navigation system for aerial-ground robots in cluttered environments. *IEEE Robotics and Automation Letters*, 2024.
- [4] Junming Wang, Zekai Sun, Xiuxian Guan, Tianxiang Shen, Zongyuan Zhang, Tianyang Duan, Dong Huang, Shixiong Zhao, and Heming Cui. AGRNav: Efficient and energy-saving autonomous navigation for air-ground robots in occlusion-prone environments. In *ICRA*, 2024.
- [5] Akash Patel, Mario Alberto Valdes Saucedo, Nikolaos Stathouloupoulos, Viswa Narayanan Sankaranarayanan, Ilias Tevetzidis, Christoforos Kanellakis, and George Nikolakopoulos. A hierarchical graph-based terrain-aware autonomous navigation approach for complementary multimodal ground-aerial exploration. *arXiv preprint arXiv:2505.14859*, 2025.
- [6] Hongyu Li, Taşkın Pađır, and Huaizu Jiang. StereoNavNet: Learning to navigate using stereo cameras with auxiliary occupancy voxels. In *IROIS*, 2024. 1
- [7] Shun Nijjima, Ryoichi Tsuzaki, Noriaki Takasugi, and Masaya Kinoshita. Real-time multi-plane segmentation based on GPU accelerated high-resolution 3D voxel mapping for legged robot locomotion. *arXiv preprint arXiv:2510.01592*, 2025. 1
- [8] Yinzhaodong, Ji Ma, Liu Zhao, Wanyue Li, and Peng Lu. MARG: Mastering risky gap terrains for legged robots with elevation mapping. *IEEE Transactions on Robotics*, 2025.
- [9] Alejandro Escontrela, Justin Kerr, Arthur Allshire, Jonas Frey, Rocky Duan, Carmelo Sferrazza, and Pieter Abbeel. GaussGym: An open-source real-to-sim framework for learning locomotion from pixels. *arXiv preprint arXiv:2510.15352*, 2025.
- [10] Yeke Chen, Ji Ma, Zeren Luo, Yimin Han, Yinzhaodong, Bowen Xu, and Peng Lu. Learning autonomous and safe quadruped traversal of complex terrains using multi-layer elevation maps. *IEEE Robotics and Automation Letters*, 2025. 1
- [11] Rainer Kartmann, Danqing Liu, and Tamim Asfour. Semantic scene manipulation based on 3D spatial object relations and language instructions. In *Humanoids*, 2021. 1
- [12] Nils Dengler, Jesper Mücke, Rohit Menon, and Maren Bennewitz. Efficient manipulation-enhanced semantic mapping with uncertainty-informed action selection. In *Humanoids*, 2025.
- [13] Ying Li, Xiaobao Wei, Xiaowei Chi, Yuming Li, Zhongyu Zhao, Hao Wang, Ningning Ma, Ming Lu, and Shanghang Zhang. ManipDreamer3D: Synthesizing plausible robotic manipulation video with occupancy-aware 3D trajectory. *arXiv preprint arXiv:2509.05314*, 2025.
- [14] Kaijun Wang, Liqin Lu, Mingyu Liu, Jianuo Jiang, Zeju Li, Bolin Zhang, Wancai Zheng, Xinyi Yu, Hao Chen, and Chunhua Shen. ODYSSEY: Open-world quadrupeds exploration and manipulation for long-horizon tasks. *arXiv preprint arXiv:2508.08240*, 2025. 1
- [15] Yuqi Wu, Wenzhao Zheng, Sicheng Zuo, Yuanhui Huang, Jie Zhou, and Jiwen Lu. EmbodiedOcc: Embodied 3D occupancy prediction for vision-based online scene understanding. In *ICCV*, 2025. 1
- [16] Hao Wang, Xiaobao Wei, Xiaoan Zhang, Jianing Li, Chengyu Bai, Ying Li, Ming Lu, Wenzhao Zheng, and Shanghang Zhang. EmbodiedOcc++: Boosting embodied 3D occupancy prediction with plane regularization and uncertainty sampler. In *MM*, 2025.
- [17] Xinpeng Liu, Haowen Hou, Yanchao Yang, Yong-Lu Li, and Cewu Lu. Revisit human-scene interaction via space occupancy. In *ECCV*, 2024. 1
- [18] Quan Lai, Haifeng Zheng, Xinxin Feng, Mingkui Zheng, Huacong Chen, and Wenqiang Chen. RTONet: Real-time occupancy network for semantic scene completion. *IEEE Robotics and Automation Letters*, 2024. 1
- [19] Helin Cao and Sven Behnke. SLCF-Net: Sequential LiDAR-camera fusion for semantic scene completion using a 3D recurrent U-Net. In *ICRA*, 2024.
- [20] Yuxiang Yan, Boda Liu, Jianfei Ai, Qinbu Li, Ru Wan, and Jian Pu. PointSSC: A cooperative vehicle-infrastructure point cloud benchmark for semantic scene completion. In *ICRA*, 2024.
- [21] Zhang Zhang, Qiang Zhang, Wei Cui, Shuai Shi, Yijie Guo, Gang Han, Wen Zhao, Hengle Ren, Renjing Xu, and Jian Tang. RoboOcc: Enhancing the geometric and semantic scene understanding for robots. *arXiv preprint arXiv:2504.14604*, 2025. 1, 3
- [22] Nathan Silberman, Derek Hoiem, Pushmeet Kohli, and Rob Fergus. Indoor segmentation and support inference from RGBD images. In *ECCV*, 2012. 2
- [23] Angela Dai, Angel X. Chang, Manolis Savva, Maciej Halber, Thomas A. Funkhouser, and Matthias Nießner. Scan-

- Net: Richly-annotated 3D reconstructions of indoor scenes. In *CVPR*, 2017. 2
- [24] Shuran Song, Fisher Yu, Andy Zeng, Angel X. Chang, Manolis Savva, and Thomas A. Funkhouser. Semantic scene completion from a single depth image. In *CVPR*, 2017. 2, 5, 7, 36, 37, 38
- [25] Yancheng Pan, Biao Gao, Jilin Mei, Sibao Geng, Chengkun Li, and Huijing Zhao. SemanticPOSS: A point cloud dataset with large quantity of dynamic instances. In *IV*, 2020. 2
- [26] Jens Behley, Martin Garbade, Andres Milioto, Jan Quenzel, Sven Behnke, Cyrill Stachniss, and Jürgen Gall. SemanticKITTI: A dataset for semantic scene understanding of LiDAR sequences. In *ICCV*, 2019. 2, 15, 30, 31, 32, 34, 35, 36, 37, 38
- [27] Xiaofeng Wang, Zheng Zhu, Wenbo Xu, Yunpeng Zhang, Yi Wei, Xu Chi, Yun Ye, Dalong Du, Jiwen Lu, and Xingang Wang. OpenOccupancy: A large scale benchmark for surrounding semantic occupancy perception. In *ICCV*, 2023. 2
- [28] Xiaoyu Tian, Tao Jiang, Longfei Yun, Yucheng Mao, Huitong Yang, Yue Wang, Yilun Wang, and Hang Zhao. Occ3D: A large-scale 3D occupancy prediction benchmark for autonomous driving. In *NeurIPS*, 2023. 2
- [29] Yiming Li, Sihang Li, Xinhao Liu, Moonjun Gong, Kenan Li, Nuo Chen, Zijun Wang, Zhiheng Li, Tao Jiang, Fisher Yu, Yue Wang, Hang Zhao, Zhiding Yu, and Chen Feng. SSCBench: A large-scale 3D semantic scene completion benchmark for autonomous driving. In *IROS*, 2024. 2
- [30] Song Wang, Jiawei Yu, Wentong Li, Hao Shi, Kailun Yang, Junbo Chen, and Jianke Zhu. Label-efficient semantic scene completion with scribble annotations. In *IJCAI*, 2024. 2
- [31] Lianqing Zheng, Long Yang, Qunshu Lin, Wenjin Ai, Minghao Liu, Shouyi Lu, Jianan Liu, Hongze Ren, Jingyue Mo, Xiaokai Bai, Jie Bai, Zhixiong Ma, and Xichan Zhu. OmniHD-Scenes: A next-generation multimodal dataset for autonomous driving. *arXiv preprint arXiv:2412.10734*, 2024. 2
- [32] Heng Zhai, Jilin Mei, Chen Min, Liang Chen, Fangzhou Zhao, and Yu Hu. WildOcc: A benchmark for off-road 3D semantic occupancy prediction. *arXiv preprint arXiv:2410.15792*, 2024. 2
- [33] Shangwei Guo, Hao Shi, Song Wang, Xiaoting Yin, Kailun Yang, and Kaiwei Wang. Event-aided semantic scene completion. *arXiv preprint arXiv:2502.02334*, 2025. 2, 3, 41
- [34] Chen Min, Jilin Mei, Heng Zhai, Shuai Wang, Tong Sun, Fanjie Kong, Haoyang Li, Fangyuan Mao, Fuyang Liu, Shuo Wang, Yiming Nie, Qi Zhu, Liang Xiao, Dawei Zhao, and Yu Hu. Advancing off-road autonomous driving: The large-scale ORAD-3D dataset and comprehensive benchmarks. *arXiv preprint arXiv:2510.16500*, 2025. 2
- [35] Hanlin Wu, Pengfei Lin, Ehsan Javanmardi, Naren Bao, Bo Qian, Hao Si, and Manabu Tsukada. A synthetic benchmark for collaborative 3D semantic occupancy prediction in V2X autonomous driving. *arXiv preprint arXiv:2506.17004*, 2025. 2
- [36] Xin Lin, Xian Ge, Dizhe Zhang, Zhaoliang Wan, Xianshun Wang, Xiangtai Li, Wenjie Jiang, Bo Du, Dacheng Tao, Ming-Hsuan Yang, and Lu Qi. One flight over the gap: A survey from perspective to panoramic vision. *arXiv preprint arXiv:2509.04444*, 2025. 1
- [37] Tianhe Ren, Shilong Liu, Ailing Zeng, Jing Lin, Kunchang Li, He Cao, Jiayu Chen, Xinyu Huang, Yukang Chen, Feng Yan, Zhaoyang Zeng, Hao Zhang, Feng Li, Jie Yang, Hongyang Li, Qing Jiang, and Lei Zhang. Grounded SAM: Assembling open-world models for diverse visual tasks. *arXiv preprint arXiv:2401.14159*, 2024. 2, 22, 24
- [38] Luis Roldao, Raoul de Charette, and Anne Verroust-Blondet. LMSCNet: Lightweight multiscale 3D semantic completion. In *3DV*, 2020. 2, 5, 7, 18, 36, 37, 41, 43
- [39] Xu Yan, Jiantao Gao, Jie Li, Ruimao Zhang, Zhen Li, Rui Huang, and Shuguang Cui. Sparse single sweep LiDAR point cloud segmentation via learning contextual shape priors from scene completion. In *AAAI*, 2021. 2
- [40] Zhaoyang Xia, Youquan Liu, Xin Li, Xinge Zhu, Yuexin Ma, Yikang Li, Yuenan Hou, and Yu Qiao. SCPNet: Semantic scene completion on point cloud. In *CVPR*, 2023. 2
- [41] Sicheng Zuo, Wenzhao Zheng, Yuanhui Huang, Jie Zhou, and Jiwen Lu. PointOcc: Cylindrical tri-perspective view for point-based 3D semantic occupancy prediction. *arXiv preprint arXiv:2308.16896*, 2023. 2
- [42] Hui Zhou, Xinge Zhu, Xiao Song, Yuexin Ma, Zhe Wang, Hongsheng Li, and Dahua Lin. Cylinder3D: An effective 3D framework for driving-scene LiDAR semantic segmentation. *arXiv preprint arXiv:2008.01550*, 2020. 2, 16
- [43] Song Wang, Jiawei Yu, Wentong Li, Wenyu Liu, Xiaolu Liu, Junbo Chen, and Jianke Zhu. Not all voxels are equal: Hardness-aware semantic scene completion with self-distillation. In *CVPR*, 2024. 2
- [44] Linqing Zhao, Xiuwei Xu, Ziwei Wang, Yunpeng Zhang, Borui Zhang, Wenzhao Zheng, Dalong Du, Jie Zhou, and Jiwen Lu. LowRankOcc: Tensor decomposition and low-rank recovery for vision-based 3D semantic occupancy prediction. In *CVPR*, 2024. 2
- [45] Yukai Ma, Jianbiao Mei, Xuemeng Yang, Licheng Wen, Weihua Xu, Jiangning Zhang, Xingxing Zuo, Botian Shi, and Yong Liu. LiCROcc: Teach radar for accurate semantic occupancy prediction using LiDAR and camera. *IEEE Robotics and Automation Letters*, 2025. 2, 3
- [46] Junming Wang, Wei Yin, Xiaoxiao Long, Xingyu Zhang, Zebin Xing, Xiaoyang Guo, and Qian Zhang. OccR-WKV: Rethinking efficient 3D semantic occupancy prediction with linear complexity. In *ICRA*, 2025. 5, 7, 37, 38
- [47] Xuemeng Yang, Hao Zou, Xin Kong, Tianxin Huang, Yong Liu, Wanlong Li, Feng Wen, and Hongbo Zhang. Semantic segmentation-assisted scene completion for LiDAR point clouds. In *IROS*, 2021.
- [48] Hao Zou, Xuemeng Yang, Tianxin Huang, Chujuan Zhang, Yong Liu, Wanlong Li, Feng Wen, and Hongbo Zhang. Up-to-down network: Fusing multi-scale context for 3D semantic scene completion. In *IROS*, 2021.
- [49] Jianbiao Mei, Yu Yang, Mengmeng Wang, Tianxin Huang, Xuemeng Yang, and Yong Liu. SSC-RS: Elevate LiDAR semantic scene completion with representation separation and BEV fusion. In *IROS*, 2023. 2

- [50] Anh-Quan Cao and Raoul de Charette. MonoScene: Monocular 3D semantic scene completion. In *CVPR*, 2022. 2, 5, 6, 7, 14, 20, 21, 22, 30, 31, 39, 40, 41, 42, 43
- [51] Yiming Li, Zhiding Yu, Christopher B. Choy, Chaowei Xiao, José M. Álvarez, Sanja Fidler, Chen Feng, and Anima Anandkumar. VoxFormer: Sparse voxel transformer for camera-based 3D semantic scene completion. In *CVPR*, 2023. 2, 5, 6, 7, 16, 32, 33, 34, 35
- [52] Yunpeng Zhang, Zheng Zhu, and Dalong Du. OccFormer: Dual-path transformer for vision-based 3D semantic occupancy prediction. In *ICCV*, 2023. 2, 5, 6, 7, 34, 35, 36
- [53] Mingjie Pan, Jiaming Liu, Renrui Zhang, Peixiang Huang, Xiaoqi Li, Hongwei Xie, Bing Wang, Li Liu, and Shanghang Zhang. RenderOcc: Vision-centric 3D occupancy prediction with 2D rendering supervision. In *ICRA*, 2024. 3
- [54] Zhenxing Ming, Julie Stephany Berrio, Mao Shan, and Stewart Worrall. InverseMatrixVT3D: An efficient projection matrix-based approach for 3D occupancy prediction. In *IROS*, 2024. 3
- [55] Rodrigo Marcuzzi, Lucas Nunes, Elias Marks, Louis Wiesmann, Thomas Läbe, Jens Behley, and Cyrill Stachniss. Sf-mOcc: Vision-based 3D semantic occupancy prediction in urban environments. *IEEE Robotics and Automation Letters*, 2025. 3
- [56] Pin Tang, Zhongdao Wang, Guoqing Wang, Jilai Zheng, Xiangxuan Ren, Bailan Feng, and Chao Ma. SparseOcc: Rethinking sparse latent representation for vision-based semantic occupancy prediction. In *CVPR*, 2024. 3
- [57] Yujie Xue, Ruihui Li, Fan Wu, Zhuo Tang, Kenli Li, and Mingxing Duan. Bi-SSC: Geometric-semantic bidirectional fusion for camera-based 3D semantic scene completion. In *CVPR*, 2024.
- [58] Aleksandar Jevtić, Christoph Reich, Felix Wimbauer, Oliver Hahn, Christian Rupprecht, Stefan Roth, and Daniel Cremers. Feed-forward SceneDINO for unsupervised semantic scene completion. In *ICCV*, 2025. 3
- [59] Enyu Liu, En Yu, Sijia Chen, and Wenbing Tao. Disentangling instance and scene contexts for 3D semantic scene completion. In *ICCV*, 2025. 3
- [60] Dubing Chen, Huan Zheng, Yucheng Zhou, Xianfei Li, Wenlong Liao, Tao He, Pai Peng, and Jianbing Shen. Semantic causality-aware vision-based 3D occupancy prediction. In *ICCV*, 2025. 3
- [61] Hyo-Jun Lee, Yeong Jun Koh, Hanul Kim, Hyunseop Kim, Yonguk Lee, and Jinu Lee. SOAP: Vision-centric 3D semantic scene completion with scene-adaptive decoder and occluded region-aware view projection. In *CVPR*, 2025. 3
- [62] Haoang Lu, Yuanqi Su, Xiaoning Zhang, Longjun Gao, Yu Xue, and Le Wang. VisHall3D: Monocular semantic scene completion from reconstructing the visible regions to hallucinating the invisible regions. In *ICCV*, 2025. 3
- [63] Hao Shi, Song Wang, Jiaming Zhang, Xiaoting Yin, Guangming Wang, Jianke Zhu, Kailun Yang, and Kaiwei Wang. Offboard occupancy refinement with hybrid propagation for autonomous driving. *IEEE Transactions on Intelligent Transportation Systems*, 2025. 3, 16, 40
- [64] Hyun-Kurl Jang, Jihun Kim, Hyeokjun Kweon, and Kuk-Jin Yoon. TALoS: Enhancing semantic scene completion via test-time adaptation on the line of sight. In *NeurIPS*, 2024. 3
- [65] Wanshui Gan, Fang Liu, Hongbin Xu, Ningkai Mo, and Naoto Yokoya. GaussianOcc: Fully self-supervised and efficient 3D occupancy estimation with gaussian splatting. *arXiv preprint arXiv:2408.11447*, 2024. 3
- [66] Simon Boeder, Fabian Gigengack, and Benjamin Risse. GaussianFlowOcc: Sparse and weakly supervised occupancy estimation using gaussian splatting and temporal flow. *arXiv preprint arXiv:2502.17288*, 2025. 3
- [67] Yuanhui Huang, Wenzhao Zheng, Yunpeng Zhang, Jie Zhou, and Jiwen Lu. GaussianFormer: Scene as gaussians for vision-based 3D semantic occupancy prediction. In *ECCV*, 2024. 3
- [68] Yuanhui Huang, Amonnut Thammatadatrakoon, Wenzhao Zheng, Yunpeng Zhang, Dalong Du, and Jiwen Lu. GaussianFormer-2: Probabilistic gaussian superposition for efficient 3D occupancy prediction. In *CVPR*, 2025. 3
- [69] Chaofan Wu, Jiaheng Li, Jinghao Cao, Ming Li, Sidan Du, and Yang Li. OmniOcc: Cylindrical voxel-based semantic occupancy prediction for omnidirectional vision systems. *IEEE Access*, 2025. 3
- [70] Xianghui Pan, Jiayuan Du, Shuai Su, Wenhao Zong, Xiao Wang, Chengju Liu, and Qijun Chen. GenerOcc: Self-supervised framework of real-time 3D occupancy prediction for monocular generic cameras. In *IROS*, 2024. 3
- [71] Zhenxing Ming, Julie Stephany Berrio, Mao Shan, Yaoqi Huang, Hongyu Lyu, Nguyen Hoang Khoi Tran, Tzu-Yun Tseng, and Stewart Worrall. OccCylindrical: Multi-modal fusion with cylindrical representation for 3D semantic occupancy prediction. *arXiv preprint arXiv:2505.03284*, 2025. 3
- [72] Lianqing Zheng, Jianan Liu, Runwei Guan, Long Yang, Shouyi Lu, Yuanzhe Li, Xiaokai Bai, Jie Bai, Zhixiong Ma, Hui-Liang Shen, and Xichan Zhu. Doracamom: Joint 3D detection and occupancy prediction with multi-view 4D radars and cameras for omnidirectional perception. *arXiv preprint arXiv:2501.15394*, 2025. 3
- [73] Jingyi Pan, Zipeng Wang, and Lin Wang. Co-Occ: Coupling explicit feature fusion with volume rendering regularization for multi-modal 3D semantic occupancy prediction. *IEEE Robotics and Automation Letters*, 2024. 3
- [74] Heng Li, Yuenan Hou, Xiaohan Xing, Yuexin Ma, Xiao Sun, and Yanyong Zhang. OccMamba: Semantic occupancy prediction with state space models. In *CVPR*, 2025.
- [75] Long Yang, Lianqing Zheng, Wenjin Ai, Minghao Liu, Sen Li, Qunshu Lin, Shengyu Yan, Jie Bai, Zhixiong Ma, and Xichan Zhu. MetaOcc: Spatio-temporal fusion of surround-view 4D radar and camera for 3D occupancy prediction with dual training strategies. *arXiv preprint arXiv:2501.15384*, 2025. 3
- [76] Chengyang Zhang, Jiashi Zhang, Jun Wu, and Qiuguo Zhu. Vision-assisted localization and terrain reconstruction with quadruped robots. In *IROS*, 2022. 3
- [77] Manthan Patel, Fan Yang, Yuheng Qiu, Cesar Cadena, Sebastian A. Scherer, Marco Hutter, and Wenshan Wang. TartanGround: A large-scale dataset for ground robot per-

- ception and navigation. *arXiv preprint arXiv:2505.10696*, 2025. 3
- [78] Ganyu Deng, Jianwen Luo, Caiming Sun, Dongwei Pan, Longyao Peng, Ning Ding, and Aidong Zhang. Vision-based navigation for a small-scale quadruped robot pegasus-mini. In *ROBIO*, 2021. 3
- [79] Sebastian Egidius, Dennis Hadjivelichkov, Jianhao Jiao, Jonathan Embley-Riches, and Dimitrios Kanoulas. Watch your STEPP: Semantic traversability estimation using pose projected features. In *ICRA*, 2025.
- [80] Minh Oh, Byeongho Yu, I Made Aswin Nahrendra, Seoyeon Jang, Hyeonwoo Lee, Dongkyu Lee, Seungjae Lee, Yeeun Kim, Kevin Christiansen Marsim, Hyungtae Lim, and Hyun Myung. TRIP: Terrain traversability mapping with risk-aware prediction for enhanced online quadrupedal robot navigation. *arXiv preprint arXiv:2411.17134*, 2024. 3
- [81] Zhengcai Cao, Junnian Li, Shibo Shao, Dong Zhang, and Mengchu Zhou. Siamese adaptive network-based accurate and robust visual object tracking algorithm for quadrupedal robots. *IEEE Transactions on Cybernetics*, 2025. 3
- [82] Shuo Xin, Zhen Zhang, Liang Liu, Xiaojun Hou, Deye Zhu, Mengmeng Wang, and Yong Liu. A robotic-centric paradigm for 3D human tracking under complex environments using multi-modal adaptation. In *IROS*, 2024. 3
- [83] Yuting Mei, Ye Wang, Sipeng Zheng, and Qin Jin. QuadrupedGPT: Towards a versatile quadruped agent in open-ended worlds. *arXiv preprint arXiv:2406.16578*, 2024. 3
- [84] ByungOk Han, Woo-han Yun, Beom-Su Seo, and Jaehong Kim. Space-aware instruction tuning: Dataset and benchmark for guide dog robots assisting the visually impaired. *arXiv preprint arXiv:2502.07183*, 2025. 3
- [85] Songbo Li, Shixin Luo, Jun Wu, and Qiuguo Zhu. MOVE: Multi-skill omnidirectional legged locomotion with limited view in 3D environments. *arXiv preprint arXiv:2412.03353*, 2024. 3
- [86] Yi Cheng, Hang Liu, Guoping Pan, Houde Liu, and Linqi Ye. Quadruped robot traversing 3D complex environments with limited perception. In *IROS*, 2024.
- [87] Zifan Wang, Teli Ma, Yufei Jia, Xun Yang, Jiaming Zhou, Wenlong Ouyang, Qiang Zhang, and Junwei Liang. Omni-Perception: Omnidirectional collision avoidance for legged locomotion in dynamic environments. In *CoRL*, 2025. 3
- [88] Kai Luo, Hao Shi, Sheng Wu, Fei Teng, Mengfei Duan, Chang Huang, Yuhang Wang, Kaiwei Wang, and Kailun Yang. Omnidirectional multi-object tracking. In *CVPR*, 2025. 3
- [89] Jianping Li, Zhongyuan Liu, Xinhang Xu, Jinxin Liu, Shenghai Yuan, Fang Xu, and Lihua Xie. LiMo-Calib: On-site fast LiDAR-motor calibration for quadruped robot-based panoramic 3D sensing system. *arXiv preprint arXiv:2502.12655*, 2025. 3
- [90] Boyi Liu, Qianyi Zhang, Qiang Yang, Jianhao Jiao, Jagmohan Chauhan, and Dimitrios Kanoulas. The starlink robot: A platform and dataset for mobile satellite communication. *arXiv preprint arXiv:2506.19781*, 2025. 3
- [91] Gang Chen, Zhaoying Wang, Wei Dong, and Javier Alonso-Mora. Particle-based instance-aware semantic occupancy mapping in dynamic environments. *IEEE Transactions on Robotics*, 2025. 3
- [92] Wei Cui, Haoyu Wang, Wenkang Qin, Yijie Guo, Gang Han, Wen Zhao, Jiahang Cao, Zhang Zhang, Jiaru Zhong, Jingkai Sun, Pihai Sun, Shuai Shi, Botuo Jiang, Jiahao Ma, Jiaxu Wang, Hao Cheng, Zhichao Liu, Yang Wang, Zheng Zhu, Guan Huang, Jian Tang, and Qiang Zhang. Humanoid occupancy: Enabling a generalized multimodal occupancy perception system on humanoid robots. *arXiv preprint arXiv:2507.20217*, 2025. 3
- [93] Qiang Zhang, Zhang Zhang, Wei Cui, Jingkai Sun, Jiahang Cao, Yijie Guo, Gang Han, Wen Zhao, Jiaxu Wang, Chenghao Sun, Lingfeng Zhang, Hao Cheng, Yujie Chen, Lin Wang, Jian Tang, and Renjing Xu. HumanoidPano: Hybrid spherical panoramic-LiDAR cross-modal perception for humanoid robots. *arXiv preprint arXiv:2503.09010*, 2025.
- [94] Zhang Zhang, Qiang Zhang, Wei Cui, Shuai Shi, Yijie Guo, Gang Han, Wen Zhao, Jingkai Sun, Jiahang Cao, Jiaxu Wang, Hao Cheng, Xiaozhu Ju, Zhengping Che, Renjing Xu, and Jian Tang. Occupancy world model for robots. *arXiv preprint arXiv:2505.05512*, 2025. 3
- [95] Davide Scaramuzza, Agostino Martinelli, and Roland Siegwart. A toolbox for easily calibrating omnidirectional cameras. In *IROS*, 2006. 4, 22, 23, 24, 30, 31, 32
- [96] Jianbiao Mei, Yu Yang, Mengmeng Wang, Junyu Zhu, Jongwon Ra, Yukai Ma, Laijian Li, and Yong Liu. Camera-based 3D semantic scene completion with sparse guidance network. *IEEE Transactions on Image Processing*, 2024. 5, 6, 7, 31, 32, 33, 34, 39, 40, 42, 43
- [97] Lvmin Zhang, Anyi Rao, and Maneesh Agrawala. Adding conditional control to text-to-image diffusion models. In *ICCV*, 2023. 5
- [98] Xuweiyi Chen, Wentao Zhou, Aruni RoyChowdhury, and Zezhou Cheng. Point-MoE: Towards cross-domain generalization in 3D semantic segmentation via mixture-of-experts. *arXiv preprint arXiv:2505.23926*, 2025. 14
- [99] Yaohua Zha, Tao Dai, Hang Guo, Yanzi Wang, Bin Chen, Ke Chen, and Shu-Tao Xia. Point cloud mixture-of-domain-experts model for 3D self-supervised learning. In *IJCAI*, 2025. 14
- [100] Shaohua Gao, Kailun Yang, Hao Shi, Kaiwei Wang, and Jian Bai. Review on panoramic imaging and its applications in scene understanding. *IEEE Transactions on Instrumentation and Measurement*, 2022. 22
- [101] Wei Xu, Yixi Cai, Dongjiao He, Jiarong Lin, and Fu Zhang. FAST-LIO2: Fast direct LiDAR-inertial odometry. *IEEE Transactions on Robotics*, 2022. 22, 24
- [102] Alexey Dosovitskiy, German Ros, Felipe Codevilla, Antonio Lopez, and Vladlen Koltun. CARLA: An open urban driving simulator. In *CoRL*, 2017. 26
- [103] Marius Cordts, Mohamed Omran, Sebastian Ramos, Timo Rehfeld, Markus Enzweiler, Rodrigo Benenson, Uwe Franke, Stefan Roth, and Bernt Schiele. The cityscapes dataset for semantic urban scene understanding. In *CVPR*, 2016. 28

- [104] Ilya Loshchilov and Frank Hutter. Decoupled weight decay regularization. In *ICLR*, 2019. [30](#), [31](#)
- [105] Clément Godard, Oisín Mac Aodha, Michael Firman, and Gabriel J. Brostow. Digging into self-supervised monocular depth estimation. In *CVPR*, 2019. [32](#), [33](#)
- [106] Jonah Philion and Sanja Fidler. Lift, splat, shoot: Encoding images from arbitrary camera rigs by implicitly unprojecting to 3D. In *ECCV*, 2020. [34](#), [35](#)
- [107] Bowen Cheng, Ishan Misra, Alexander G Schwing, Alexander Kirillov, and Rohit Girdhar. Masked-attention mask transformer for universal image segmentation. In *CVPR*, 2022. [34](#), [35](#)
- [108] Xizhou Zhu, Weijie Su, Lewei Lu, Bin Li, Xiaogang Wang, and Jifeng Dai. Deformable DETR: Deformable transformers for end-to-end object detection. In *ICLR*, 2021. [34](#)
- [109] Mingxing Tan and Quoc V. Le. Efficientnet: Rethinking model scaling for convolutional neural networks. In *ICML*, 2019. [35](#)
- [110] Diederik P. Kingma and Jimmy Ba. Adam: A method for stochastic optimization. *ICLR*, 2015. [36](#), [37](#), [38](#)
- [111] Bernhard Kerbl, Georgios Kopanas, Thomas Leimkühler, and George Drettakis. 3D gaussian splatting for real-time radiance field rendering. *ACM Transactions on Graphics (TOG)*, 2023. [38](#)
- [112] Hao Shi, Qi Jiang, Kailun Yang, Xiaoting Yin, Huajian Ni, and Kaiwei Wang. Beyond the field-of-view: Enhancing scene visibility and perception with clip-recurrent transformer. *IEEE Transactions on Intelligent Vehicles*, 2025. [39](#)
- [113] Zhiyu Tan, Zichao Dong, Cheng Zhang, Weikun Zhang, Hang Ji, and Hao Li. OVO: Open-vocabulary occupancy. *arXiv preprint arXiv:2305.16133*, 2023. [39](#)
- [114] Wenzhao Zheng, Weiliang Chen, Yuanhui Huang, Borui Zhang, Yueqi Duan, and Jiwen Lu. OccWorld: Learning a 3D occupancy world model for autonomous driving. In *ECCV*, 2024. [42](#)
- [115] Sicheng Zuo, Wenzhao Zheng, Yuanhui Huang, Jie Zhou, and Jiwen Lu. GaussianWorld: Gaussian world model for streaming 3D occupancy prediction. In *CVPR*, 2025.
- [116] Tuo Feng, Wenguan Wang, and Yi Yang. Gaussian-based world model: Gaussian priors for voxel-based occupancy prediction and future motion prediction. In *ICCV*, 2025. [42](#)
- [117] Yili Liu, Linzhan Mou, Xuan Yu, Chenrui Han, Sitong Mao, Rong Xiong, and Yue Wang. Let Occ flow: Self-supervised 3D occupancy flow prediction. In *CoRL*, 2024. [42](#)
- [118] Dubing Chen, Jin Fang, Wencheng Han, Xinjing Cheng, Junbo Yin, Chengzhong Xu, Fahad Shahbaz Khan, and Jianbing Shen. ALOcc: Adaptive lifting-based 3D semantic occupancy and cost volume-based flow predictions. In *ICCV*, 2025. [42](#)

6. More Ablations

Setup and notation. Unless stated otherwise, we evaluate on H3O-Heter with the native equirectangular view and report P/R/IoU/mIoU on non-empty voxels. We additionally include QuadOcc only where the raw annulus is required (DP-ER). Grid bounds and taxonomy follow the main paper. For H3O we study both native $64 \times 64 \times 8$ and $128 \times 128 \times 16$ resolutions. Timing is measured with the batch size 1 on a single NVIDIA RTX-4090 GPU (FP32). We report Params (M), FPS, and Mem (GB).

6.1. Hierarchical AMoE-3D: Number of Experts K

Question. How does the number of 3D experts affect accuracy?

Table 6. A1: AMoE-3D experts on H3O-Heter. $K=1$ reduces to a fused bottleneck. Gate is 3D Gradient-Energy by default unless noted. We report precision (P), recall (R), IoU, and mIoU on non-empty voxels under the official H3O-Heter protocol.

K	Gate	P	R	IoU	mIoU
1	–	65.38	61.02	46.12	29.68
2	GradEnergy3D	66.79	63.69	48.37	31.25
4	GradEnergy3D	67.89	64.77	49.58	32.23
8	GradEnergy3D	68.08	64.39	49.46	32.03
4	Uniform	66.21	63.04	47.70	31.13
4	Top- k	67.18	64.06	48.79	31.84

Findings. Increasing K from 1 to 4 consistently improves robustness on H3O-Heter. Moving to $K=8$ slightly increases precision but reduces recall, leading to marginal declines in IoU/mIoU due to expert fragmentation and noisier routing. 3D Gradient-Energy gating (Sec. 3.6) prioritizes high-gradient regions (class boundaries and thin structures), yielding better voxel-wise expert assignment than uniform or naive Top- k routing [98]. $K=4$ achieves the best accuracy–efficiency trade-off and is our default. We also note related progress in point-cloud domain adaptation: Point-MoDE [99] employs a mixture-of-domain-experts to enhance cross-domain generalization, reaching conclusions consistent with ours.

6.2. Horizontal Field-of-View: from 90° to 360°

Question. How much does full 360° surround help, and how do methods degrade when evaluated under narrower FoVs?

Protocol (train-once, test-with-crops). Unless otherwise stated, all methods are trained with full 360° ER panora-

mas. At evaluation time, we reduce the horizontal FoV by cropping the panorama *without finetuning* the models. We use forward-centered cropping so the input spatial extent truly shrinks as the FoV narrows (thereby reflecting realistic compute/memory savings).

Table 7. A2: FoV ablation on H3O-Heter (ER panorama; horizontal crop at eval only; no retraining). We report overall metrics on non-empty voxels. Both OneOcc and MonoScene [50] are *trained once at 360°* , and *evaluated* at narrower FoVs via forward-centered cropping.

FoV	Visible	Method	#Params	FPS \uparrow	Mem \downarrow	P \uparrow	R \uparrow	IoU \uparrow	mIoU \uparrow
90°	25%	MonoScene [50]	146.13M	13.07	1.72GB	56.14	13.59	12.28	4.65
		OneOcc (ours)	101.76M	24.19	1.65GB	58.65	15.43	13.92	7.35
180°	50%	MonoScene [50]	146.13M	12.63	1.78GB	63.40	29.64	25.31	13.74
		OneOcc (ours)	101.76M	19.24	1.70GB	62.68	31.62	26.61	17.27
270°	75%	MonoScene [50]	146.13M	10.08	2.09GB	65.46	41.19	33.84	18.20
		OneOcc (ours)	101.76M	16.13	1.76GB	65.79	47.53	38.11	24.28
360°	100%	MonoScene [50]	146.13M	8.29	2.60GB	67.39	55.00	43.44	24.15
		OneOcc (ours)	101.76M	14.30	1.82GB	67.89	64.77	49.58	32.23

Findings.

- **Train-once, test-with-crops.** For OneOcc, mIoU scales near-monotonically with FoV: $+9.92$ ($90 \rightarrow 180$), $+7.01$ ($180 \rightarrow 270$), and $+7.95$ ($270 \rightarrow 360$), totaling $+24.88$ from 90° to 360° ($+77.2\%$ rel.). MonoScene also improves but less ($+19.50$ total). This indicates that *surround cues translate into long-range context*, with stronger returns when the azimuthal ring is closed.
- **Closing-the-ring effect.** The last increment ($270 \rightarrow 360$) is sizable for both methods, and larger for OneOcc ($+7.95$ vs. $+5.95$ mIoU), evidencing a *nonlinear benefit* when the 360° ring continuity becomes complete.
- **Precision parity, Recall advantage.** OneOcc and MonoScene have similar precision at a given FoV (e.g., 67.89 vs. 67.39 at 360°), while the *recall gap* dominates OneOcc’s advantage: $+9.77$ recall points at 360° (and $+6.34$ at 270°). This matches our design goal: cylindrical alignment and dual-projection preserve azimuthal continuity, yielding *more complete* occupancy recovery as FoV expands.
- **Absolute margins grow with FoV.** OneOcc surpasses MonoScene by $+2.70$ / $+3.53$ / $+6.08$ / $+8.08$ mIoU at $\{90^\circ, 180^\circ, 270^\circ, 360^\circ\}$, respectively. Relative gains are $+58.1\%$, $+25.7\%$, $+33.4\%$, $+33.5\%$.
- **Accuracy–throughput Pareto (AET).** We define $AET = mIoU \times FPS$ to summarize accuracy at a given runtime budget. OneOcc vs. MonoScene AET is:

90° : 177.8 vs 60.8 (**2.93** \times)
 180° : 332.3 vs 173.5 (**1.91** \times)
 270° : 391.6 vs 183.5 (**2.13** \times)
 360° : 460.9 vs 200.2 (**2.30** \times)

Across all FoVs, OneOcc is *Pareto-superior* in

accuracy-throughput.

- **Memory/parameter efficiency.** OneOcc uses 30.3% fewer parameters (101.76M vs. 146.13M). Its mIoU per GB is consistently higher: 4.45 vs. 2.70 (90°), 10.16 vs. 7.72 (180°), 13.80 vs. 8.71 (270°), 17.71 vs. 9.29 (360°), *i.e.*, 1.31–1.91× memory-normalized gains.
- **Practical iso-accuracy choices.** If targeting ~24 mIoU, *OneOcc@270°* achieves 24.28 mIoU at 16.13 FPS and 1.76 GB, matching/exceeding *MonoScene@360°* (24.15 mIoU at 8.29 FPS, 2.60 GB). Thus, for similar accuracy, OneOcc needs ~2× throughput and -0.84 GB memory. Likewise, *OneOcc@180°* (17.27 mIoU, 19.24 FPS) rivals *MonoScene@270°* (18.20 mIoU, 10.08 FPS) at roughly ~1.9× throughput.

Takeaways. Full-surround cues are critical; methods that explicitly encode ring continuity not only achieve higher absolute accuracy, but also deliver better *accuracy-per-compute* and *accuracy-per-memory*. In embodied settings, these advantages persist even when FoV must shrink to meet runtime constraints.

Why an ego-centric 360° symmetric occupancy grid?

Unlike automotive datasets (*e.g.*, front-view grids such as SemanticKITTI [26]) that emphasize a forward driving cone, embodied agents must reason about objects and free space *all around* the ego: turning-in-place, backtracking, and manipulations behind/aside the agent are common. A *symmetrically* centered 360° grid (front/back/left/right balanced) aligns the spatial prior with such behaviors, reduces coordinate bias, and enables globally consistent occlusion reasoning and memory beyond the forward frustum. Empirically, this grid pairs naturally with ring-continuous features and improves cross-directional consistency in long-range context.

6.3. Bi-Grid Voxelization: Cartesian vs. Cylinder

Question. Does the camera-aligned cylindrical grid help beyond a standard Cartesian grid?

Table 8. A3: Single-grid vs. Bi-Grid on H3O-Heter. We stratify *near* using an XY-centered crop (center ratio 0.5, *i.e.*, front/back/left/right ±6.4 m) and *far* using the full XY footprint (±12.8 m); the vertical range is fixed to $z \in [-2, 1.2]$ m.

Voxelization	#Params	FPS ↑	Mem ↓	P ↑	R ↑	IoU ↑	Near mIoU ↑	Far mIoU ↑
Cartesian-only	101.73M	14.32	1.70GB	62.54	63.18	45.84	36.42	30.56
Cylindrical-only	101.73M	14.33	1.78GB	63.65	65.30	47.57	34.15	31.00
Bi-Grid	101.76M	14.30	1.82GB	67.89	64.77	49.58	37.35	32.23

Setup. Unless otherwise stated, we predict occupancy on a Cartesian grid and evaluate within a fixed vertical range

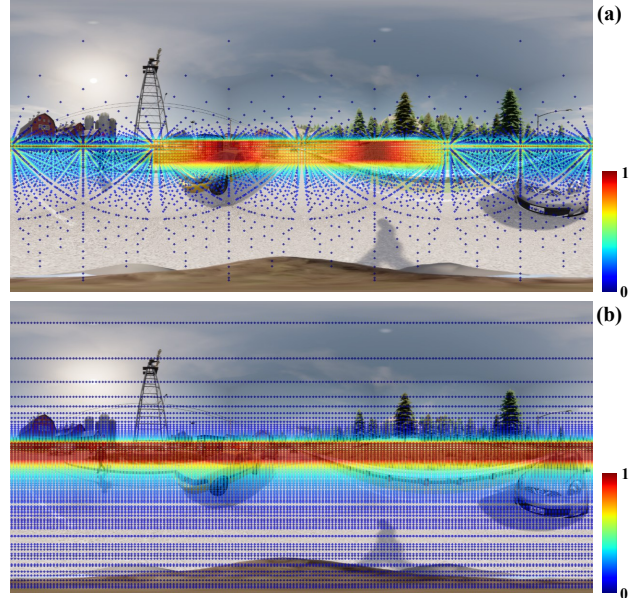


Figure 5. **Cartesian vs. cylindrical voxel projections on a panoramic view.** We visualize how different voxel parameterizations project onto an equirectangular panorama in Human360Occ. Dots denote voxel centroids projected to the image; the colored band (0–1) encodes the normalized depth distribution of occupied voxels along each azimuthal ray. (a) A conventional axis-aligned *Cartesian* grid in world coordinates produces fan-shaped footprints when projected to the panorama: voxels at different heights but similar depth map to tilted rays, and far-range structures such as roads, snow banks, and building façades are squeezed into a narrow band around the equator. This favors metrically uniform sampling in 3D but breaks the angular regularity of the panoramic image. (b) In contrast, an omnidirectional camera-centric *cylindrical* grid uses equal steps in azimuth and height, so the projected voxel centroids form nearly horizontal sampling rows that follow the equirectangular parameterization and maintain ring continuity for distant structures. This complementarity motivates combining both grids in our Bi-Grid voxelization to balance near-field metric fidelity and far-field azimuthal coherence.

$z \in [-2, 1.2]$ m. For range-wise analysis, we follow a panoramic-camera protocol: *near* uses an XY-centered crop with a center ratio of 0.5 (*i.e.*, front/back/left/right ±6.4 m around the ego) and excludes far voxels; *far* uses the full XY footprint (front/back/left/right ±12.8 m). The far split is intrinsically harder due to larger geometric errors, heavier occlusions, sparser voxels, and higher sampling noise, so many classes naturally obtain higher Recall/IoU in the near window, which in turn boosts the near mIoU.

Findings.

- **Complementary inductive biases.** A cylindrical grid (aligned with panoramic camera rays and azimuth) preserves ring continuity and equal-angle sampling, favoring *far-field* layout regularities (roads/sidewalks

bands, building facades). Compared with Cartesian-only, Cylindrical-only raises Recall by +2.12 (65.30 vs. 63.18) and IoU by +1.73, but degrades *near* mIoU by -2.27 (34.15 vs. 36.42), while slightly improving *far* mIoU by +0.44 (31.00 vs. 30.56), echoing Cylinder3D-style observations on cylindrical parameterizations for long-range structure [42].

- **Bi-Grid synergy with negligible overhead.** Our Bi-Grid fuses both discretizations and delivers the best of both worlds: over Cartesian-only it gains +5.35 Precision (67.89 vs. 62.54), +1.59 Recall, and +3.74 IoU, while consistently lifting *both* ranges (near: +0.93, far: +1.67). Against Cylindrical-only, Bi-Grid trades a small Recall drop (-0.53) for a much larger Precision gain (+4.24), resulting in the highest IoU/mIoU overall. The parameter and runtime overhead are minimal (+0.03 M params; ~ 14.3 FPS maintained; +0.12 GB peak memory).
- **Why the overhead is tiny (implementation).** The voxel centroids for both cartesian and cylindrical grids are precomputed and projected to the images in the `dataloader`; at inference we only bilinearly sample 2D features at these fixed locations. We remove the offset-MLP that predicts per-voxel 2D sampling displacements, so the parameter budget barely changes (observed $\Delta \approx +0.03$ M) and throughput remains ~ 14.3 FPS. The main extra cost is memory: Bi-Grid performs two sets of feature samplings and maintains slightly larger activation buffers, causing a modest peak-memory increase (about +0.12 GB).
- **Why Cartesian still matters near the ego.** Evaluation and downstream planners operate on a Euclidean (Cartesian) grid; close-range contact geometry (ground, curbs, thin structures, small objects) benefits from uniform metric spacing and axis-aligned neighborhoods. This explains why Cartesian-only is stronger than Cylindrical-only on *near* mIoU (36.42 vs. 34.15).
- **Panoramic geometry alignment.** With equirectangular/panoramic imaging, cylindrical bins match the camera’s spherical parameterization and mitigate azimuthal aliasing, improving *far*-field coherence; Cartesian bins better preserve metric fidelity and local topology critical for *near*-field planning. Bi-Grid inherits both advantages.
- **Context from SSC/OCC.** Prior occupancy works (e.g., VoxFormer [51], OccFiner [63]) typically report higher short-range fidelity due to denser observations and stronger priors, while accuracy decays with distance. Our *near/far* split makes this explicit: the near window naturally boosts Recall/IoU for many classes, and cylindrical alignment helps counteract the far-range drop; Bi-Grid couples the two.

Takeaways. (i) Cylindrical improves far-field ring coherence but may underfit metric-accurate contact geometry nearby; (ii) Cartesian preserves near-field fidelity but underexploits azimuthal continuity; (iii) For panoramic input with Cartesian output, Bi-Grid is a near-free, robust default that simultaneously improves both *near* and *far* regimes.

6.4. Dual-Projection: ER-only vs. Raw-only

Question. How much does processing both the equirectangular (ER) panorama *and* the raw annulus help?

Setup. All variants share the same backbone/decoder and training schedule; only the input projection path differs. For *ER-only* we unwrap the PAL annulus to equirectangular and feed a single ER encoder. For *Raw-only* we process the native annulus with a single raw-path encoder. *Dual (ER+Raw)* instantiates both encoders and fuses features before 3D lifting. Unless otherwise stated, inference is measured with batch size 1, FP32; ER-based paths use 352×1216 , and Raw-only uses 512×512 . We report wall-clock throughput (FPS) and peak CUDA memory alongside accuracy (Precision *P*, Recall *R*, IoU, mIoU). On H3O (native ER panoramas) we adopt ER-only by default; on QuadOcc (true PAL optics) we compare all three paths.

Table 9. A4: Projection path ablation. On H3O we use ER-only by default (native ER); on QuadOcc we compare ER-only, Raw-only, and Dual (ER+Raw).

Projection Path	#Params	FPS \uparrow	Mem \downarrow	P \uparrow	R \uparrow	IoU \uparrow	mIoU \uparrow
ER-only	101.76M	18.15	1.71GB	65.77	64.81	48.47	20.03
Raw-only	101.97M	25.18	1.55GB	66.42	62.86	47.70	19.76
Dual (ER+Raw)	189.83M	15.46	2.14GB	66.69	64.74	48.92	20.56

Findings.

- **Accuracy on QuadOcc.** Dual achieves the best overall occupancy quality, improving over ER-only by +0.45 IoU and +0.53 mIoU (48.92/20.56 vs. 48.47/20.03), with higher precision (66.69 vs. 65.77) at essentially unchanged recall (64.74 vs. 64.81). Raw-only is weaker on IoU/mIoU (47.70/19.76), indicating that using the raw annulus *alone* is insufficient for best voxel quality.
- **Cost/efficiency.** Relative to ER-only, Dual increases parameters by +86.5% (189.83M vs. 101.76M) and peak memory by +25.1% (2.14 GB vs. 1.71 GB), while throughput drops by 14.8% (15.46 vs. 18.15 FPS). Raw-only is the fastest (25.18 FPS; +38.7% vs. ER-only) and most memory-frugal (1.55 GB), but sacrifices recall (-1.95) and IoU (-0.77).
- **H3O (native ER).** When inputs are already native ER panoramas, the *incremental* benefit of adding a raw

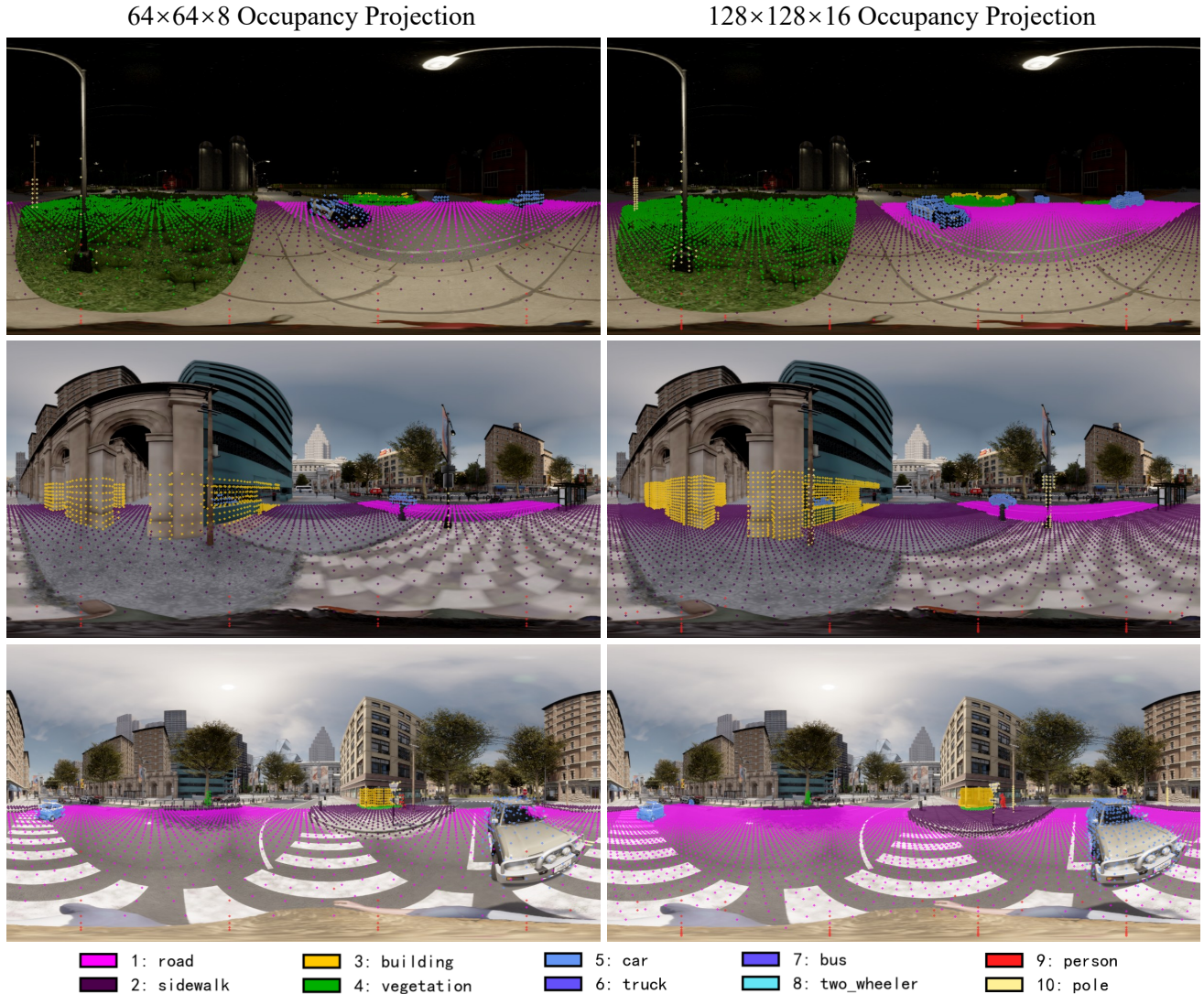


Figure 6. **Semantic ground-truth occupancy projections at different voxel resolutions.** We visualize the projection of *ground-truth* semantic voxels from grids of size $64 \times 64 \times 8$ (left) and $128 \times 128 \times 16$ (right) onto the panoramic image. Colored dots follow the legend at the bottom and indicate voxel centers of different semantic classes relevant to legged locomotion, such as road, sidewalk, buildings, vegetation, vehicles, pedestrians, and poles. The higher-resolution $128 \times 128 \times 16$ grid produces visually denser and more detailed occupancy patterns, with sharper boundaries and more finely sampled thin structures. However, the coarser $64 \times 64 \times 8$ grid still provides sufficient spatial coverage and granularity for a legged robot to perceive traversable surfaces and nearby obstacles in 360° around the body. Considering the computation and payload constraints of embodied agents, we adopt $64 \times 64 \times 8$ as the default resolution for main results on both datasets.

path is marginal relative to its compute/memory overhead; ER-only is the practical setting.

Why Dual helps on QuadOcc (true PAL). A PAL camera forms a circular annulus on the sensor. Unwrapping to ER is convolution-friendly and keeps azimuthal continuity, but induces latitude-dependent distortion and can smooth out high-frequency structures near the inner/outer rings. The *raw annulus* stream preserves native PAL geometry and local texture statistics; fusing it with the ER stream lets the

network resolve ER-induced distortions and seam/edge artifacts while retaining the global continuity provided by ER. This complementary coverage improves precision (fewer false positives around thin/elongated objects) without hurting recall, thereby nudging IoU/mIoU upward.

Takeaway. For true PAL deployments (QuadOcc-like), Dual (ER+Raw) is a robust choice when accuracy is prioritized over a modest efficiency loss. For native ER inputs (H3O-like), ER-only offers the best accuracy–efficiency trade-off;

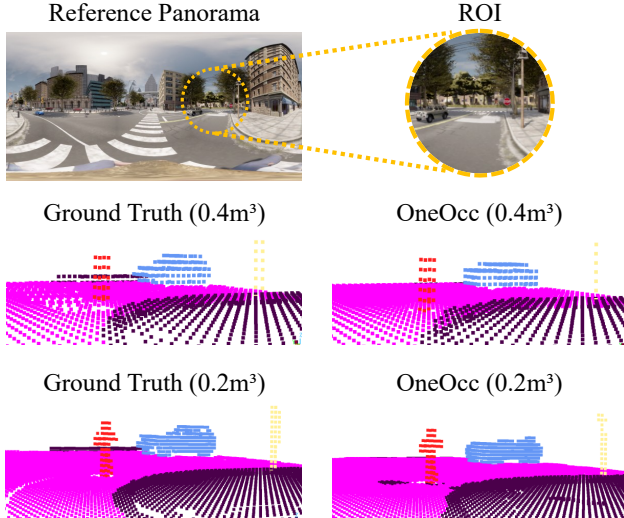


Figure 7. **Voxel grid resolution vs. throughput/accuracy on H3O-Heter.** We keep identical 3D bounds and voxel size; only the grid resolution changes: *BEV* increases from 64×64 to 128×128 while the number of vertical bins increases from 8 to 16. Timings are measured on a single RTX 4090 with batch size 1 (FP32). Raising resolution adds +3.41 M parameters ($101.76 \rightarrow 105.17$ M), reduces FPS ($14.30 \rightarrow 5.01$), and inflates peak memory ($1.82 \rightarrow 10.71$ GB), with a concomitant drop in IoU/mIoU ($49.58/32.23 \rightarrow 29.98/21.16$).

enable Dual only when the last bit of precision is critical.

6.5. Voxel Resolution Scaling

Question. How does performance scale when increasing the voxel grid from $64 \times 64 \times 8$ to $128 \times 128 \times 16$ under identical spatial bounds and training/inference settings?

Setup. We isolate the effect of resolution by fixing the spatial range R , evaluation protocol (*H3O-Heter*), and all model/hyperparameters; only the voxel grid resolution is varied. We report precision (P), recall (R), IoU, and mIoU on non-empty voxels, together with #Params/FPS/Memory measured on a single RTX 4090 (FP32, batch size 1).

Table 10. A5: Resolution scaling on H3O-Heter. Same spatial bounds; only the grid resolution changes.

Resolution	#Params	FPS \uparrow	Mem \downarrow	P \uparrow	R \uparrow	IoU \uparrow	mIoU \uparrow
$64 \times 64 \times 8$	101.76M	14.30	1.82GB	67.89	64.77	49.58	32.23
$128 \times 128 \times 16$	105.17M	5.01	10.71GB	44.69	47.66	29.98	21.16

Findings.

- **Throughput & footprint.** Increasing BEV resolution by $2 \times$ in X/Y and doubling vertical bins ($8 \rightarrow 16$) leaves the backbone almost unchanged in parameter count (+3.41M) but cuts throughput by $\sim 3 \times$ and

raises memory by $\sim 5.9 \times$, as denser 3D feature maps amplify intermediate activations.

- **Accuracy at higher resolution.** Finer-grained occupancy is intrinsically harder: evaluating and *learning* at a denser discretization exacerbates class imbalance and boundary sensitivity, and demands longer-range completion for thin, rare structures. Empirically, our $128 \times 128 \times 16$ setting yields lower aggregate IoU/mIoU than $64 \times 64 \times 8$ despite the finer grid. This trend aligns with multiscale SSC literature (*e.g.*, LMSCNet [38]), where coarse-scale heads are designed for efficiency and are consistently easier to optimize/infer than their fine-scale counterparts¹.
- **Embodied perspective.** Our target use case is *embodied intelligence* with tight on-board compute and memory budgets. Given the $\sim 3 \times$ FPS gain and $\sim 6 \times$ lower memory at $64 \times 64 \times 8$, we adopt this resolution as the *main* setting in the paper: it strikes the best accuracy–efficiency trade-off for real-time, resource-constrained platforms, while $128 \times 128 \times 16$ is reserved for analyses prioritizing geometric detail with a substantial compute penalty.

Therefore, under fixed bounds, $64 \times 64 \times 8$ is the preferred default for accuracy–efficiency in embodied settings; $128 \times 128 \times 16$ offers crisper geometry on slender structures but at markedly worse throughput/memory and lower overall IoU/mIoU.

6.6. Calibration Robustness

Question. How robust is OneOcc to test-time intrinsic/extrinsic calibration perturbations, and can simple calibration-noise augmentation flatten the degradation curve?

Setup. We evaluate robustness on *H3O-Heter* by injecting controlled calibration noise at *data loading time* in the equirectangular projection. Intrinsic perturbation is implemented as a global pixel scaling, while extrinsic perturbation is simulated as per-point pixel offsets. For reproducibility, the perturbation is deterministic for each frame via a fixed seed and frame id, with clipping and FoV-mask update applied accordingly. We report mIoU under three settings: joint intrinsic+extrinsic noise, intrinsic-only noise, and extrinsic-only noise, each with perturbation ratios $p \in \{1\%, 2\%, 5\%\}$. We additionally include robustness-oriented variants retrained with 5% joint calibration-noise augmentation.

Findings.

- **Robustness under calibration perturbation.** Under all corruption levels, OneOcc consistently remains

¹See LMSCNet’s multiscale completion design and coarser-head efficiency.

Table 11. A6: Robustness to intrinsic/extrinsic calibration noise on H3O-Heter. We report mIoU under clean and noisy projections.

Method	Clean 0%	Both (Intr.+Extr.)			Intr. only			Extr. only		
		1%	2%	5%	1%	2%	5%	1%	2%	5%
MonoScene	24.15	21.99	19.58	13.96	22.78	21.00	16.30	22.75	20.69	15.90
OneOcc	32.23	27.26	23.67	16.75	27.88	24.80	19.15	29.42	25.28	18.95
MonoScene [†]	18.97	18.86	18.64	16.48	18.71	18.28	15.74	19.01	19.17	18.92
OneOcc [†]	23.00	22.97	23.03	22.84	22.86	22.84	22.48	22.94	23.15	23.16

[†] Retrained with 5% joint intrinsic+extrinsic calibration-noise augmentation.

above MonoScene. With joint intrinsic+extrinsic noise, OneOcc achieves 27.26/23.67/16.75 mIoU at 1%/2%/5%, outperforming MonoScene by +5.27/+4.09/+2.79, respectively. This indicates that the proposed dual-projection lifting and 3D reasoning pipeline retains stronger geometric consistency under imperfect calibration.

- **Intrinsic vs. extrinsic noise.** Both perturbation types degrade performance, while their combination is the most harmful as expected. Intrinsic-only noise is slightly more disruptive at low-to-moderate levels, likely because global projection-scale distortion affects all lifted features simultaneously, whereas extrinsic perturbation mainly introduces spatial misalignment. Nevertheless, OneOcc preserves a clear margin over the baseline in all settings.
- **Effect of calibration-noise augmentation.** Retraining with simple 5% calibration-noise augmentation substantially flattens the degradation curve. For example, the robustness-oriented OneOcc[†] variant stays nearly constant at 22.97/23.03/22.84 mIoU under 1%/2%/5% joint noise. This comes at the cost of lower clean performance (23.00 vs. 32.23), suggesting a standard robustness–accuracy trade-off: the default model is preferable when calibration is reliable, whereas noise augmentation is attractive for long-term deployment under persistent drift.

Therefore, OneOcc is reasonably robust to bounded calibration errors and consistently more resilient than MonoScene; when stronger calibration drift is expected, simple calibration-noise augmentation can further improve robustness at the expense of clean-set accuracy.

6.7. Temporal Aggregation

Question. Does lightweight temporal aggregation materially improve occupancy prediction, and how does it trade accuracy against latency and memory compared with the default single-frame design?

Setup. We compare the default *single-frame* OneOcc with two simple 3-frame temporal variants under identical image resolution (608×1216), voxel bounds, backbone, and eval-

uation protocol. The first variant performs temporal feature averaging using *ground-truth pose* for alignment, representing a minimal upper-bound baseline with reliable multi-frame registration. The second variant adopts a lightweight BEVFormer-style temporal attention over three frames. We report mIoU on *QuadOcc-val* and *H3O-Heter*, together with latency and memory measured on a single RTX 4090 (FP32, batch size 1).

Table 12. A7: Temporal aggregation vs. the default single-frame design. Temporal fusion improves accuracy, but also increases deployment cost.

Setting	QuadOcc-val mIoU [†]	H3O-Heter mIoU [†]	Latency (ms) [↓]	Memory (GB) [↓]
OneOcc (single-frame)	20.56	32.23	69.93	1.82
+ Temporal average by GT pose (3 frames)	20.92	33.74	69.93	1.82
+ Temporal BEVFormer-like attention (3 frames)	21.18	34.25	78.60	2.35

Findings.

- **Temporal aggregation is beneficial with reliable alignment.** Both 3-frame variants improve over the default single-frame setting. Simple temporal averaging already raises mIoU from 20.56 to 20.92 on QuadOcc-val and from 32.23 to 33.74 on H3O-Heter, confirming that multi-frame context helps suppress transient gait-induced jitter and recover partially occluded structures when alignment is accurate.
- **Stronger temporal fusion yields larger gains but higher cost.** The BEVFormer-style temporal attention further improves mIoU to 21.18 on QuadOcc-val and 34.25 on H3O-Heter, but increases latency from 69.93 ms to 78.60 ms and memory from 1.82 GB to 2.35 GB. This shows that temporal fusion is effective, yet its benefit is not free: better multi-frame reasoning comes with additional state handling, feature fusion overhead, and higher deployment cost.
- **Why single-frame remains the default.** Our goal is an *easy-to-deploy*, *low-latency*, and *odometry-free* embodied perception system. The temporal-average variant relies on ground-truth pose for reliable frame alignment and therefore should be interpreted as an upper-bound reference rather than a plug-and-play deployment mode. In contrast, the default single-frame OneOcc avoids temporal drift accumulation, requires no motion history, and maintains a cleaner inference path for resource-constrained onboard platforms.

Therefore, temporal aggregation can further improve panoramic occupancy prediction when accurate multi-frame alignment is available, but the default single-frame OneOcc remains the preferred setting for real-time embodied deployment due to its simplicity, robustness to drift, and lower system complexity.

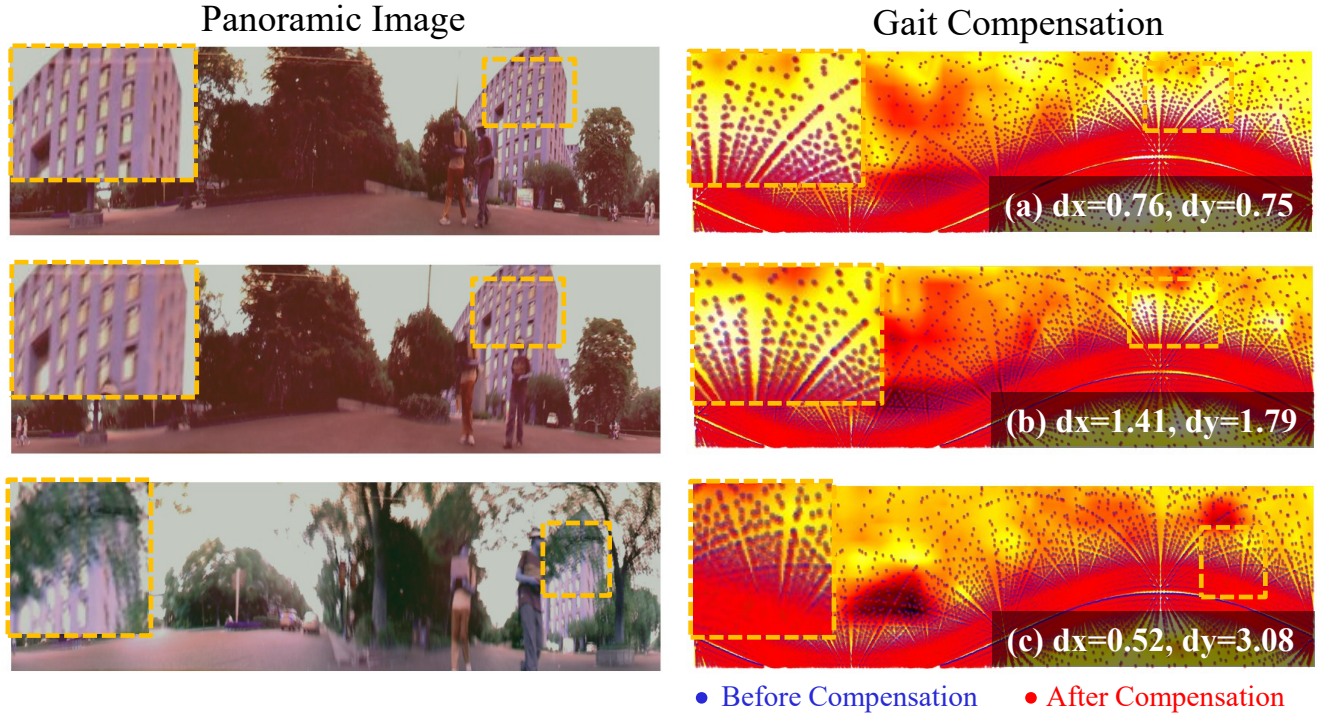


Figure 8. **Panoramic gait displacement compensation on real-world quadruped data.** We visualize the effect of Gait Displacement Compensation (GDC) on our QuadOcc dataset collected by a quadruped robot equipped with a panoramic camera. Each row shows one panorama captured at a different gait intensity: the left column is the input image with a zoom-in of a distant structure, and the right column overlays FLoSP [50] sampling locations on the equirectangular feature map before (blue) and after (red) GDC. From top to bottom, the robot motion changes from mild to pronounced body oscillation, and the estimated vertical offsets dy increase accordingly (see the (dx, dy) values in (a)–(c)), while the horizontal offsets dx remain comparatively small. This indicates that gait-induced jitter produces a characteristic *vertical* motion-blur pattern during exposure, and GDC automatically adapts the strength of its correction mainly along the vertical axis. Although the predicted displacements are real-valued and sometimes fractional, we augmented FLoSP with bilinear interpolation, so sub-pixel shifts of the sampling grid are still meaningful and help recover sharper, less blur-contaminated features for downstream occupancy prediction in this single-frame model.

7. Qualitative Analysis of GDC

Figure 8 provides a qualitative view of GDC on real-world quadruped runs. The three rows correspond to panoramas captured under increasing gait intensity, ranging from mild to pronounced body oscillation. Because the panoramic camera is mounted on a moving body, the gait induces vertical shake during the exposure time and creates a characteristic motion-blur pattern: distant objects and tree lines are smeared mainly along the vertical direction. Without compensation, the fixed FLoSP [50] sampling grid (blue) may query different parts of this blurred streak depending on the current gait phase, effectively mixing background and foreground evidence within a single frame. GDC predicts per-frame offsets that correct this effect: from (a) to (c), the estimated dy increases while dx stays small, showing that the module automatically scales its response with the blur magnitude and focuses almost exclusively on the dominant vertical direction. Note that OneOcc operates purely on single panoramas without temporal aggregation, so GDC

is not used for temporal alignment; instead, it refines the instantaneous feature sampling locations to better match the underlying static geometry under gait-induced motion blur. Since we implemented FLoSP with bilinear interpolation rather than the classic nearest-neighbor lookup [50], the real-valued (often fractional) (dx, dy) still produce meaningful sub-pixel shifts of the sampling grid, which leads to cleaner voxel features and the consistent mIoU gains observed in our ablations.

8. Lightweight Design Philosophy of OneOcc

While Sec. 4.5 of the main paper reports the overall runtime and memory footprint, here we decompose the parameter counts of OneOcc and the MonoScene [50] baseline into their major components. We focus on the panoramic setting on QuadOcc as well as the Human360Occ (H3O) variant.

Table 13. Parameter breakdown on QuadOcc (panorama-only). The additional geometry-aware modules in OneOcc (GDC, BGV-informed volumetric fusion, and the lightweight AMoE-3D gating heads) contribute less than 0.2% of the total parameters. The AMoE-3D attention and expert weights are counted as part of the 3D decoder. Both the 3D decoder and each single 2D encoder are lighter than the MonoScene [50] counterpart.

Method	2D encoder(s)	3D decoder	GDC+fusion+gates	Total
MonoScene (QuadOcc)	1 × 132M	16.9M	–	148.9M
OneOcc (QuadOcc)	2 × 87.8M	12.3M	≈ 0.27M	189.8M

8.1. QuadOcc: dual-projection variant

Tab. 13 summarizes the parameter breakdown when training on QuadOcc with the full dual-projection encoders (DP-ER) and bi-grid voxelization. MonoScene [50] consists of a single 2D encoder operating on the equirectangular panorama and a standard 3D UNet decoder, resulting in 132M parameters for the 2D encoder and 16.9M for the 3D decoder (148.9M total).

In contrast, OneOcc factorizes its capacity across (i) two 2D encoders for raw and equirectangular views (DP-ER), (ii) a lightweight depthwise-separable 3D decoder with Hierarchical AMoE-3D, and (iii) a set of geometry-aware auxiliary modules (GDC, volumetric fusion, and tiny gating heads). Each 2D encoder in DP-ER contains 87.8M parameters, and the DWLite3D decoder with AMoE-3D attention blocks (excluding the gating heads) contains 12.3M. The remaining components—GDC heads, 3D SE/fusion layers, and the lightweight AMoE-3D gating MLPs—add only about 0.27M parameters in total (less than 0.2% of the overall capacity). For clarity, we count the AMoE-3D attention and expert weights inside the “3D decoder” bucket, while the gating networks are included in the “GDC+fusion+gates” bucket in Tab. 13 and Tab. 14.

Although the total parameter count increases by ≈ 26% compared to MonoScene (148.9M → 189.8M), the design is *structurally lightweight*: (1) the 3D decoder is 27% smaller (16.9M → 12.3M) thanks to the depthwise-separable DWLite3D design; (2) each single DP-ER encoder is 33% lighter than MonoScene’s 2D encoder (132M → 87.8M); and (3) the additional geometry-aware modules (GDC, BGV-based fusion, AMoE-3D gates) are extremely cheap in parameters. The modest increase in total parameters on QuadOcc therefore comes almost entirely from using two lighter encoders in parallel, which is amortized by GPU parallelism and justified by the improved robustness under gait-induced jitter.

8.2. H3O: single-projection variant

On Human360Occ (H3O), the images are already native equirectangular, so we follow the main paper and disable the raw-annulus branch in DP-ER and the associated fu-

Table 14. Parameter breakdown on H3O. When the raw panoramic branch is disabled, OneOcc becomes markedly lighter than MonoScene [50] in terms of learned parameters, while preserving GDC, the lightweight AMoE-3D gating heads, and the DWLite3D attention blocks (whose weights are counted inside the 3D decoder).

Method	2D encoder(s)	3D decoder	GDC+gates	Total
MonoScene (H3O)	1 × 132M	16.9M	–	148.9M
OneOcc (H3O)	1 × 87.8M	12.3M	≈ 0.27M	101.7M

sion layers, while keeping the same DWLite3D decoder and GDC. Tab. 14 reports the resulting parameter statistics. MonoScene [50] again uses a single 2D encoder (132M) and the standard 3D decoder (16.9M), totaling 148.9M parameters.

The H3O configuration of OneOcc uses a single 2D encoder (87.8M), the same 12.3M DWLite3D decoder, and the small GDC and gating modules, for a total of ~100M parameters. This corresponds to a reduction of approximately 33% in parameter count compared to MonoScene [50] (148.9M → 101.7M), while retaining all the geometry-aware components that are shown in the main paper ablations to be crucial for far-field context and near-field contact geometry.

8.3. Runtime on NVIDIA Jetson AGX Orin

To complement the parameter analysis above, we further report *measured* runtime on an NVIDIA Jetson AGX Orin 64GB (MAX power mode), which provides a more deployment-realistic efficiency reference than desktop-GPU throughput alone. In particular, we compare OneOcc against MonoScene [50] under the QuadOcc panoramic setting using the native input size $1 \times 3 \times 370 \times 1220$ and batch size 1. All numbers are averaged over 100 runs after 5 warm-up iterations. Following a practical edge-deployment setup, the 2D UNet-style image encoder/decoder is executed in INT8 using TensorRT, while the remaining geometry-aware modules are run in FP16. We decompose the latency into four stages: (i) *2D Enc. + 2D Dec.*, *i.e.*, the image-space feature extraction and decoding backbone; (ii) *Lift2Cart Samp.*, which lifts image features into the Cartesian voxel space; (iii) *Cart2Polar Samp.*, the additional Cartesian-to-polar resampling used only in OneOcc; and (iv) *3D Dec.*, the volumetric decoder operating on lifted features.

As shown in Tab. 15, OneOcc achieves a total latency of 73.32 ms (13.64 FPS), compared with 98.01 ms (10.20 FPS) for MonoScene [50], corresponding to an overall speedup of approximately $1.34 \times$ on the embedded platform. Notably, this gain is achieved *despite* the additional *Cart2Polar Samp.* stage, which is absent in MonoScene. The main reason is that OneOcc reduces computation in

Table 15. Measured runtime breakdown on NVIDIA Jetson AGX Orin 64GB (MAX power mode). Input: $1 \times 3 \times 370 \times 1220$ (QuadOcc panoramas), batch size 1; 5 warm-up iterations + 100 measured runs. The 2D image encoder/decoder is executed in INT8 (TensorRT), while the remaining modules are run in FP16. Despite the extra Cartesian-to-polar resampling step, OneOcc remains faster overall due to its lighter 2D/3D computation.

Method	2D Enc. + 2D Dec.	Lift2Cart Samp.	Cart2Polar Samp.	3D Dec.	Total	FPS
MonoScene	61.97	2.46	<i>n.a.</i>	33.58	98.01	10.20
OneOcc	53.86	2.48	2.40	14.57	73.32	13.64

the dominant stages. In the 2D branch, OneOcc requires 53.86 ms versus 61.97 ms for MonoScene, reflecting the lighter dual-projection image backbone design discussed above. The largest reduction appears in the 3D decoder: OneOcc uses only 14.57 ms, whereas MonoScene requires 33.58 ms. This is consistent with the parameter analysis in Tab. 13–14, where the DWLite3D decoder is substantially lighter than the standard dense 3D UNet decoder. By contrast, the geometry-aware sampling operations are cheap: *Lift2Cart Samp.* is nearly identical for both methods (2.48 ms vs. 2.46 ms), and the extra *Cart2Polar Samp.* in OneOcc adds only 2.40 ms. These measurements support the lightweight positioning of OneOcc from an edge-deployment perspective. Rather than relying only on desktop-GPU throughput or theoretical scaling estimates, the Jetson AGX Orin results show that the proposed design remains practically efficient on an embedded robotics platform while providing stronger panoramic semantic occupancy prediction.

8.4. Discussion

Across both benchmarks, OneOcc follows a consistent lightweight design philosophy: (i) concentrate capacity in flexible 2D encoders that can be reconfigured (dual-projection on QuadOcc vs. single-projection on H3O), (ii) employ a depthwise-separable DWLite3D decoder with Hierarchical AMoE-3D to reduce 3D convolutional cost, and (iii) ensure that geometry-specific modules (GDC, BGV-based volumetric fusion, and the AMoE-3D gating heads that select experts based on GradEnergy) remain extremely parameter-efficient. On QuadOcc, this yields a modest increase in parameters but significantly better panoramic SSC under gait-induced jitter; on H3O, the same architecture, with the redundant projection path removed, becomes *substantially* lighter than MonoScene [50] while still providing clear performance gains.

9. QuadOcc: Dataset Construction

Goal and setting QuadOcc targets full-surround *semantic occupancy* from a *single* omnidirectional panorama on a quadruped robot. Each frame couples an omnidirectional

image captured via Panoramic Annular Lens (PAL) [100] with time-synchronized LiDAR for semi-automatic Ground Truth (GT) construction; outputs are $64 \times 64 \times 8$ semantic volumes at 0.4 m per voxel under a 6-class taxonomy. The dataset comprises 10 scenes and 24K frames across day/dusk/night, reflecting realistic legged operation with moderate speeds and tight payload/power budgets.

9.1. Sensor Suite, Time Sync, and Calibration

We mount on a quadruped a Livox Mid-360 LiDAR (with built-in IMU) and an omnidirectional panoramic annular lens (PAL) camera, time-synchronized by hardware trigger and software timestamp alignment. Let $\mathcal{I} = \{I_t\}$ be panoramic RGB streams and $\mathcal{L} = \{L_t\}$ be LiDAR scans.

PAL (Taylor/OCam) calibration and unwarping. We adopt the generic Taylor (OCam) model [95] for PAL calibration. For an equirectangular pixel $(u, v) \in [0, W) \times [0, H)$ with spherical angles:

$$\phi = \frac{2\pi}{W}u - \pi, \quad \theta = \frac{\pi}{2} - \frac{\pi}{H}v, \quad (15)$$

the corresponding polar radius on the annulus is $r(\theta) = \sum_{i=0}^N a_i \theta^i$, and the raw-annulus coordinates are:

$$\begin{bmatrix} u_{\text{raw}} \\ v_{\text{raw}} \end{bmatrix} = \begin{bmatrix} u_0 \\ v_0 \end{bmatrix} + A r(\theta) \begin{bmatrix} \cos \phi \\ \sin \phi \end{bmatrix}, \quad (16)$$

where $\{a_i\}$, (u_0, v_0) , and $A \in \mathbb{R}^{2 \times 2}$ come from calibration. The unwarped equirectangular image I^{equi} is obtained by sampling the raw annulus I^{raw} at $(u_{\text{raw}}, v_{\text{raw}})$.

9.2. Panoramic Semantic Acquisition

We perform pixel-wise open-vocabulary segmentation on I_t^{equi} with Grounded-SAM [37] using a prompt set \mathcal{P} (e.g., “road”, “vehicle”, “vegetation”), producing a semantic map $S_t \in \{1, \dots, C\}^{H \times W}$ with confidence map Q_t .

9.3. LiDAR–Image Label Transfer

With extrinsics $\mathbf{T}_{L \rightarrow C} \in \text{SE}(3)$ and the PAL intrinsics, a LiDAR point $\mathbf{p}_L \in \mathbb{R}^3$ projects to pixel $\mathbf{u} = \pi(\mathbf{T}_{L \rightarrow C} \tilde{\mathbf{p}}_L)$, where $\tilde{\mathbf{p}}_L$ is in homogeneous coordinates and $\pi(\cdot)$ denotes the PAL projection composed with the equirectangular sampling above. We assign the point label:

$$\ell(\mathbf{p}_L) = S_t(\mathbf{u}), \quad w(\mathbf{p}_L) = Q_t(\mathbf{u}), \quad (17)$$

thus converting costly 3D annotation into robust 2D segmentation.

9.4. Semantic-Guided Dynamic Mapping

We split points into *static* vs. *dynamic* by semantics $\ell(\cdot)$ (e.g., “vehicle”, “pedestrian” as dynamic). A LiDAR-SLAM [101] backend yields a dense global map \mathcal{M} in

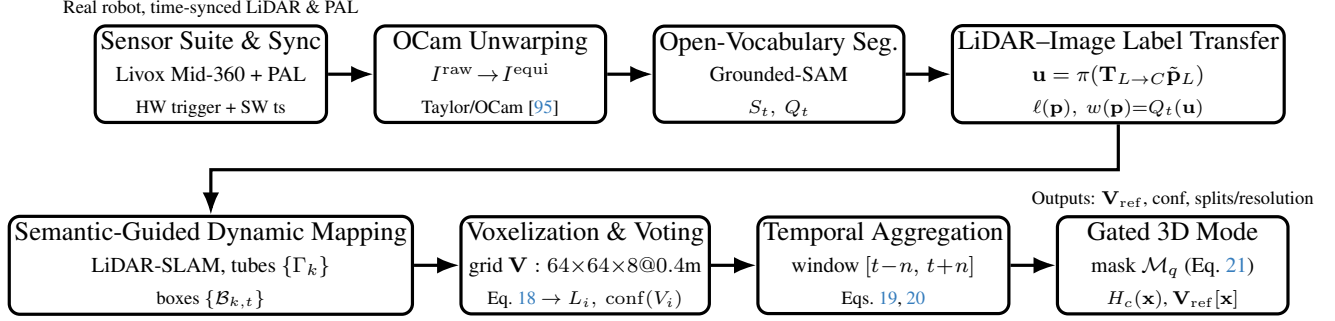


Figure 9. **QuadOcc ground-truth construction pipeline.** From synchronized LiDAR & PAL capture, OCam unwarping and open-vocabulary segmentation provide S_t and Q_t . LiDAR–image label transfer assigns (ℓ, w) to points, followed by semantic-guided dynamic mapping. Voxelization and majority voting (Eq. 18) produce \mathbf{V} ; temporal aggregation (Eqs. 19, 20) and a gated 3D mode with \mathcal{M}_q (Eq. 21) yield the refined volume \mathbf{V}_{ref} .

a world frame. Dynamic instances form *tubes* $\{\Gamma_k\}$ in space-time; each tube provides a motion axis and per-frame bounding boxes $\mathcal{B}_{k,t}$. Background is integrated as static surfels/voxels; dynamic objects are re-inserted in temporal order to preserve their trajectories with minimal manual interaction.

9.5. Voxelization and Majority Voting

We use a fixed occupancy grid $\mathbf{V} \in \{0, \dots, C\}^{X \times Y \times Z}$ (default $64 \times 64 \times 8$ with 0.4 m voxels). Given all points $\{P_{i,j}\}$ in voxel V_i , we take a weighted majority vote:

$$L_i = \arg \max_c \sum_j w(P_{i,j}) \delta(\ell(P_{i,j}), c),$$

$$\text{conf}(V_i) = \frac{\max_c \sum_j \delta(\ell(P_{i,j}), c)}{\sum_j 1}. \quad (18)$$

where $\delta(\cdot, \cdot)$ is the Kronecker delta and $\text{conf}(\cdot)$ is a per-voxel confidence (later used for quality control).

9.6. Temporal Aggregation and Refinement

To suppress flicker and fill occlusions, we aggregate a temporal window $[t-n, t+n]$. All points inside the window are first transformed to the current frame by $\mathbf{T}_\tau^{\text{cur}} \in \text{SE}(3)$:

$$\mathcal{P}_\tau^{\text{cur}} = \mathbf{T}_\tau^{\text{cur}} \mathcal{P}_\tau, \quad \forall \tau \in [t-n, t+n]. \quad (19)$$

Here, \mathcal{P}_τ is the LiDAR point set at time τ and $\mathcal{P}_\tau^{\text{cur}}$ its transformed set. After devoxelization and re-voxelization, we accumulate per-class votes in each voxel and take a temporal majority:

$$\mathbf{V}_{\text{agg}}[x, y, z] = \arg \max_c \sum_{\tau=t-n}^{t+n} \mathbb{I}(\mathcal{P}_\tau^{\text{cur}}(x, y, z) = c). \quad (20)$$

Here, \mathbf{V}_{agg} denote the aggregated label volumes. $\mathbb{I}(\cdot)$ denotes the *indicator function*: $\mathbb{I}(\text{predicate}) = 1$ if the predicate is true and 0 otherwise.

Quantization-aware 3D mode (our implementation).

Let U denote the *ignore/unlabeled* index, and define a quantization mask that flags “empty-vote” voxels (no support from any frame):

$$\mathcal{M}_q[x, y, z] = \mathbb{I}\left(\sum_c \sum_\tau \mathbb{I}(\mathcal{P}_\tau^{\text{cur}}(x, y, z) = c) = 0\right). \quad (21)$$

We then apply a *gated* 3D mode filter only where $\mathcal{M}_q=1$. Using a cubic neighborhood of size $k \times k \times k$ (default $k=5$), and let the local class histogram $H_c(\mathbf{x})$ be:

$$\mathbf{x} = (x, y, z)^\top, \quad \mathcal{N}_k = \{\boldsymbol{\delta} \in \mathbb{Z}^3 : \|\boldsymbol{\delta}\|_\infty \leq \lfloor k/2 \rfloor\}.$$

$$H_c(\mathbf{x}) = \sum_{\boldsymbol{\delta} \in \mathcal{N}_k} \mathbb{I}(\mathbf{V}_{\text{agg}}[\mathbf{x} + \boldsymbol{\delta}] = c). \quad (22)$$

The refined label \mathbf{V}_{ref} is then:

$$\mathbf{V}_{\text{ref}}[\mathbf{x}] = \begin{cases} \arg \max_{c \neq U} H_c(\mathbf{x}), & \mathcal{M}_q[\mathbf{x}] = 1, \\ \mathbf{V}_{\text{agg}}[\mathbf{x}], & \text{otherwise.} \end{cases} \quad (23)$$

Ties and safety: in case of a tie, we keep $\mathbf{V}_{\text{agg}}[\mathbf{x}]$ (no change). If the neighborhood histogram is empty (all U), we fall back to a nearest-neighbor fill in Euclidean space with a small radius (default $r_{\text{max}}=5$ voxels) and still ignore U ; if no valid neighbor exists within r_{max} the voxel remains U . Border handling uses a constant pad (out-of-bounds treated as U). This quantization-aware gating prevents the mode operation from overwriting confident voxels while reliably filling holes introduced by multi-frame alignment and re-voxelization.

9.7. Data Splits, Resolution, and Taxonomy

Our legged/humanoid setting prioritizes reliable near-field awareness under tight onboard compute. We therefore bound the grid to $R = [-X_{\text{max}}, X_{\text{max}}] \times [-Y_{\text{max}}, Y_{\text{max}}] \times [Z_{\text{min}}, Z_{\text{max}}]$ with $X_{\text{max}} = Y_{\text{max}} = 12.8$ m, $Z_{\text{min}} = -2.0$ m,

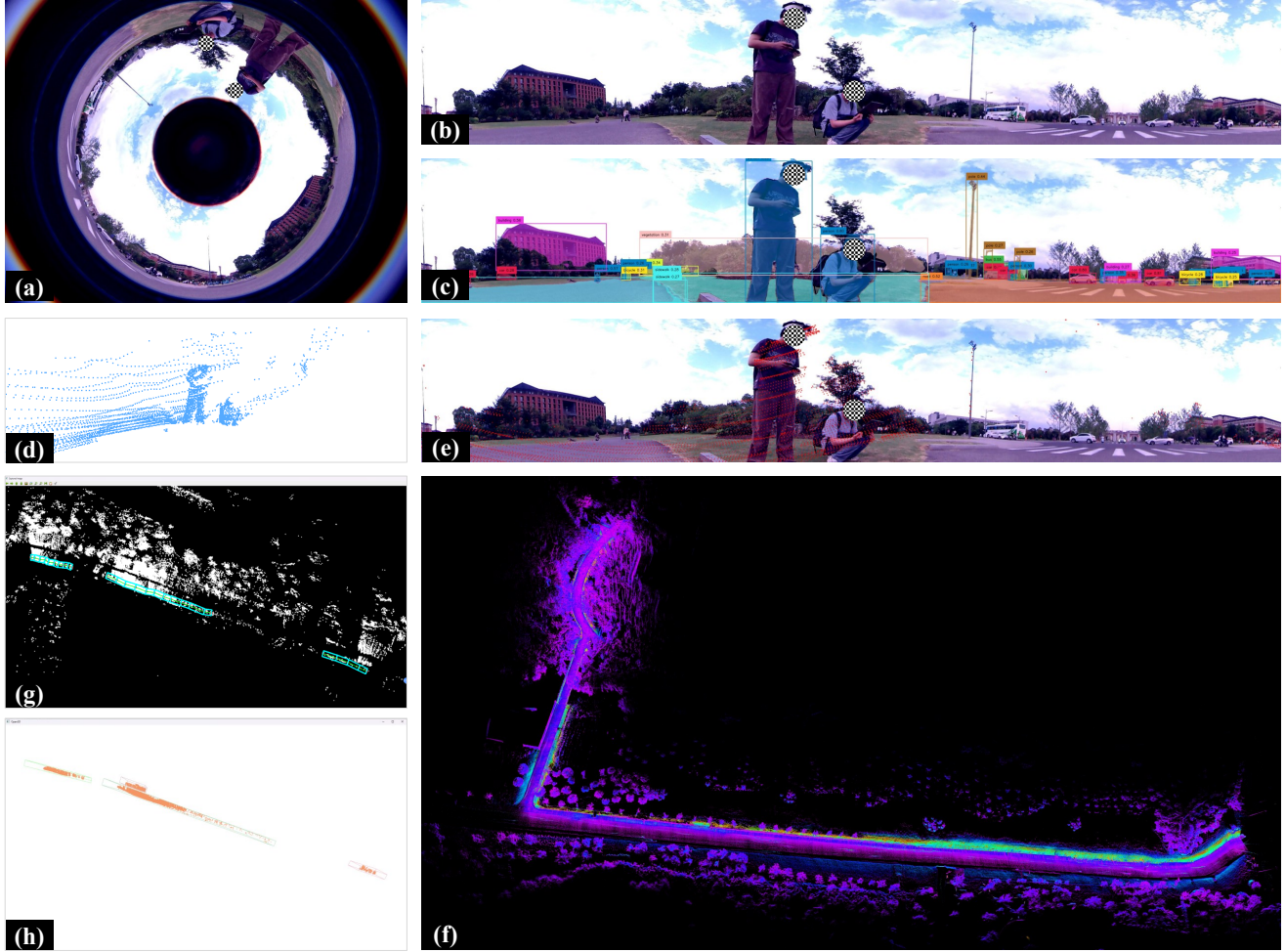


Figure 10. **QuadOcc ground-truth construction pipeline.** (a) Raw panoramic annulus captured by the PAL camera. (b) Equirectangular (ER) panorama obtained by *calibrated* OCam/Taylor [95] unwarping of (a). (c) Open-vocabulary segmentation on the ER image to obtain per-pixel class scores (e.g., Grounded-SAM [37]), yielding \mathcal{S}_t and score maps \mathbf{Q}_t . (d) A single time-synchronized LiDAR scan \mathbf{P}_t . (e) LiDAR \rightarrow camera projection followed by *image \rightarrow point* label transfer: pixels at $u = \pi(T_{L\rightarrow C}\tilde{\mathbf{p}}_L)$ assign $(\ell, w) = \mathbf{Q}_t(u)$ to 3D points, producing per-point semantics and confidence. (f) LiDAR SLAM [101] mapping for long-range geometry and temporal consistency. (g) Human-in-the-loop BEV annotation of moving-object trajectories to form tubes/boxes $\{\Gamma_k\}, \{B_{k,t}\}$ for dynamic/static separation. (h) Points are associated with trajectory boxes and motion attributes (direction, instance), then voxelized with majority voting and temporal aggregation to yield the refined semantic occupancy volume \mathbf{V}_{ref} . This pipeline produces $64 \times 64 \times 8$ semantic volumes at 0.4 m resolution under a 6-class taxonomy and is used as GT for training/evaluation on *QuadOcc*.

$Z_{\text{max}} = 1.2$ m, and a native cubic voxel size $\Delta = 0.4$ m, yielding a $64 \times 64 \times 8$ grid that balances (i) adequate radius for low-speed legged motion and foothold safety, (ii) memory/latency budgets for real-time inference on embedded GPUs, and (iii) azimuthal continuity for panoramic cues. We also standardize a six-class schema {vehicle, pedestrian, road, building, vegetation, terrain} to stabilize training under long-tailed class frequencies while keeping labels deployable for onboard planning. The corpus contains ten scenes and 24K frames captured under day/dusk/night (the latter also used in stress tests).

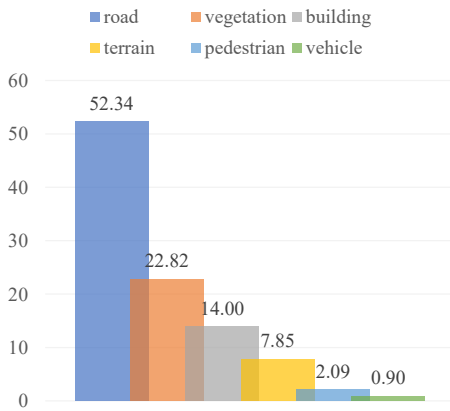
9.8. Quality Control and Semi-Automatic Labeling

Our labels originate from multi-frame LiDAR accumulation, Grounded-SAM initialization, and targeted manual fixes in ambiguous regions and around thin structures. During quality control, we flag voxels whose $\text{conf}(V_i)$ or temporal agreement rates fall below thresholds, and prioritize these for human proofreading.

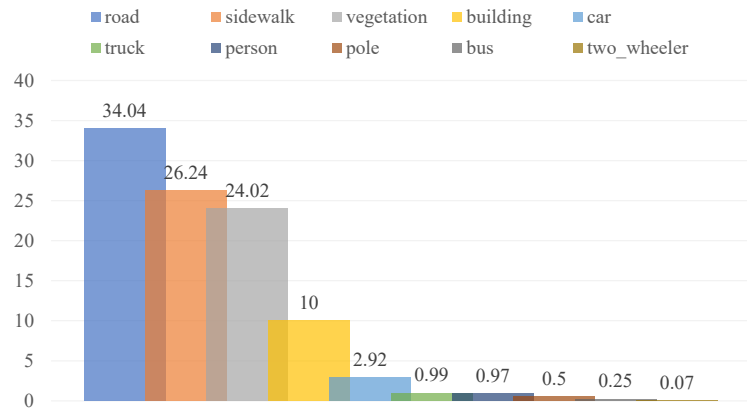
9.9. Analysis: Distribution, Difficulty, and Lighting

Class imbalance. On non-empty voxels, road dominates ($\approx 52.3\%$) followed by vegetation ($\approx 22.8\%$) and build-

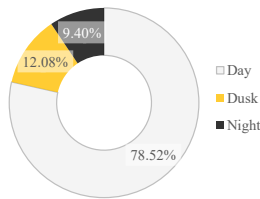
(a) QuadOcc: Semantic Frequency (%)



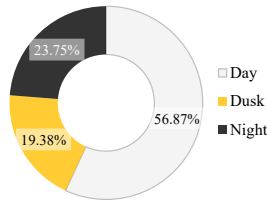
(b) Human360Occ (H3O): Semantic Frequency (%)



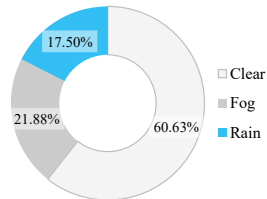
(c) QuadOcc: Time-of-Day Distribution (%)



(d) H3O: Time-of-Day Distribution (%)



(e) H3O: Weather Distribution (%)



(f) H3O: Weather × Time of Day (Voxels)

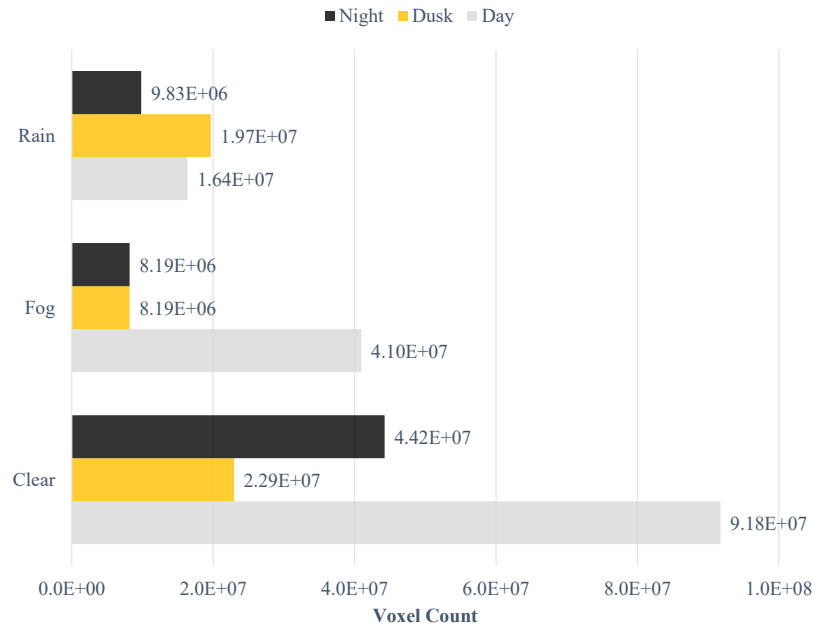


Figure 11. **Dataset statistics for QuadOcc and Human360Occ (H3O).** (a) QuadOcc semantic frequency (non-empty voxels): strong head classes (e.g., *road* $\approx 52.34\%$) with a long tail (*pedestrian*, *vehicle*). (b) H3O semantic frequency (non-empty voxels): most voxels lie in *road/sidewalk/vegetation/building*, with smaller shares for traffic-related rare classes. (c) QuadOcc time-of-day split by frames: Day 78.5%, Dusk 12.1%, Night 9.4%. (d) H3O time-of-day split by voxels: Day 56.9%, Dusk 19.4%, Night 23.8%. (e) H3O weather split by voxels: Clear 60.6%, Fog 21.9%, Rain 17.5%. (f) H3O weather \times time of day (voxels): **clear/day** 91.75M, **clear/night** 44.24M, **fog/day** 40.96M dominate. *Notes:* (a,b) use non-empty voxel frequencies; (c) is frame-level stats for QuadOcc; (d–f) are voxel-level stats for H3O.

ing ($\approx 14.0\%$), while vehicle/pedestrian are rare ($\approx 0.9\%/2.1\%$). This long-tail calls for per-class reweighting or sampling-aware training.

Dynamic vs. static. Dynamic tubes reduce motion ghosts and improve temporal coherence near moving objects; they also ease targeted manual verification.

Lighting. Day/dusk/night coverage intentionally stresses robustness. We observe that crepuscular lighting often improves geometric precision (reduced glare), whereas nighttime increases sparsity and aliasing in the far range, recommending stronger temporal priors or test-time refinement.

Confidence-driven curation. The per-voxel confidence and windowed agreement are reliable indicators for spot-

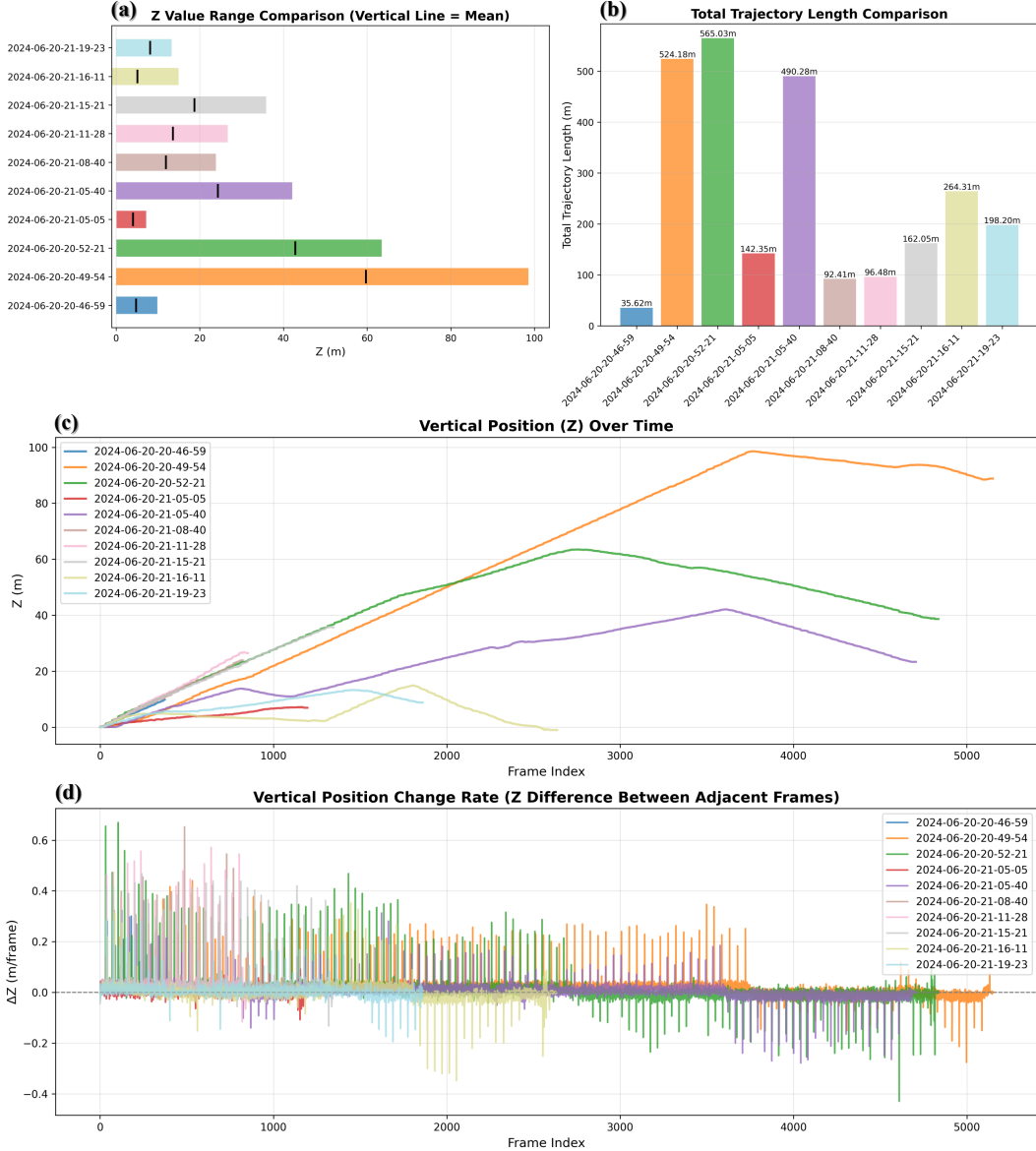


Figure 12. **QuadOcc camera pose statistics.** Visualization of the ego camera pose distribution on QuadOcc in the canonical grid frame (X forward, Y left, Z up). (a)–(d) show complementary views of the aggregated 6-DoF poses over all sequences: top-down ego trajectories, heading statistics, and height/orientation distributions. The coverage concentrates within the 12.8 m radius and $64 \times 64 \times 8$ voxel grid used for ground-truth construction, confirming that the chosen range and resolution (Sec. 4.7) are well-aligned with real quadruped operation and the gait-induced body motion that motivates our GDC and bi-grid design.

ting residual errors at class boundaries (*e.g.*, vehicle–road).

10. Human360Occ: Dataset Construction

Goal and setting Human360Occ (H3O) targets full-surround semantic occupancy for legged/humanoid platforms from a *single* panoramic stream. Each frame provides RGB, metric depth, and semantic panoramas, and the ground-truth (GT) occupancy at two resolutions ($64 \times 64 \times 8$

and $128 \times 128 \times 16$). We standardize within-/cross-city splits and record rich metadata for reproducibility.

10.1. Panoramic capture

Cubemap rig and stitching. We mount six synchronized virtual cameras in CARLA [102] (front/right/back/left/up/down) with unified exposure to avoid face-wise brightness drift. Images from the six faces are stitched into an

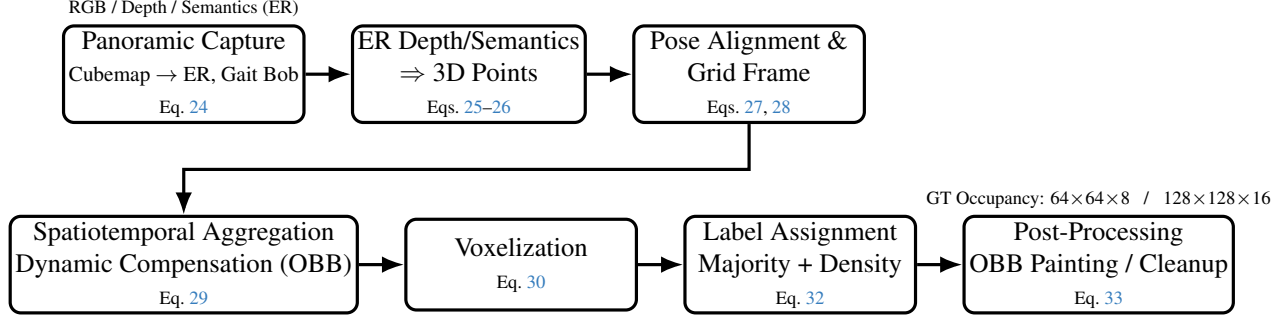


Figure 13. **H3O ground-truth construction pipeline.** Starting from synchronized cubemap panoramas, we stitch to an equirectangular (ER) image and emulate legged motion with a speed-conditioned vertical bob (Eq. 24). ER depth and semantics are back-projected to the camera frame by ER \rightarrow sphere \rightarrow 3D conversion (Eqs. 25–26). We then align points to a canonical grid frame (forward X , up Z , left Y via Y -flip) using a reference pose (Eqs. 27, 28). A spatiotemporal aggregation window stabilizes moving actors through OBB-based local registration and transport to the reference time τ (Eq. 29), mitigating ghost trails. The aligned points are voxelized within a fixed 3D range to indices (i, j, k) (Eq. 30) and labeled by majority with density safeguards (Eq. 32). Finally, we apply post-processing to ensure complete occupancy of dynamic instances (*OBB painting*) and clean small/noisy components (Eq. 33). Outputs include semantic occupancy at $64 \times 64 \times 8$ and $128 \times 128 \times 16$ over the same spatial bounds, together with per-sequence metadata for exact reproducibility.

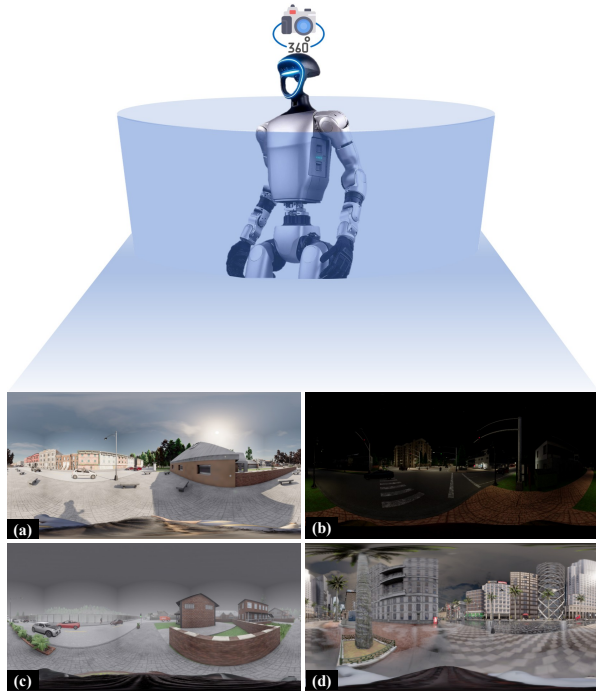


Figure 14. **H3O: Weather and lighting diversity.** Representative equirectangular (ER) panoramas illustrating the variety of conditions covered by *Human360Occ (H3O)*. (a) Clear—daytime; (b) Clear—night; (c) Fog; (d) Rain/overcast in a metropolitan scene. All frames are native ER inputs used directly for training/evaluation. Across H3O, voxel-level distributions span *Clear/Fog/Rain* and *Day/Dusk/Night*, enabling controlled stress-tests under illumination and adverse weather. Ground-truth supervision is provided at two resolutions ($64 \times 64 \times 8$ and $128 \times 128 \times 16$) over the same spatial bounds.

equirectangular panorama using a calibrated cubemap-to-ER pipeline.

Gait-induced motion (bob). To emulate first-person legged motion, the camera center undergoes a vertical bob whose amplitude and frequency adapt to walking speed. Let t be time (s), $v(t)$ the ego speed, $A(v)$ the amplitude (m), and $f(v)$ the frequency (Hz). The camera z position is:

$$z(t) = z_0 + A(v(t)) \cdot \sin(2\pi \cdot f(v(t)) \cdot t + \phi), \quad (24)$$

where $A(v)$ linearly interpolates within $[A_{\min}, A_{\max}]$ and $f(v)$ within $[f_{\min}, f_{\max}]$ as speed increases.

Environment randomization. We randomize the environment at the *sequence* level across maps, weather, and time-of-day with fixed quotas for coverage. Concretely, H3O spans **16** distinct CARLA maps (10 sequences per map) and totals **160** sequences (**8,000** frames). Weather is sampled from $\{\text{Clear}, \text{Fog}, \text{Rain}\}$, yielding the realized distribution: Clear 97 ($\approx 60.6\%$), Fog 35 ($\approx 21.9\%$), Rain 28 ($\approx 17.5\%$). Time-of-day is sampled from $\{\text{day}, \text{dusk}, \text{night}\}$, realized as: day 91 ($\approx 56.9\%$), dusk 31 ($\approx 19.4\%$), night 38 ($\approx 23.8\%$). For exact reproducibility, each sequence provides a `sequence_meta.json` that records the loaded map ID, time-of-day label, weather type and parameters, and simulation tick rate.

10.2. From panoramas to a registered 3D point cloud

Depth-to-3D in camera coordinates. Given an equirectangular depth map $r(u, v)$ (meters) of size $W \times H$ with pixel coordinates $(u, v) \in [0, W) \times [0, H)$, we first map pixels to spherical angles:

$$\theta(u) = \frac{2\pi}{W}u - \pi, \quad \phi(v) = \frac{\pi}{H}v, \quad (25)$$

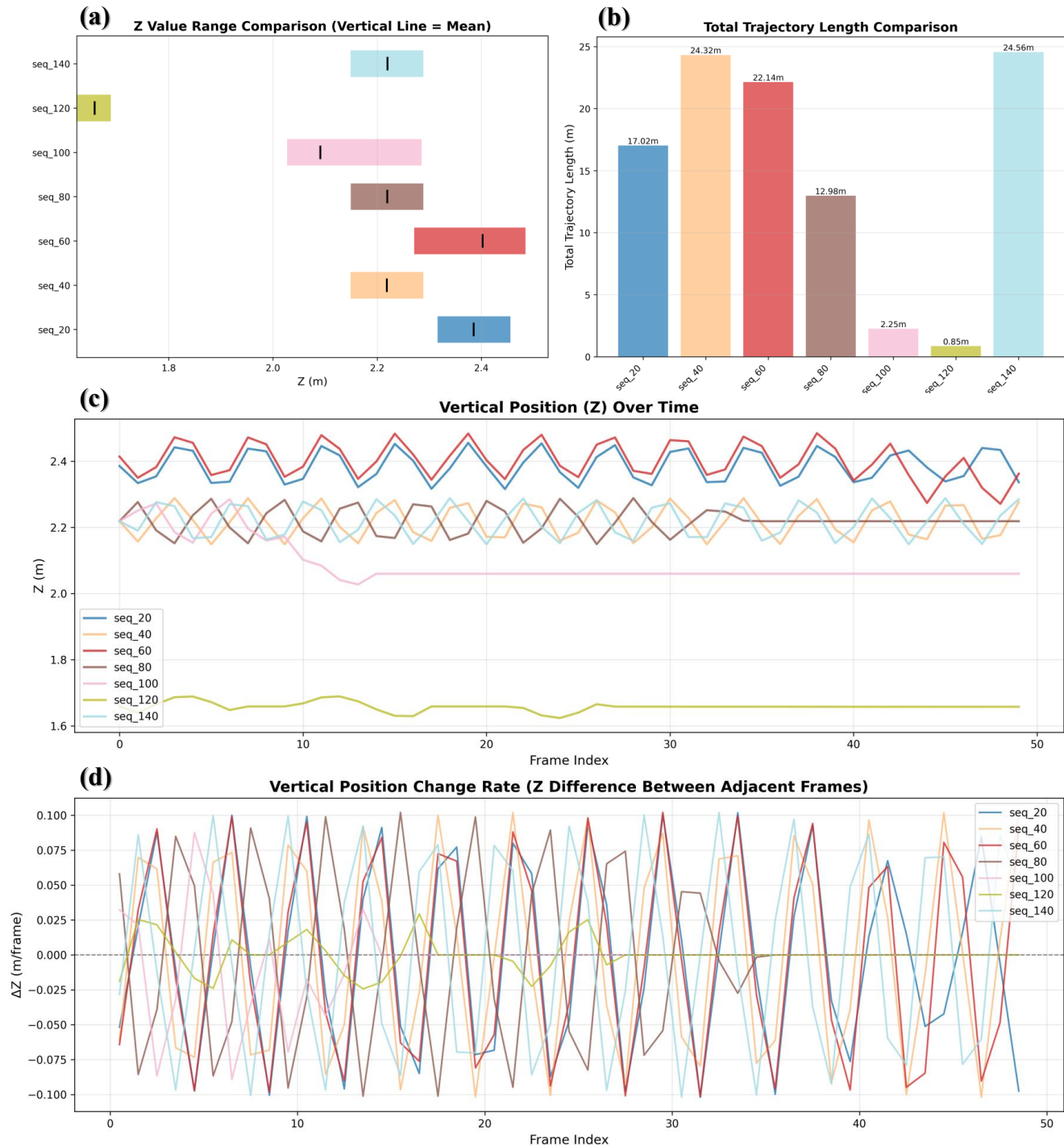


Figure 15. **Human360Occ (H3O) ego pose distribution.** Camera pose statistics for Human360Occ in the same grid frame as used for QuadOcc, aggregated over 160 sequences across 16 CARLA maps and diverse weather/lighting conditions. (a)–(d) provide complementary views of the ego trajectories and 6-DoF poses, including top-down coverage and orientation/height distributions. The plots highlight that H3O exhibits wide heading coverage, non-trivial vertical bobbing, and varied viewpoints, which together stress-test panoramic SSC under gait-like motion and support the standardized within-/cross-city splits and dual-resolution occupancy volumes used in our benchmarks.

and then project to the local camera frame (left-handed, X forward, Y right, Z up):

$$\mathbf{p}_c(u, v) = \begin{bmatrix} x \\ y \\ z \end{bmatrix} = r(u, v) \begin{bmatrix} \sin \phi \cos \theta \\ \sin \phi \sin \theta \\ \cos \phi \end{bmatrix}. \quad (26)$$

We discard invalid measurements (too near/far) and sky pixels and keep (\mathbf{p}_c, ℓ) pairs where ℓ is the Cityscapes-style [103] semantic ID.

Pose alignment and grid frame. Let $\mathbf{T}_{w \leftarrow c(t)} \in SE(3)$ be the camera pose at time t and define the grid frame so that X is forward, Z is up, and Y points *left* (a Y -flip w.r.t. the camera). If $\mathbf{F}_y = \text{diag}(1, -1, 1, 1)$, then the world-to-grid transform at a *reference* frame τ is

$$\mathbf{T}_{g \leftarrow w} = (\mathbf{T}_{w \leftarrow c(\tau)} \mathbf{F}_y)^{-1}. \quad (27)$$

A point captured at time t transforms to the grid frame as

$$\tilde{\mathbf{p}}_g = \mathbf{T}_{g \leftarrow w} \mathbf{T}_{w \leftarrow c(t)} \begin{bmatrix} \mathbf{p}_c \\ 1 \end{bmatrix}, \quad \mathbf{p}_g = \Pi(\tilde{\mathbf{p}}_g), \quad (28)$$

where Π drops the homogeneous coordinate. We aggregate a temporal window of frames around τ (Sec. 10.3).

10.3. Spatiotemporal aggregation with dynamic compensation

We stabilize moving actors (cars, walkers) to the reference time τ to mitigate “ghost tubes” in time-accumulated clouds.

OBB-based local registration. For every dynamic actor, we obtain an oriented bounding box (OBB) at time t via its rigid transform $\mathbf{T}_{\text{box}}^{(t)}$ and extents $\mathbf{e} = (e_x, e_y, e_z)$. A world point \mathbf{p}_w is inside a *scaled* OBB if

$$|(\mathbf{T}_{\text{box}}^{(t)})^{-1} [\mathbf{p}_w; 1]| \preceq \mathbf{e} \odot s + \mathbf{m}, \quad (29)$$

where $s > 1$ is a scale factor, \mathbf{m} is a per-axis margin (m), and \preceq is element-wise. For points inside, we transport them from time t to τ by composing actor poses; otherwise we keep the standard camera-pose alignment of (28). As a fall-back, we optionally *remove* dynamic points from non-reference frames or *paint* current-frame OBBs into the grid (Sec. 10.5).

10.4. Voxelization and semantic labeling

Grid bounds and resolution. We set an asymmetric vertical range anchored at the ego camera: $Z_{\min} = -2.0$ m ensures sufficient ground coverage and small depressions below the head-height camera, while $Z_{\max} = 1.2$ m captures overhanging obstacles without wasting vertical resolution. We therefore define a fixed 3D range

$$\mathcal{R} = [-X_{\max}, X_{\max}] \times [-Y_{\max}, Y_{\max}] \times [Z_{\min}, Z_{\max}],$$

with defaults $X_{\max} = Y_{\max} = 12.8$ m, $Z_{\min} = -2.0$ m, $Z_{\max} = 1.2$ m, and a native cubic voxel size $\Delta = 0.4$ m. The native grid size is $\mathbf{N} = (N_x, N_y, N_z) = \lfloor (\max - \min) / \Delta \rfloor$, and we also export higher resolutions (e.g., $128 \times 128 \times 16$) over the *same* \mathcal{R} .

Indexing. A grid index for a point $\mathbf{p}_g = (x, y, z)$ is

$$(i, j, k) = \left\lfloor \frac{x - x_{\min}}{\Delta} \right\rfloor, \left\lfloor \frac{y - y_{\min}}{\Delta} \right\rfloor, \left\lfloor \frac{z - z_{\min}}{\Delta} \right\rfloor. \quad (30)$$

Label assignment with density safeguards. Let $\mathcal{P}_{i,j,k}$ be the set of aggregated points falling into voxel (i, j, k) and $\ell(\cdot)$ their semantic IDs. We adopt majority voting with a minimum support:

$$\hat{c}_{i,j,k} = \arg \max_c \#\{\mathbf{p} \in \mathcal{P}_{i,j,k} : \ell(\mathbf{p}) = c\}, \quad (31)$$

keep if $\#\mathcal{P}_{i,j,k} \geq \tau$, $\tau = \max(N_{\min}, \lceil \rho_{\min} V_{\text{vox}} \rceil)$, (32)

where $\#S$ denotes the cardinality (number of elements) of a set S . N_{\min} is a point-count threshold, ρ_{\min} is an optional density floor (points/m³), and V_{vox} is the voxel volume. Unless stated otherwise, we use majority voting with $N_{\min} = 4$ and optionally enable the density floor.

10.5. Post-processing

OBB painting. To ensure complete occupancy for current-frame dynamic instances, we fill their OBBs in the grid using a scaled+margin ROI (s, \mathbf{m}):

for voxels $v \in \text{ROI}$:

$$\text{occ}[v] \leftarrow \begin{cases} c_{\text{actor}}, & \text{override,} \\ c_{\text{actor}} \text{ if } \text{occ}[v] = 0, & \text{keep.} \end{cases} \quad (33)$$

We analogously paint known static vehicles (*environment objects*) with a slightly tighter ROI.

Noise removal. We remove isolated singletons (no same-label neighbors) and delete small connected components below a voxel-count threshold using spatial-connectivity (we favor 6-connectivity to preserve thin structures).

Semantic schema and storage. Occupancy volumes are stored as `uint8` NumPy arrays of shape $[N_x, N_y, N_z]$, where 0 denotes empty and 1~28 follow a Cityscapes-style palette (e.g., road/sidewalk/building/vegetation/person/car/truck/bus/twowheeler, etc.). We export both native and $128 \times 128 \times 16$ grids, plus optional colored PCDs of voxel centers for visual auditing.

10.6. Train/val splits and stats

H3O comprises 160 sequences / 8K frames across 16 maps under diverse weather and lighting. Each frame includes RGB, metric depth, ER semantics, poses, and GT occupancy at two resolutions, supporting within-city (per-map 8:2) and cross-city (12/4 maps) protocols.

10.7. Default configuration

Unless specified otherwise, we use: time window $T = 50$ frames centered at τ ; native voxel size $\Delta = 0.4$ m over $\mathcal{R} = [\pm 12.8 \text{ m}]$ (XY) and $[-2.0, 1.2] \text{ m}$ (Z); label assignment majority with $N_{\min}=4$ (optionally density-gated); OBB fill for dynamic and static vehicles enabled; and singleton/small-component removal.

Deliverables. For each sequence, we provide ER panoramas (RGB/Depth/Semantics), per-frame `ground_truth.json` (poses, actor OBBs, ego info), `sequence_meta.json`, native and $128 \times 128 \times 16$ occupancy volumes, and optional point-cloud visualizations for quality control.

11. Implementation Details of Baselines

General protocol. All camera-only baselines are *re-trained from scratch* on our panoramic legged-robot benchmarks with *minimal modifications*: we preserve original backbones/heads and only adapt dataset hooks, projection reshaping, voxel grid sizes, and loss toggles required by the panoramic small-volume regime. Unless otherwise noted, we fix seeds, follow original training schedules, and report results with the default settings stated under each method.

11.1. Overview

We organize per-method details in a uniform structure to facilitate verification and extension:

- **[Method Name]:** a short protocol summary (minimal changes, training schedule).
- **QuadOcc:** dataset- and grid-specific settings for re-training on our QuadOcc split.
- **H3O:** corresponding settings for retraining on H3O.
- **Design rationale:** why these choices are necessary under panoramic, small-volume settings.

11.2. MonoScene

Scope. We keep MONOSCENE’s [50] original design and adapt only the dataset branch, projection reshape, and losses required by panoramic inputs and smaller grids; all models are trained from scratch.

QuadOcc. Data and taxonomy. QuadOcc provides per-frame panoramic RGB and voxelized semantic occupancy within the 3D range $X=Y=\pm 12.8$ m, $Z \in [-2.0, 1.2]$ m, discretized into a $64 \times 64 \times 8$ grid at 0.4 m resolution. We train on 7 labels with empty at index 0 and six non-empty classes: {vehicle, pedestrian, road, building, vegetation, terrain}. Images are equirectangular panoramas of size 370×1220 produced by calibrated OCam/Taylor [95] unwarping of a PAL camera. We use the official train/val sequences and sample every 5 frames.

Architecture adaptations. We adopt the small-grid CP and standard lifting without extra magnification:

- **Context Prior (CP) for small grids:** the CP module (CPMegaVoxels) dynamically adjusts kernel sizes/strides as a function of the minimum side-length; if any side is < 3 , it falls back to 1^3 kernels with unit stride to avoid over-downsampling.

- **Logit-GT alignment:** the decoder head ensures output logits match the $64 \times 64 \times 8$ GT grid exactly after lifting.

- **FLoSP lifting (QuadOcc):** we use the *standard* FLoSP reshape consistent with the chosen `project_scale`.

Training hyper-parameters. We mostly keep the KITTI [26] recipe and only adapt what is necessary:

- **Scene/voxel:** `full_scene_size= (64, 64, 8)`, voxel size 0.4 m, origin $[-12.8, -12.8, -1.2]$.
- **Backbone/decoder:** feature dimension 64.
- **Classes/losses:** `n_classes=7` (including empty); enable `CE_loss`, `sem_scal_loss`, `geo_scal_loss`, and `fp_loss` with `frustum_size= 8`; disable relation loss (`relation_loss=false`) due to small grids and panoramic distortions.
- **Optimization:** AdamW [104] with $LR= 10^{-4}$, $WD= 10^{-4}$; MultiStepLR (milestones= [20], $\gamma = 0.1$); `max_epochs= 30`, `batch_size= 1`, `n_gpu= 1`.
- **Data loading:** `num_workers_per_gpu= 16`.
- **Augmentation:** color jitter (0.4, 0.4, 0.4) at train-time; no augmentation at val/test.

Camera and normalization. We use OCam/Taylor [95] intrinsics and the precomputed annulus→equirectangular maps. RGB normalization: $\mu = [\frac{123.971}{255}, \frac{123.564}{255}, \frac{164.785}{255}]$, $\sigma = [\frac{84.271}{255}, \frac{88.170}{255}, \frac{72.966}{255}]$.

Loss weighting. We compute frequency-based class weights on the QuadOcc training split (non-empty voxels) for the CE term to stabilize rare dynamic categories and the head class (road).

Design rationale. (i) *Small-grid & dynamic CP:* with $64 \times 64 \times 8$, aggressively strided 3^3 stacks can collapse features; dynamic kernels retain receptive fields without over-downsampling. (iii) *Disable relation loss:* co-occurrence priors that help on KITTI [26] tend to over-smooth azimuthal seams and suppress rare classes under panoramas. (iv) *jitter on:* moderate color jitter improves robustness.

H3O. Projection (FLoSP). We use the *standard* FLoSP reshape consistent with `project_scale= 1`.

Voxel grid and scene bounds. Two modes are supported: *native* $64 \times 64 \times 8$ at 0.4 m/voxel (default) and *fixed 128* $128 \times 128 \times 16$ at 0.2 m/voxel; both share $25.6 \times 25.6 \times 3.2$ m with origin $[-12.8, -12.8, -2.4]$ m.

Remapping and losses. We adopt the default 11-class remap (car/truck/bus separated; traffic furniture merged). We enable `CE_loss`, `sem_scal_loss`, `geo_scal_loss`, `fp_loss` (`frustum_size= 8`), and disable relation loss.

Image pipeline and optimization. Panoramas are resized to 352×1216 and normalized with statistics ($\mu=[0.485, 0.456, 0.406]$, $\sigma=[0.229, 0.224, 0.225]$). We follow the KITTI [26] schedule (AdamW [104], $LR=$

Table 16. **QuadOcc vs. KITTI [26] (MonoScene [50]).**

Component	KITTI [26]	QuadOcc	Rationale
Grid size	256×256×32	64×64×8	Embedded compute / near-field focus
Voxel size	0.2 m	0.4 m	Balanced radius vs. memory
Classes	20	6	legged-relevant labels
Relation loss	true	false	Unstable / unhelpful on small grids
3D decoder	KITTI default	small-grid CP preserved	Prevent over-downsampling

Table 17. **H3O vs. KITTI [26] (MonoScene [50]).**

Component	KITTI [26]	H3O	Rationale
Grid size	256×256×32	64×64×8 / 128×128×16	Near-field focus vs. detail
Voxel size	0.2 m	0.4/0.2 m	Match grid mode and memory
Projection scale	2	1 (standard reshape)	Lifting without over-enlargement
Classes	20	11	Stable yet granular labels
Relation loss	true	false	Avoid over-smoothing rare classes
Batch size	1	2	Smaller grid ⇒ higher throughput

10^{-4} , $WD=10^{-4}$; MultiStepLR at epoch 20 with $\gamma=0.1$; 30 epochs). The smaller grid permits `batch_size=2` and `num_workers_per_gpu=12` on a single GPU.

Design rationale. (i) *Equirect + standard reshape*: no extra magnification is required for uniform azimuthal sampling; this reduces aliasing. (ii) *Two grid modes*: *native* trades speed for scale; *fixed128* recovers thin structures. (iii) *Relation loss off*: improves stability under panoramic distortions and class imbalance.

11.3. SGN

Scope. We keep SGN’s [96] transformer-based image-to-voxel lifting and the original detector-head layout, and make only minimal changes required by panoramic inputs and small voxel grids. All models are trained from scratch. Single-GPU batches ≥ 1 are fully supported by us in both training and testing.

QuadOcc. Data and taxonomy. QuadOcc provides single-frame omnidirectional RGB and voxelized semantic occupancy within $X=Y=\pm 12.8$ m and $Z \in [-2.0, 1.2]$ m, discretized at 0.4 m into a $64 \times 64 \times 8$ grid. We use 7 labels with empty at index 0 and six non-empty classes: {vehicle, pedestrian, road, building, vegetation, terrain}. Images are equirectangular panoramas of size 370×1220 obtained via calibrated OCam/Taylor [95] unwarping.

Architecture adaptations (transformer lifting).

- *3D queries.* We instantiate one 3D query per voxel center within the native bounds; each query carries a 3D sinusoidal positional encoding.
- *2D tokens for panoramas.* ER images are encoded by

a 2D CNN and flattened into tokens with 2D positional encodings augmented by spherical (longitude/latitude) terms computed from OCam/Taylor [95] intrinsics.

- *Cross-attention lifting.* Multi-head cross-attention lets 3D queries sample informative 2D tokens to produce fused voxel features; The decoder head maps fused features to per-voxel logits aligned with the $64 \times 64 \times 8$ GT grid.

Losses, schedules, and IO. We enable `CE_ssc_loss`, `sem_scal_loss`, and `geo_scal_loss`. Optimization uses AdamW [104] ($LR = 2 \times 10^{-4}$, $WD = 10^{-2}$) with CosineAnnealing and a linear warmup of 500 iterations; `total_epochs=48`, `batch_size=1`, `workers_per_gpu=4`. RGB normalization uses dataset statistics $\mu = [\frac{123.971}{255}, \frac{123.564}{255}, \frac{164.785}{255}]$, $\sigma = [\frac{84.271}{255}, \frac{88.170}{255}, \frac{72.966}{255}]$.

H3O. Grid modes. We support voxel grid mode with the spatial bounds $25.6 \times 25.6 \times 3.2$ m and origin $[-12.8, -12.8, -2.4]$ m: *native* ($64 \times 64 \times 8$ at 0.4 m/voxel; default). The transformer lifting is unchanged: 3D queries at voxel centers cross-attend to ER image tokens.

Remap, losses, and schedule. We adopt the default 11-class remap (*car/truck/bus* separated; *traffic furniture* merged), and enable the same `CE/sem_scal/geo_scal` losses. Panoramas are resized to 608×1216 and normalized with statistics ($\mu=[0.485, 0.456, 0.406]$, $\sigma=[0.229, 0.224, 0.225]$). We follow a KITTI-style schedule [26]: AdamW ($LR = 10^{-4}$, $WD = 10^{-4}$), MultiStepLR at epoch 20 with $\gamma = 0.1$, for 30 epochs; `batch_size=2`, `num_workers_per_gpu=12`.

Table 18. KITTI [26] vs. QuadOcc (SGN [96]).

Component	KITTI [26] baseline	QuadOcc (ours)	Rationale
Grid size (GT)	256×256×32	64×64×8	Near-field grid for embedded budget
Voxel size	0.2 m	0.4 m	Trade detail for memory/speed
Bounds (x/y/z)	[0, -25.6, -2, 51.2, 25.6, 4.4]	[-12.8, -12.8, -1.2, 12.8, 12.8, 2.0]	Symmetric, small-volume scenes
2D input	Pinhole RGB	ER panorama 370×1220	Panoramic coverage
2D tokens/PE	Planar PE	ER tokens + spherical (lon/lat) terms	Longitude/latitude-aware tokenization
Lifting	X-attn: 3D←2D	Same (X-attn)	Transformer lifting unchanged
3D queries	Per voxel (dense)	Per voxel (dense)	Same mechanism; fewer voxels
Classes	20	7 (empty+6)	Dataset taxonomy
Losses	CE/sem_scal/geo_scal	Same	Stable on small grids

Table 19. KITTI [26] vs. H3O (SGN [96]).

Component	KITTI [26] baseline	H3O (ours)	Rationale
Grid size (GT)	256×256×32	64×64×8 (<i>native</i>)	Matched to human-scale scenes
Voxel size	0.2 m	0.4 m	Memory/speed under panorama
Bounds (x/y/z)	[0, -25.6, -2, 51.2, 25.6, 4.4]	[-12.8, -12.8, -2.4, 12.8, 12.8, 0.8]	Symmetric bounds
2D input	Pinhole RGB	ER panorama 608×1216	Wider FoV under H3O
2D tokens/PE	Planar PE	ER tokens + spherical (lon/lat) terms	Azimuth/elevation-aware tokens
Lifting	X-attn: 3D←2D	Same (X-attn)	Transformer lifting unchanged
3D queries	Per voxel (dense)	Per voxel (dense)	Same mechanism; fewer voxels
Classes	20	11 (default remap)	default mapping on H3O
Losses	CE/sem_scal/geo_scal	Same	Consistent objectives
Batching	$B=1$ common	$B=2$ (single GPU)	Smaller grid ⇒ higher throughput

11.4. VoxFormer

Scope. We follow VOXFORMER [51]’s two-stage design and keep the model (VOXFORMER-S) with minimal adaptations for panoramic inputs and small voxel grids. We reimplement the head/encoder hooks to support batch ≥ 1 and retrain all models from scratch.

QuadOcc. Data and taxonomy. QuadOcc provides single-frame omnidirectional RGB and voxelized semantic occupancy within $X=Y=\pm 12.8$ m and $Z \in [-2.0, 1.2]$ m, discretized at 0.4 m into a $64\times 64\times 8$ grid. We train with 7 labels (index 0 is empty; non-empty: {vehicle, person, road, building, vegetation, terrain}). Images are equirectangular panoramas of size 370×1220 produced by calibrated OCam/Taylor [95] un-warping of a PAL camera.

Architecture adaptations.

- *Head.* We replace the baseline head with VoxFormerHeadQuad (class count 20 \rightarrow 7; frequency-based class weights). BEV positional encoding (PE): We extensively explored two granularities that are compatible with the repository’s square-PE constraint: (a) 64×64 PE for a compact $32\times 32\times 4$ BEV query grid (our default for fair comparisons); and (b) 512×512 PE for $128\times 128\times 16$ queries (the largest setting we tested). Despite the substantially larger query sets in (b)—which increase memory and latency considerably—we observed no material accuracy gains on QuadOcc/H3O. In

particular, (b) frequently leads to out-of-memory on a 24 GB RTX 4090 even at batch size 1 under panoramic inputs; enabling activation checkpointing/mixed precision improves stability but more than $10\times$ wall-clock time with negligible accuracy change. Given the fairness to other transformer-based baselines (e.g., SGN [96]) and the unfavorable compute–benefit trade-off, we report the 64×64 PE results and regard (b) as ablations without qualitative advantage.

- *Encoder/Layers.* We adapt reference-point generation to QuadOcc bounds and voxel sizes; cross/self attention settings follow the small model.
- *Proposals.* Instead of reading proposals from `img metas`, we dynamically voxelize 3D points to obtain sparse 3D proposals (Sec. Stage-1 below), enabling both pseudo-LiDAR and GT-LiDAR routes.

Stage-1 (depth⇒3D proposals). We use two interchangeable routes to generate 3D points for proposal voxelization:

- *Pseudo-LiDAR.* We run MONODEPTH2 [105] on ER panoramas and back-project with OCam/Taylor [95] intrinsics to obtain per-pixel 3D points, then voxelize them into a coarse $64\times 64\times 8$ prior.
- *GT-LiDAR.* We alternatively voxelize the provided LiDAR points to form the same coarse prior.

Both routes train the identical Stage-1 network (query update via multi-head deformable cross-attention from 3D queries to ER image features). In all cases, Stage-1 outputs $64\times 64\times 8$ logits.

Stage-2 (refinement). Stage-2 takes Stage-1 logits as priors and refines them with a shallow stack of query updates and

3D convolutions, keeping the same class set and bounds. Unless specified, reported results include the *GT-LiDAR Stage-1* variant followed by Stage-2.

Training hyper-parameters. We keep the VoxFormer-S recipe and adapt only what is necessary:

- *Scene/voxel.* `full_scene_size=(64, 64, 8)`, voxel size 0.4 m, origin $[-12.8, -12.8, -1.2]$, eval range 25.6 m.
- *Transformer (S).* `embed_dims= 128`, `cross/self layers= 3/2`, `sampled points per head= 8`, `FFN= 1024`.
- *Optimization.* AdamW (LR = 2×10^{-4} , WD = 10^{-2}), CosineAnnealing with 500 warmup iters, `total_epochs= 20`, `batch_size= 4`, `workers_per_gpu= 4`, gradient clip (max_norm= 35).
- *Losses.* We enable `CE_ssc_loss`, `sem_scal_loss`, and `geo_scal_loss`.

Image pipeline and normalization. Panoramas are 370×1220 ; standard color jitter (0.4, 0.4, 0.4) at train-time; no val/test augmentation. RGB normalization uses QuadOcc statistics $\mu = [\frac{123.971}{255}, \frac{123.564}{255}, \frac{164.785}{255}]$, $\sigma = [\frac{84.271}{255}, \frac{88.170}{255}, \frac{72.966}{255}]$.

Class weighting. We compute frequency-based weights on the QuadOcc training split (non-empty voxels) for the CE term to stabilize rare dynamic classes and the head class (road).

Design rationale. (i) *BEV positional encoding.* We made a best-effort push to larger PE (up to 512×512) to increase the number of BEV queries and potential receptive-field coverage. However, under omnidirectional inputs and small near-field grids, the resulting memory/latency costs are disproportionately high and do not translate into consistent accuracy gains; thus we favor the 64×64 PE for fair and efficient comparison. (ii) *Proposal voxelization (pseudo vs. GT).* Pseudo-LiDAR from MONODEPTH2 [105] preserves the monocular setting but introduces depth noise that weakens sparse-query coverage; training Stage-1 with GT-LiDAR proposals improves stability yet still does not close the gap to stronger transformer baselines [96] on QuadOcc/H3O. (iii) *Minimal deltas from the baseline.* We keep transformer depths/widths unchanged and only modify class hooks, reference-point generation, and proposal construction; this avoids capacity confounds and keeps results reproducible under panoramic small-volume scenes.

H3O. Data and taxonomy. H3O provides single-frame omnidirectional RGB and voxelized semantic occupancy within $X=Y=\pm 12.8$ m and $Z \in [-2.4, 0.8]$ m, discretized at 0.4 m into a native $64 \times 64 \times 8$ grid. We adopt the default 11-class remap with empty at index 0 and ten non-empty classes: {road, sidewalk, building, vegetation, car, truck, bus, two-wheeler, person, pole}.

Panoramas are equirectangular (ER).

Architecture adaptations (omni variants).

- *Head.* We use `VoxFormerHeadOmni` (class count $20 \rightarrow 11$; frequency-based class weights).
- *Encoder/Layers.* We operate with ER cameras and *consume precomputed* per-voxel, per-view image correspondences from `img metas: projected_pix` stores the pixel coordinates (u, v) of voxel centers on each ER image, and `fov_mask` flags whether a voxel lies inside the valid field-of-view. These caches: (i) avoid recomputation of spherical projection in the forward pass, (ii) faithfully adapt to the equirectangular model, and (iii) naturally extend to multi-camera ER inputs by concatenating per-view tokens and masks. Reference-point generation is adapted to the symmetric bounds $[-12.8, 12.8]^2 \times [-2.4, 0.8]$.
- *BEV positional encoding (PE) \rightarrow query grid.* The repository enforces a square PE whose side equals the BEV query side. Given H3O’s native $64 \times 64 \times 8$ GT, we evaluate two compatible query configurations: (a) 64×64 PE $\Rightarrow 32 \times 32 \times 4$ queries (default for fairness/efficiency), and (b) 512×512 PE $\Rightarrow 128 \times 128 \times 16$ queries (largest tested; ablation).

Stage-1 (depth \Rightarrow 3D proposals). We consider two proposal routes within the H3O bounds:

- *Pseudo-depth (ER).* Back-project ER depth from MONODEPTH2 [105] and voxelize the 3D points.
- *Ground-truth depth (ER).* To rule out reproduction artifacts, we also voxelize proposals from *ground-truth* depth maps and train VOXFORMER-S [51] accordingly; we *report* its accuracy alongside the pseudo-depth variant.

Stage-1 performs multi-head deformable cross-attention from 3D queries to ER image features and outputs $64 \times 64 \times 8$ logits.

Stage-2 (refinement). Stage-2 refines Stage-1 logits using a shallow stack of query updates and 3D convolutions under the same bounds/classes. Unless otherwise specified, H3O results correspond to Stage-1 \rightarrow Stage-2.

Training hyper-parameters.

- *Scene/voxel.* `full_scene_size=(64, 64, 8)`, voxel size 0.4 m, origin $[-12.8, -12.8, -2.4]$, eval range 25.6 m.
- *Transformer (S).* `embed_dims= 128`, `cross/self layers= 3/2`, `sampled points per head= 8`, `FFN= 1024`.
- *Optimization.* AdamW (LR = 2×10^{-4} , WD = 10^{-2}), CosineAnnealing with 500 warmup iters, `total_epochs= 24`, `batch_size= 1`, `workers_per_gpu= 4`, gradient clip (max_norm= 35).
- *Losses.* `CE_ssc_loss`, `sem_scal_loss`, `geo_scal_loss` are enabled.

Table 20. KITTI [26] vs. QuadOcc (VoxFormer-S [51]).

Component	KITTI baseline	QuadOcc (ours)	Rationale
Grid size (GT)	256×256×32	64×64×8	Embedded compute / near-field focus
Voxel size	0.2m	0.4m	Balanced radius vs. memory
BEV PE → queries	128×128×16	32×32×4 (default); 128×128×16 (ablations)	Larger PE yields heavy memory/latency with no material gains
Classes	20	7	Panoramic, legged-relevant labels
Proposal source	meta/file	voxelized (pseudo/GT) Depth	Rule out reproduction artifacts
Batch size	1	4	Smaller grid ⇒ higher throughput

Image pipeline and normalization. Panoramas are resized to 608×1216; we use statistics for normalization ($\mu=[0.485, 0.456, 0.406]$, $\sigma=[0.229, 0.224, 0.225]$). No test-time augmentation is used.

Design rationale. (i) *Cached ER correspondences.* Pre-computing `projected_pix` and `fov_mask` yields deterministic cross-attention sampling, eliminates redundant spherical projection during the forward pass, and scales to multi-camera ER inputs—this is the key omni feature we introduce to strengthen VoxFormer [51] on H3O. (ii) *BEV PE under square-constraint.* We pushed the BEV PE to 512×512 (i.e., 128×128×16 queries) to maximize coverage; however, the substantial memory/latency increase did not translate into consistent accuracy gains on H3O, mirroring our QuadOcc findings. (iii) *Depth-driven proposals (pseudo and GT).* Using *ground-truth* depth removes the confound from depth estimation noise and confirms that the performance gap is *not* due to reproduction artifacts: even with GT-depth proposals and Stage-2 refinement, VOXFORMER-S [51] remains markedly weaker than stronger transformer baselines (e.g., OccFormer [52], SGN [96]) in our panoramic setting.

11.5. OccFormer

Scope. We follow OCCFORMER [52] and preserve the original architecture (2D backbone + LSS-style view transformer [106] + 3D encoder/decoder + Mask2Former-style head [107] with a DETR decoder [108]). To adapt to panoramic inputs and small voxel grids in QuadOcc, we only modify the dataset branch, spatial bounds, class taxonomy, and sampling/normalization. All models are trained from scratch; the core network depths/widths remain unchanged.

QuadOcc. Data and taxonomy. QuadOcc provides single-frame omnidirectional RGB and voxelized semantic occupancy within $X=Y=\pm 12.8$ m and $Z \in [-1.2, 2.0]$ m, discretized at 0.4m into a 64×64×8 grid. We train on 7 labels (index 0 is unlabeled; non-empty classes: {vehicle, person, road, building, vegetation, terrain}). Images are unfolded equirectangular panoramas; Input resolution is (384, 1280); We use dataset-specific normalization (mean [123.971, 123.564, 164.785],

std [84.271, 88.170, 72.966]).

Architecture/data adaptations.

- *Camera/input.* We switch `camera_used` from ['left'] (KITTI [26]) to ['images_unfold'] to consume unfolded panoramic RGB.
- *View transformer bounds.* We set `point_cloud_range=[-12.8, -12.8, -1.2, 12.8, 12.8, 2.0]` and `occ_size=[64, 64, 8]` (voxel size 0.4m). This symmetrizes the near-field volume relative to KITTI’s [26] 51.2×51.2×6.4m.
- *Classes.* We replace the 20-class SemanticKITTI taxonomy with the 7-class QuadOcc taxonomy in the head and evaluator.

Model components (unchanged). We keep the KITTI [26] baseline components: `CustomEfficientNet-B7` backbone, `SECONDFPN` `image` neck, `ViewTransformerLiftSplatShootVoxel` for `image→voxel` lifting, `OccupancyEncoder` (3D), `MSDeformAttnPixelDecoder3D` BEV neck, `Mask2FormerOccHead`, and a 9-layer `DetrTransformerDecoder`.

Training hyper-parameters.

- *Optimization.* AdamW with LR = 10^{-4} , weight decay = 10^{-2} ; gradient clipping with `max_norm=20`.
- *Schedule.* StepLR with milestones at epochs [20, 25]; total 30 epochs.
- *Batching.* `samples_per_gpu=4` (vs. 1 on KITTI [26]) and `workers_per_gpu=8`, enabled by the smaller grid.
- *Losses.* Loss weights follow the baseline: `loss_cls=2.0`, `loss_mask=5.0`, `loss_dice=5.0`. We keep class weighting consistent with the 7-class setup (background down-weighted).

I/O and evaluation. Input resolution is (384, 1280); we evaluate on the official QuadOcc validation split (KITTI [26] baseline uses `test`). Unless noted, we report single-model, single-scale results without test-time augmentation.

Design rationale. (i) *Symmetric near-field bounds.* QuadOcc emphasizes a 25.6×25.6×3.2m volume; centering and halving KITTI’s [26] bounds removes pinhole-

Table 21. KITTI [26] vs. H3O (VoxFormer-S [51]).

Component	KITTI baseline	H3O (ours)	Rationale
Grid size (GT)	256×256×32	64×64×8	Native near-field
Voxel size	0.2m	0.4	Match grid mode and memory
BEV PE → queries	128×128×16	32×32×4 (default); 128×128×16 (ablation)	Square-PE constraint; larger PE = heavy cost
Omni projection	pinhole	ER	Deterministic sampling
Proposals	meta/file	voxelized (pseudo/GT)	Rule out reproduction artifacts

Table 22. KITTI [26] vs. QuadOcc (OccFormer [52]).

Component	KITTI [26] baseline	QuadOcc (ours)	Rationale
Grid size (GT)	256×256×32	64×64×8	Near-field focus; compute budget
Voxel size	0.2m	0.4m	Match smaller radius, reduce tokens
Point-cloud range	[0, -25.6, -2, 51.2, 25.6, 4.4]	[-12.8, -12.8, -1.2, 12.8, 12.8, 2.0]	Symmetric bounds for panoramas
Classes	20	7	Quad taxonomy (coarser labels)
Camera	left (pinhole)	images.unfold (panorama)	Fit ER/unfolded panoramas
Batch size	1	4	Lower res ⇒ higher throughput

centric bias and avoids wasting tokens outside the useful radius. (ii) *Dataset-specific normalization*. Quad statistics align the unfolded ER appearance with the backbone’s expectations and improve stability. (iii) *Minimal deltas*. We keep the architecture intact (EffNet-B7 [109] → Mask2FormerOccHead [107]) to avoid capacity confounds; changes are isolated to data, bounds, taxonomy, and sampling so that comparisons remain fair and reproducible.

H3O. Data and taxonomy. H3O provides omnidirectional RGB and voxelized semantic occupancy within $X=Y=\pm 12.8$ m and $Z \in [-2.4, 0.8]$ m, discretized at 0.4 m into a native 64×64×8 grid. We adopt the 11-class remap with empty at index 0 and non-empty: {road, sidewalk, building, vegetation, car, truck, bus, two_wheeler, person, pole}. Images are panoramic ER (equidistant cylindrical) frames; normalization uses H3O statistics (mean [123.971, 123.564, 164.785], std [84.271, 88.170, 72.966]).

Architecture/data adaptations.

- *Camera/input*. camera_used is switched from ['left'] (KITTI [26]) to ['panorama.rgb'] (ER panorama).
- *View transformer*. We replace the pinhole version with ViewTransformerLiftSplatShootVoxelH3O and its ER-aware geometry routine get_geometry_h3o, which maps pixel (u, v) to azimuth–elevation (θ, ϕ) (e.g., $\theta = 2\pi(u/W - 0.5)$, $\phi = \pi(v/H)$) and then to 3D rays before lifting and splatting.
- *Spatial bounds and resolution*. point_cloud_range = [-12.8, -12.8, -2.4, 12.8, 12.8, 0.8], occ_size = [64, 64, 8] (voxel size 0.4 m). Symmetric near-field bounds replace KITTI’s [26] forward-biased setup.

- *Pipelines*. Training uses CreateDepthFromLiDAR (dataset='h3o') to provide LSS [106] depth supervision and LoadH3OAnnotation; evaluation uses LoadH3OAnnotation.

Components (kept as baseline). CustomEfficientNet-B7 backbone, SECONDFPN image neck, OccupancyEncoder (3D), MSDeformAttnPixelDecoder3D BEV neck, Mask2FormerOccHead, and a 9-layer DetrTransformerDecoder.

Training hyper-parameters.

- *Optimization*. AdamW (LR = 10^{-4} , weight decay = 10^{-2}); gradient clipping with max_norm = 20.
- *Schedule*. StepLR with milestones at epochs [20, 25]; total 30 epochs.
- *Batching and sampling*. samples_per_gpu = 4, workers_per_gpu = 8.

I/O and evaluation. Input resolution is (640, 1280); we evaluate on the official val split of H3O and select save_best='h3o_SSC_mIoU'. We report single-model, single-scale results without test-time augmentation.

Design rationale. (i) *ER-aware lifting*. The equidistant cylindrical model avoids systematic azimuthal bias and preserves uniform horizontal sampling; get_geometry_h3o converts (u, v) to (θ, ϕ) and then to 3D rays for accurate lift–splat. (ii) *Symmetric bounds at small radius*. Centered 25.6×25.6×3.2 m is better matched to 360° human-scale scenes than KITTI’s [26] forward-biased frustum. (iii) *Minimal deltas*. By keeping backbone, necks, encoder, and head identical to the baseline, improvements (or failures) can be attributed to geometry/data adaptations rather than capacity changes.

Table 23. KITTI [26] vs. H3O (OccFormer [52]).

Component	KITTI [26] baseline	H3O (ours)	Rationale
Grid size (GT)	256×256×32	64×64×8	Small near-field; computation budget
Voxel size	0.2 m	0.4 m	Match smaller radius; reduce tokens
Point-cloud range	[0, -25.6, -2, 51.2, 25.6, 4.4]	[-12.8, -12.8, -2.4, 12.8, 12.8, 0.8]	Symmetric bounds for 360° panoramas
Camera model	pinhole (left)	ER panorama	Correct geometry for 360° input
View transformer	LSS-voxel (pinhole)	LSS-voxel (ER)	Azimuth/elevation → 3D rays
cam_channels	33	27	Match H3O camera metadata
Batch size	1	4	Lower res ⇒ higher throughput

11.6. LMSCNet

Scope. We follow LMSCNET [38]’s original 3D CNN design and keep the architecture intact (multi-scale encoder–decoder for semantic scene completion). To adapt to panoramic inputs and the native small voxel grid in QuadOcc, we only modify channel widths and the loss, and plug in the Quad dataset/config. All models are trained from scratch with identical depths and kernels as the baseline.

QuadOcc. Data and taxonomy. QuadOcc provides single-frame semantic occupancy within $X=Y=\pm 12.8$ m and $Z \in [-2.0, 1.2]$ m, discretized at 0.4 m into a native $64\times 64\times 8$ grid (*implementation layout*: $(W, H, D)=(64, 8, 64)$). We train on 7 labels (index 0 is empty; non-empty: {vehicle, person, road, building, vegetation, terrain}).

LiDAR input and alignment. Unlike monocular settings, our LMSCNET [38] input is the *real*, time-synchronized Livox Mid360 scan captured together with the PAL panoramic camera. Each scan is transformed to the benchmark frame using the calibrated rigid extrinsics $T_{\text{cam}\leftarrow\text{lidar}} \in SE(3)$: $\mathbf{X}_{\text{cam}} = T_{\text{cam}\leftarrow\text{lidar}}\mathbf{X}_{\text{lidar}}$. We then *crop* to the QuadOcc volume $X=Y=\pm 12.8$ m, $Z \in [-2.0, 1.2]$ m and *voxelize* at 0.4 m to produce a native $64\times 64\times 8$ occupancy tensor. The origin and axes match the ground-truth convention (origin $[-12.8, -12.8, -1.2]$ m), so that voxel indices align *exactly* with the GT occupancy region. Out-of-bounds points are discarded; extrinsics are applied consistently across all scans in a sequence. This setup eliminates projection drift, ensures geometric consistency with the PAL camera, and provides a strong LiDAR-aligned prior for semantic scene completion.

Architecture adaptations.

- *Channel expansion (core).* Let C_{in} denote the input feature channels at the encoder entrance. We expand the base width to $f=8C_{\text{in}}$ (baseline uses $f=C_{\text{in}}$). The first encoder block is updated to $\text{Conv2d}(C_{\text{in}} \rightarrow f) \rightarrow \text{ReLU} \rightarrow \text{Conv2d}(f \rightarrow f) \rightarrow \text{ReLU}$. At the decoder end, the fusion layer `conv1_1` maps the concatenated multi-scale features back to C_{in} instead of f to keep the output head unchanged. (We tried $2\times$ widening; it underperformed, hence the $8\times$ choice.)
- *Loss.* We use `CrossEntropyLoss` for the 1:1 scale.

- *Logit alignment.* The decoder produces logits that are voxel-for-voxel aligned with the native $64\times 64\times 8$ GT grid (our tensors follow (W, H, D) with $H=8$).

Training hyper-parameters. Unless otherwise stated, we keep the official recipe and change only what is necessary for QuadOcc:

- *Dataset/config.* `QuadSSC`, `grid` $(W, H, D) = (64, 8, 64)$, `num_classes=7`, `FLIPS=true`.
- *Optimization.* Adam [110] (LR = 10^{-3} , $\beta=(0.9, 0.999)$), no weight decay; power-iteration LR schedule per epoch with `LR_POWER=0.98`.
- *Batching.* `train_bs=8`, `val_bs=8`, `num_workers=8`.
- *Schedule.* `epochs=80`.

Design rationale. (i) *Width-for-depth trade-off.* QuadOcc collapses the vertical axis to $H=8$ bins; naive downscaling severely reduces 3D capacity. Widening the base to $8\times$ restores representational power without changing depth or kernel shapes. (ii) *Input-aware widening.* Starting from $C_{\text{in}} \rightarrow f$ lets the network capture richer low-level cues that are otherwise lost on the shallow vertical dimension, while mapping back to C_{in} preserves the original head. (iii) *Minimal deltas, consistent I/O.* We keep depths/kernels unchanged, align logits exactly to the native grid, and modify only widths, thus ensuring fairness and reproducibility.

11.7. SSCNet

Scope. We follow SSCNET [24]’s fully 3D CNN design (encoder–decoder with multi-scale skip connections) and keep depths, kernel sizes, and heads unchanged. To fit QuadOcc’s panoramic near-field grid, we minimally modify the upsampling head and the loss/balancing, and we plug in the Quad dataset branch. All models are trained from scratch.

QuadOcc. Data and taxonomy. QuadOcc provides single-frame voxelized semantic occupancy within $X=Y=\pm 12.8$ m and $Z \in [-2.0, 1.2]$ m, discretized at 0.4 m into a native $64\times 64\times 8$ grid (*implementation layout*: $(W, H, D) = (64, 8, 64)$). We adopt the Quad taxonomy with `num_classes=7` for occupied voxels; *free* voxels are encoded as label 255 and *ignored* by the CE loss (thus not counted as a learnable class).

Table 24. KITTI [26] baseline vs. QuadOcc (LMSCNet [38]).

Component	KITTI [26] baseline	QuadOcc (ours)	Rationale
Grid size (GT)	$256 \times 256 \times 32$	$64 \times 64 \times 8$	Small near-field grid
Voxel size	0.2 m	0.4 m	Memory/compute budget
Base width f	C_{in}	$8 C_{in}$	Recover capacity lost by small $H=8$
Enc. first conv	$f \rightarrow f$	$C_{in} \rightarrow f$	Widen from the input stage
Dec. last conv	$\cdot \rightarrow f$	$\cdot \rightarrow C_{in}$	Keep head I/O unchanged
Batch size	2–4	8	Smaller grid \Rightarrow higher throughput
Epochs	60–80	80	Converge under widened channels

LiDAR input and alignment. Our SSCNET [24] and SSCNET-FULL [38] variant consumes the *real*, time-synchronized Livox Mid360 scan acquired together with the PAL panoramic camera. Each scan is rigidly transformed to the benchmark/camera frame using calibrated extrinsics $T_{\text{cam} \leftarrow \text{lidar}} \in SE(3)$: $\mathbf{X}_{\text{cam}} = T_{\text{cam} \leftarrow \text{lidar}} \mathbf{X}_{\text{lidar}}$. We then *crop* to the QuadOcc volume $X=Y=\pm 12.8$ m, $Z \in [-2.0, 1.2]$ m and *voxelize* at 0.4 m to form a native $64 \times 64 \times 8$ occupancy tensor (implementation layout $(W, H, D) = (64, 8, 64)$). The origin and axes follow the ground-truth convention (origin $[-12.8, -12.8, -1.2]$ m), so that voxel indices align *exactly* with the GT occupancy region. Out-of-bounds points are discarded, and the same extrinsics are applied consistently across a sequence. The resulting single-channel free/occupied grid serves as the network input, while the CE loss supervises the 7 semantic classes with free voxels ignored (`label=255`). This setup removes projection drift, enforces geometric consistency with the PAL rig, and provides a strong LiDAR-aligned prior for semantic scene completion.

Architecture adaptations.

- *Deconvolution head* \rightarrow *Upsample + Conv (stability fix)*. The baseline uses a transposed convolution to recover the native grid (`ConvTranspose3d(128→C, k=4, s=4)`). We replace it with `Upsample(scale_factor=4, mode='nearest')` followed by `Conv3d(128→C, k=3, s=1, p=1)`. This avoids loss-time shape/NaN issues while preserving the target stride and receptive field.
- *Logit alignment*. The decoder outputs voxel-aligned logits at the native $64 \times 64 \times 8$ resolution (our tensors follow (W, H, D) with $H=8$).

Training hyper-parameters.

- *Scene/grid*. $(W, H, D) = (64, 8, 64)$, voxel size 0.4 m, `num_classes=7`, `free=255` (ignored).
- *Optimization*. Adam [110] (LR = 10^{-3} , $\beta = (0.9, 0.999)$), no weight decay; constant LR schedule.
- *Batching*. `train_bs=8`, `val_bs=8`, `num_workers=8`.
- *Schedule*. `epochs=80`.

Design rationale. (i) *Numerically stable upsampling*. Replacing deconvolution with Upsample + Conv preserves the $\times 4$ stride yet eliminates checkerboard artifacts and loss-time instability observed with transposed convolutions on small $H=8$ grids. (ii) *Minimal deltas, aligned outputs*. Keeping the encoder/decoder unchanged and aligning logits exactly to the native grid ensures that performance differences come from data/label semantics and small-grid geometry rather than capacity shifts.

11.8. OccRWKV

Scope. We follow the original OCCRWKV [46] pipeline (point-cloud preprocessing \rightarrow BEV UNet branch \rightarrow 3D completion branch, with RWKV-style recurrent blocks) and keep depths/kernels unchanged. To fit panoramic near-field grids in QuadOcc, we introduce Quad-specific modules, LiDAR-driven inputs, explicit voxel coordinate ordering, and a simplified loss. All models are trained from scratch.

QuadOcc. Data and taxonomy. QuadOcc provides single-frame voxelized semantic occupancy within the near-field bounds $X \in [0, 25.6]$ m, $Y \in [-12.8, 12.8]$ m, $Z \in [-1.2, 2.0]$ m, discretized at 0.4 m into a native $64 \times 64 \times 8$ grid. We adopt 7 semantic classes (non-empty) and treat free space as 255 (ignored by CE).

LiDAR input and alignment. Our OCCRWKV [46] variant consumes the *real*, time-synchronized Livox Mid360 scan captured together with the PAL panoramic camera. Each scan is rigidly transformed to the benchmark/camera frame via calibrated extrinsics $T_{\text{cam} \leftarrow \text{lidar}} \in SE(3)$: $\mathbf{X}_{\text{cam}} = T_{\text{cam} \leftarrow \text{lidar}} \mathbf{X}_{\text{lidar}}$. We *crop* to the QuadOcc volume, *voxelize* at 0.4 m to obtain the native $64 \times 64 \times 8$ occupancy tensor, and align the origin/axes to the GT convention. Out-of-bounds points are discarded, and the same extrinsics are applied consistently per sequence.

Architecture/data adaptations.

- *LiDAR-driven inputs*. The network ingests point clouds from `PCD['1.1']` and dense occupancy from `3D_OCCUPANCY`; labels are read from `3D_LABEL['1.1']`.

Table 25. KITTI [26] baseline vs. QuadOcc (SSCNet-full [24]).

Component	KITTI [26] baseline	QuadOcc (ours)	Rationale
Grid size (GT)	256×256×32	64×64×8 (impl. (64, 8, 64))	Small near-field volume
Voxel size	0.2 m	0.4 m	Memory/compute budget
Upsampling head	ConvTranspose3d (×4)	Upsample ×4 + Conv3d	Avoid NaNs/shape issues; same stride
Labels (free)	0 (free), occupied > 0	255 (free), occupied < 255	Match Quad label semantics
Batch size	4	8	Lower res ⇒ higher throughput
Epochs	60–80	80	Convergence at native width/depth

Table 26. KITTI [26] baseline vs. QuadOcc (OccRWKV [46]).

Component	KITTI [26] baseline	QuadOcc (ours)	Rationale
Grid size	256×256×32	64×64×8	Near-field, low-memory grid
Voxel size	0.2 m	0.4 m	Token reduction for panoramic scenes
Bounds (X/Y/Z)	[0, 51.2]/−25.6:25.6/−2:4.4	[0, 25.6]/−12.8:12.8/−1.2:2.0	Match Quad near-field convention
Loss	CE + aux. seg	CE (w/ class weights) + Lovasz	Stable single-head supervision
Batch size	2	2	Compute budget
Epochs	80	80	Same convergence horizon

- *Occupancy + BEV fusion.* We treat the $D=8$ occupancy slices as channels ($B \times D \times H \times W$) and concatenate them with BEV features ($B \times C_{\text{bev}} \times H \times W$) along the channel dimension, yielding a $B \times (D + C_{\text{bev}}) \times H \times W$ tensor for the 2D BEV UNet.
- *Loss.* We remove auxiliary semantic-point loss and keep a *single* voxel-wise objective: class-weighted cross-entropy (CE) with `ignore_index=255` plus Lovasz-Softmax. Final logits are permuted to (B, C, W, D, H) as required by the head before loss.

Training hyper-parameters.

- *Dataset/config.* QuadOcc; grid $[W, H, D] = [64, 64, 8]$; voxel size 0.4 m; bounds as above; `FLIPS=true`; modalities: PCD, 3D_OCCUPANCY, 3D_LABEL.
- *Optimization.* Adam [110] (LR = 10^{-3} , $\beta = (0.9, 0.999)$), no weight decay; power-iteration schedule per epoch with `LR_POWER=0.98`.
- *Batching/schedule.* `batch_size=2`, `num_workers=8`, `epochs=80`.

Design rationale. (i) *Simplified loss.* Dropping the auxiliary semantic segmentation loss branch focuses capacity and stabilizes training; adding Lovasz complements CE on class-imbalanced voxels. (v) *Minimal deltas.* Network depths/widths are unchanged; improvements (or failures) can thus be attributed to geometry/data choices rather than capacity changes.

12. Discussions

12.1. Limitations and Potential Solutions

Spatial resolution and fine-grained interaction. Our semantic occupancy is defined on a $64 \times 64 \times 8$ grid with 0.4 m voxels around the ego, which is sufficient for navigation,

foothold selection, and path planning on legged/humanoid platforms with moderate speed and limited payload compared to intelligent vehicles. However, this resolution is not ideal for tasks that require fine-grained contact reasoning, such as precise grasping, object re-arrangement, or manipulation in cluttered shelves. At this scale, small objects and thin structures are often represented by only a few voxels, which amplifies label noise and makes it difficult to capture geometry with sub-voxel accuracy.

A straightforward remedy is to increase the grid resolution (e.g., $128 \times 128 \times 16$ under the same metric bounds), but our resolution study shows that this leads to a significant increase in memory and latency, and can even hurt mIoU due to optimization difficulty. Instead, a more promising direction is *hierarchical* or *adaptive* occupancy. One option is to maintain a coarse global grid (as in OneOcc) for full-surround situational awareness, while allocating high-resolution local volumes around the end-effectors (hands and feet) or task-relevant regions selected by an attention or proposal mechanism. Another option is to decouple geometry and semantics: a coarse semantic grid can be refined locally by an implicit or Gaussian-based representation [111] that super-resolves surfaces where higher accuracy is required. Both strategies preserve the efficiency and robustness of the current pipeline while opening the door to fine-grained interaction.

Dataset coverage and sim-to-real gap. QuadOcc is moderate-scale and rooted in a campus-like environment, and Human360Occ (H3O) is purely simulated. While this pairing is useful for studying cross-domain robustness and robot morphology changes, it does not fully cover the diversity of real humanoid deployment scenarios (e.g., dense indoor offices, homes, or highly dynamic crowds). In partic-

ular, our humanoid-style evaluation currently relies on simulated occupancy labels and thus inherits the biases of the simulator and rendering stack. This introduces an inevitable sim-to-real gap for humanoid robots with panoramas.

Mitigating this gap will require a combination of larger-scale real-world 360° occupancy datasets (*e.g.*, panoramic rigs mounted on humanoids or human operators) and sim-to-real adaptation techniques. Possible options include domain randomization and style augmentation in the panoramic image space, occupancy-level adversarial training between simulated and real volumes, and semi-supervised self-training where the model bootstraps dense occupancy from sparse or partial real sensors. Another complementary direction is to leverage weak labels, such as traversability or contact affordances, as auxiliary supervision for regions where dense voxel labels are missing.

Single-frame design and motion modeling. Our current formulation predicts occupancy from a single panoramic frame. This design choice avoids hard assumptions on the robot’s motion model, simplifies deployment, and is already robust to gait-induced jitter via GDC. However, it also limits the ability to accumulate evidence over time, to explicitly reason about dynamic objects, and to exploit long-term temporal context. In particular, fast-moving agents (pedestrians, vehicles, other robots) are treated as static at each frame, and any temporal consistency emerges only implicitly from the training data.

A natural extension is to move from single-frame inputs to short panoramic clips, and to lift them into a 4D spatio-temporal occupancy volume. Architecturally, this could be realized by adding a recurrent [112] or transformer-style temporal module on top of OneOcc, or by introducing causal 3D/4D convolutions over occupancy sequences. To keep the embodied footprint manageable, one promising strategy is to maintain a low-rate, wide-range occupancy memory complemented by higher-rate local updates near the robot, rather than processing dense video at full resolution.

12.2. Failure Case Analysis

Figure 16 illustrates a representative failure case from the challenging H3O-Heter split, where the robot traverses a corridor that is almost entirely covered by vegetation and spans multiple maps under the cross-city configuration. This scene is further compounded by adverse conditions: it is captured at dusk, in rain, with low illumination and strong specular highlights on wet surfaces. While our training data already covers diverse weather and lighting conditions, sequences that are simultaneously *vegetation-dominated*, *cross-map*, and *rainy at dusk* are extremely rare, and most trajectories follow road- or sidewalk-centric layouts in clearer visibility. As a result, all methods face a

substantial distribution shift in both geometry and appearance.

In this example, the ground-truth occupancy assigns the majority of near-field voxels to *vegetation* (class 4, green), and virtually no large dynamic objects such as *car* (class 5), *truck* (class 6), or *bus* (class 7). In contrast, vision-based baselines (*e.g.*, MonoScene [50], SGN-S [96]) hallucinate extensive road and sidewalk regions in front of the agent and along the sides. These errors reflect a strong reliance on co-occurrence priors learned from more typical urban scenes: given a forward-looking corridor with lane-like edges and headlight-like highlights, the models default to “road + sidewalk” even when the geometry and appearance actually correspond to wet vegetation. OneOcc substantially reduces these artifacts: the free/occupied structure is better aligned with the ground truth, and most spurious roads are removed, yet it still misclassifies sizable vegetation regions as sidewalk, leading to severe semantic errors despite reasonably accurate geometry.

This failure pattern highlights two important insights. First, even with improved architectural bias and stronger cross-city robustness, semantic occupancy prediction remains fundamentally data-driven: models inherit biases from the training distribution and struggle when encountering rare combinations of layout, weather, and time-of-day. Closing this gap will likely require larger-scale and more diverse 360° occupancy datasets that explicitly target under-represented environments (*e.g.*, forests, parks, off-road trails) under diverse conditions (night, adverse weather, seasonal changes), as well as more balanced class statistics. Second, the dominant error here is *semantic* rather than geometric: the model correctly infers that space is occupied, but assigns the wrong category. This suggests that future *open-vocabulary occupancy* [113] formulations, where volumetric geometry is coupled with flexible semantic embeddings instead of a fixed closed set of labels, could be beneficial. By leveraging open-set vision-language representations, such models may better adapt their semantic partition of the occupancy volume to novel environments (for example, distinguishing different types of vegetation or terrain) while reusing the same geometric backbone as OneOcc. Combined with stronger data diversity, such open-vocabulary occupancy could mitigate, though likely not completely eliminate, the kind of semantic failure observed in this case.

12.3. Range-wise Safety Analysis

To further examine whether the gains of OneOcc are confined to a particular depth interval or remain valid in safety-critical local regions, we report distance-binned mIoU comparisons against MonoScene [50] on both QuadOcc and H3O-Heter. Following the same evaluation protocol as the main paper, we restrict non-empty voxels to three nested

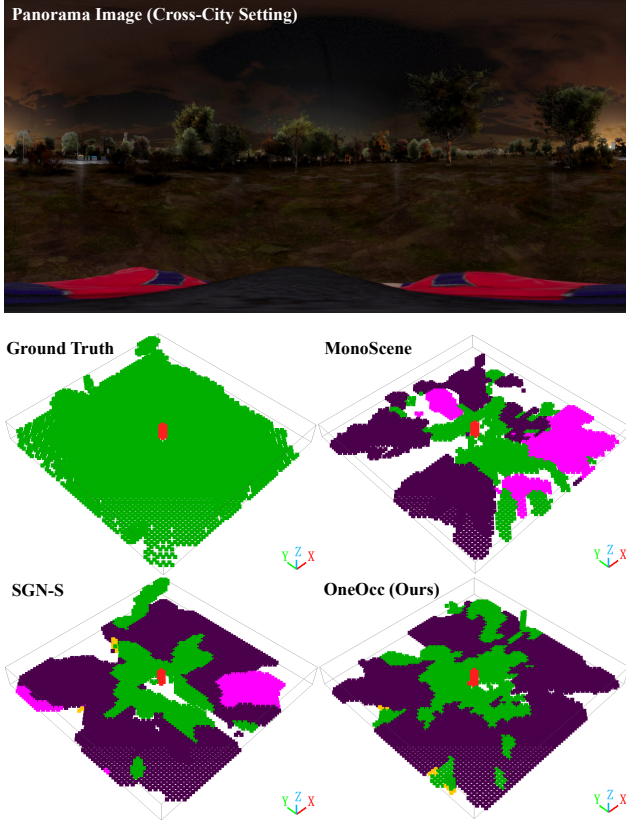


Figure 16. **Failure case on H3O-Heter (cross-city) in a rainy dusk scene dominated by vegetation.** From left to right: ground-truth occupancy, predictions from MonoScene [50], SGN-S [96], and OneOcc (Ours). OneOcc alleviates but does not eliminate severe semantic misclassification (vegetation predicted as sidewalk) under this rare combination of layout, weather, and time-of-day.

spatial ranges centered at the agent: *Far* ($\pm 12.8\text{m}$), *Mid* ($\pm 6.4\text{m}$), and *Near* ($\pm 3.2\text{m}$).

Figure 18 shows that OneOcc consistently outperforms MonoScene across all distance bins on both benchmarks. On QuadOcc, the mIoU improves from 19.19 to 20.56 in the Far range, from 23.32 to 24.47 in the Mid range, and from 24.29 to 24.95 in the Near range. On H3O-Heter, the corresponding gains are larger: 24.15 \rightarrow 32.23 (Far), 30.17 \rightarrow 37.11 (Mid), and 30.69 \rightarrow 37.35 (Near). These results indicate that the benefits of OneOcc are not limited to a specific distance regime, but remain stable from long-range completion to local occupancy reasoning. From a robotics perspective, the Near range is especially important because it is most directly related to short-horizon collision avoidance, foothold selection, and local traversability. Importantly, OneOcc still maintains positive margins in this region on both datasets: +0.66 mIoU on QuadOcc and +6.66 mIoU on H3O-Heter. This suggests that the proposed design does not merely improve far-field continuity or sup-

press panoramic artifacts at a global scale, but also provides more reliable local semantic occupancy in the region most relevant to embodied safety. A second trend is that both methods generally improve from Far to Near. This is expected, since smaller spatial ranges contain less severe long-range ambiguity, fewer occlusion-induced completion errors, and denser effective evidence around the agent. However, the gap between OneOcc and MonoScene remains consistently positive throughout. This supports the claim that the gains of OneOcc arise from better geometry-aware lifting and panoramic representation, rather than from overfitting to a narrow subset of voxels or to only far-range context. Overall, the distance-binned analysis complements the main benchmark tables by showing that OneOcc improves semantic occupancy prediction not only globally, but also in the near-field regime that is most critical for safe embodied deployment.

12.4. Scaling to Other Scenarios and Modalities

From legged to diverse robot morphologies. Although QuadOcc and H3O are designed for quadruped and humanoid-like settings, the core architectural ideas in OneOcc — dual-projection fusion, bi-grid voxelization, and lightweight 3D decoding — are not specific to a particular robot morphology. For wheeled platforms with forward-biased sensing, the same framework can be used with asymmetric voxel bounds that allocate more range in the forward direction while preserving 360° continuity, or with cropped panoramas when only 180° coverage is available. For aerial robots or platforms with elevated cameras, the vertical bounds of the voxel grid can be expanded to better capture tall structures and multi-level environments.

Indoor, outdoor, and extreme conditions. Our datasets focus on outdoor campus-style and urban-like scenes. Deployments in cluttered indoor environments introduce different statistics: shorter ranges, denser occlusions, and more small-scale objects. Scaling OneOcc to such scenarios mainly requires reconfiguring the voxel bounds and semantics, and retraining on appropriate indoor 360° data. Meanwhile, operation under extreme conditions (severe rain/snow, low light, lens contamination) may benefit from explicit robustness techniques such as test-time adaptation [63], uncertainty-aware occupancy heads, or sensor health monitoring that can gracefully degrade occupancy outputs when the panoramic signal is unreliable.

Multi-modal extensions. OneOcc is intentionally vision-only, which is attractive for platforms with strict payload and power budgets. Nevertheless, in settings where additional sensors are available, the proposed architecture can serve as a backbone for multi-modal occupancy. LiDAR or depth maps can be encoded into 2D or 3D features and fused

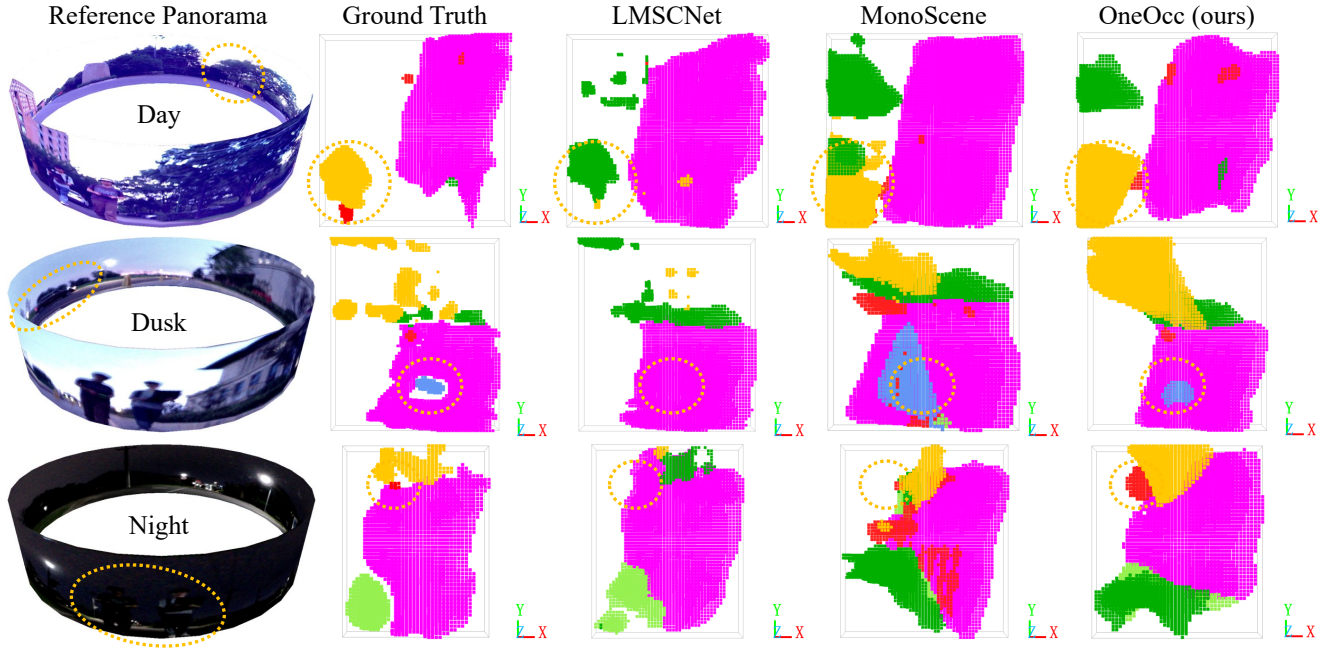


Figure 17. **Qualitative comparison on QuadOcc under different times of day.** From left to right: reference panorama, ground-truth occupancy, LMSCNet [38], MonoScene [50], and OneOcc (ours). From top to bottom: day, dusk, and night. All methods gradually degrade from day to dusk and further to night, where low illumination and glare introduce severe ambiguities. Compared to baselines, OneOcc reduces perspective sampling artifacts and yields more coherent occupied structures and semantics, especially for dynamic classes such as vehicles and pedestrians.

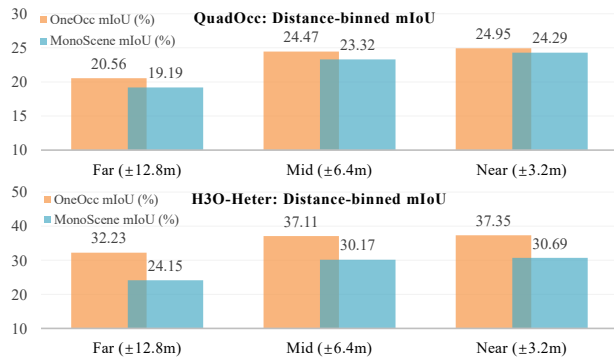


Figure 18. Distance-binned mIoU comparisons on QuadOcc and H3O-Heter. We evaluate non-empty voxels within three nested spatial ranges centered at the agent: Far ($\pm 12.8\text{m}$), Mid ($\pm 6.4\text{m}$), and Near ($\pm 3.2\text{m}$). OneOcc consistently outperforms MonoScene [50] across all ranges on both benchmarks, including the near-field region that is most relevant to local navigation and foothold safety.

with the panoramic features before or after bi-grid voxelization, while radar and event cameras [33] can complement the panoramic input with long-range or high-dynamic-range motion cues. A promising direction is to treat each modality as an additional “view” in the View2View sampling scheme, letting the model learn how to combine them into a unified

3D grid without hard-coded fusion rules.

12.5. Societal Impacts

Dense 3D semantic occupancy opens up positive applications for legged and humanoid robots. More reliable 360° perception can improve safety when robots operate in proximity to humans, reduce collisions with obstacles in cluttered environments, and enable new capabilities in search-and-rescue, inspection, and assistive robotics. In such contexts, a geometry-aware volumetric representation is often more interpretable and task-aligned than raw images, and can form a safer intermediate layer for downstream planning or language-conditioned policies.

At the same time, always-on full-surround perception could raise some societal questions. A robot equipped with a panoramic camera and a strong occupancy predictor could be used for pervasive surveillance or long-term monitoring of public or semi-private spaces. While our representation focuses on occupancy and coarse semantics rather than identity, it still encodes where humans and vehicles are likely to be, and could be combined with other modules to infer more sensitive attributes. Moreover, our datasets are biased toward specific geographies, weather patterns, and human behaviors, which may lead to failure modes or unfair performance in underrepresented environments. Responsible deployment will require transparency about sensing

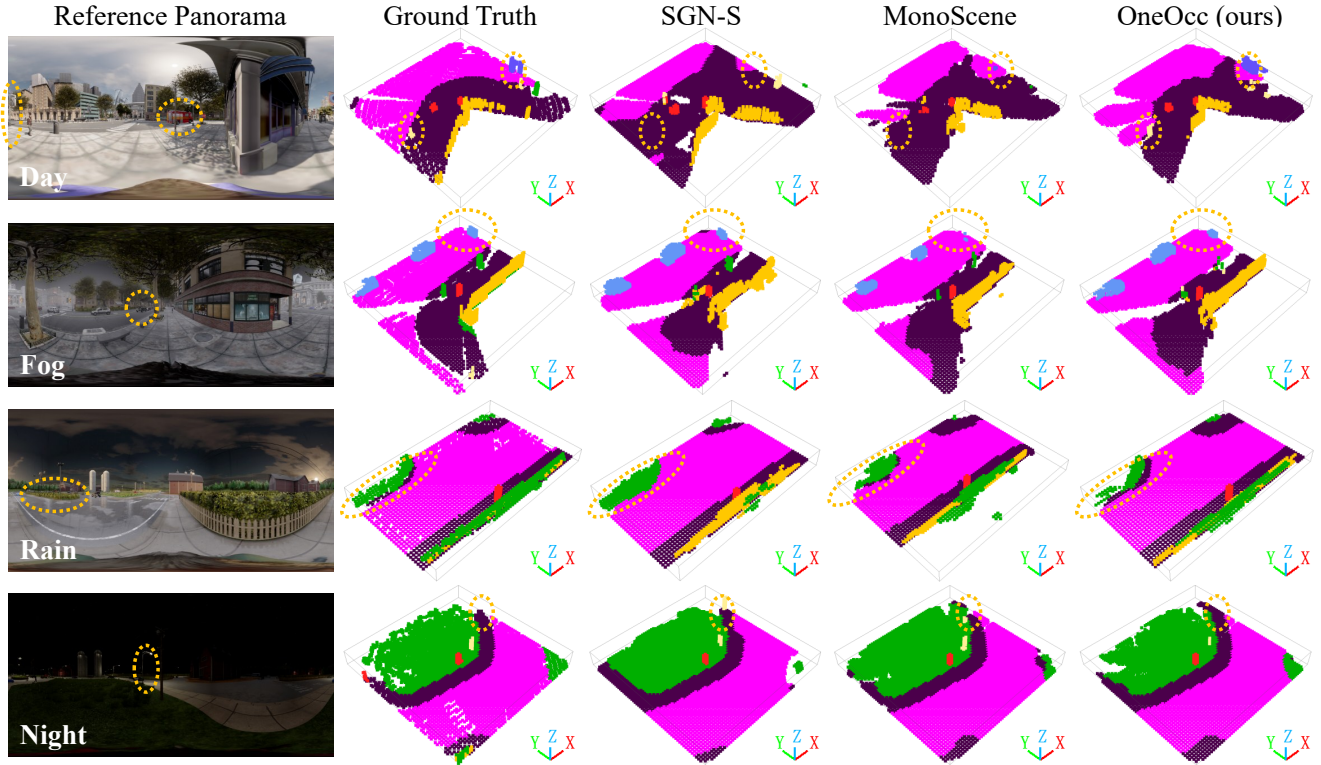


Figure 19. **Qualitative comparison on H3O-Heter under diverse weather and illumination.** From left to right: reference panorama, ground-truth occupancy, SGN-S [96], MonoScene [50], and OneOcc (ours). From top to bottom: clear day, fog, rain, and night. The heter split introduces strong cross-map distribution shift and long-tailed conditions; the performance of all methods degrades under fog/rain and becomes the most brittle at night. Notably, the circled distant lamp post is outside the OCC sensing range in the ground truth (the Night row). SGN-S and MonoScene overestimate their depth and mistakenly project it into the occupancy volume, whereas OneOcc avoids this long-range depth hallucination and yields fewer false positives, while still recovering thin structures (*e.g.*, poles) within range.

capabilities, adherence to local privacy regulations, careful consideration of where such robots are allowed to operate, and continued auditing of failure cases, especially near vulnerable populations.

12.6. Future Work

Beyond the immediate extensions discussed above, we see three main research directions.

Temporal occupancy, flow, and world models. First, moving from static occupancy to temporal occupancy sequences is a key step toward *world models* [114–116] for legged and humanoid robots. Instead of predicting only the current occupancy, one can learn to forecast future volumes conditioned on past panoramas and robot actions, or to infer an *occupancy flow* [117, 118] that encodes voxel-wise 3D motion over time. Such a flow field would provide a sparse, geometry-aware analogue of scene flow, tailored to dynamic obstacles and multi-contact locomotion. Training such models will likely require a mix of supervised signals (from synthetic data or reconstructed trajectories) and self-

supervised objectives that enforce temporal consistency and physical plausibility.

Adaptive resolution and manipulation-centric perception. Second, we plan to investigate adaptive-resolution schemes that bridge the gap between navigation-centric occupancy and manipulation-centric understanding. This includes foveated occupancy around hands and feet, dynamic refinement of regions with high uncertainty or contact likelihood, and hybrid explicit–implicit models where a coarse grid is locally refined into meshes or signed distance fields for grasp synthesis and force reasoning. A tight coupling between such perception modules and whole-body control could enable humanoid robots to seamlessly transition from long-range navigation to precise object interaction.

Data, generalization, and policy integration. Finally, scaling to broader real-world deployment will require richer data and tighter integration with decision-making. On the data side, we advocate for collecting real 360° occupancy datasets on humanoid and other platforms, with diverse

environment types and behaviors, and for exploring self-supervised pretraining on unlabeled panoramic video. On the policy side, occupancy grids can act as an intermediate tokenization layer for vision-language-action models and reinforcement learning policies, allowing language instructions and low-level control to be grounded in a common geometric space. Jointly training such policies and occupancy predictors, while preserving modularity and interpretability, is an exciting avenue toward more capable and trustworthy embodied agents.

13. More Visualizations

Figures 17 and 19 provide additional qualitative comparisons between OneOcc and representative vision-based SSC baselines under diverse illumination and weather conditions. On QuadOcc, we report results for daytime, dusk, and nighttime scenes. Across all methods, the prediction quality degrades noticeably as the illumination decreases: daytime scenes yield the cleanest geometry and semantics, dusk introduces stronger ambiguity around boundaries and small objects, and nighttime remains consistently the most challenging setting due to low signal-to-noise ratio, headlight glare, and reduced texture cues. In particular, existing perspective-based lifting methods [50] often suffer from pronounced projection artifacts and over-smoothed structures at dusk and night, leading to inconsistent free/occupied patterns and spurious semantic regions (*e.g.*, hallucinated road/sidewalk blobs). OneOcc exhibits improved robustness along this axis: by leveraging panoramic View2View fusion and bi-grid voxelization, it mitigates the typical perspective-sampling artifacts observed in FLOSP-style pipelines, and preserves more coherent occupied structures and semantic layouts at dusk and night. Notably, dynamic categories such as cars and pedestrians are more reliably localized, and their occupied footprints are less fragmented compared to MonoScene [50] and LiDAR-based LMSCNet [38].

On H3O-Heter, we further evaluate generalization under cross-map scenes and adverse weather, including clear daytime, fog, rain, and nighttime. Similar to QuadOcc, all methods deteriorate as the environment becomes more visually ambiguous. Fog reduces contrast and texture, causing baselines to miss thin vertical structures and to blur object boundaries; rain introduces specular reflections and appearance shifts that amplify road-centric priors; nighttime again triggers the largest failures. While baselines frequently collapse thin objects into the background or misclassify them into dominant terrain classes, OneOcc retains sharper geometric contours and more faithful semantics across conditions. We additionally observe a characteristic depth over-estimation error of prior methods in the heter split. As highlighted in Fig. 19, a distant lamp post (pole) lies beyond the predefined OCC sensing range in the ground truth. How-

ever, SGN-S [96] and MonoScene [50] incorrectly estimate its depth and “pull” the pole into the occupancy volume, generating spurious occupied voxels. In contrast, OneOcc does not introduce such false positives, suggesting that the panoramic View2View fusion and bi-grid lifting lead to more calibrated long-range depth reasoning under cross-map distribution shift.

Overall, these results corroborate our quantitative findings: OneOcc maintains stronger structural consistency and semantic fidelity under both illumination and weather shifts, though extreme low-light conditions remain an open challenge for monocular panoramic SSC.